Laser-Ultrasonic Measurement of Single-Crystal Elastic
Constants from Polycrystalline Samples by Measuring
and Modeling Surface Acoustic Wave Velocities

DISSERTATION

Presented in Partial Fulfillment of the Requirements for the Degree Doctor of Philosophy
in the Graduate School of The Ohio State University

By

Xinpeng Du

Graduate Program in Materials Science and Engineering

The Ohio State University

2018

Dissertation Committee:

Ji-Cheng Zhao, Advisor

Wolfgang Windl

Stephen Niezgoda

Abstract

Elastic constants C_{ij} are one of the essential properties to understand mechanical behaviors of materials. They are indispensable inputs for physics-based models of microstructural evolution and constitutive/micro-mechanistic simulations of properties. Young's modulus, bulk modulus, shear modulus and Poisson's ratio are just different combinations of elastic constant components and they only describe mechanical behavior under specific conditions. Elastic constants C_{ij} are the intrinsic parameters fully describing the elastic mechanical behavior under any given condition. Several experimental methods have been developed to measure elastic constants of materials but most of them require single-crystal samples, which are time-consuming to grow. Many compounds are not even possible to grow single crystals. As a result, only about 1% (roughly 1500 out of 160,000 kinds) of distinct solid compounds have experimental values of the elastic constants. To change this scenario, an innovative experimental method has been developed to measure single-crystal elastic constants directly from polycrystalline samples, without the need of growing single crystals.

The new method is based on measuring and modeling femtosecond laser-generated surface acoustic waves (SAWs) that only propagate on the sample surface and decay with the distance from the surface into the sample exponentially.

An elastodynamic model has been developed to predict the SAW phase velocities along any general direction at given full elastic constants and density. A femtosecond laser-based experimental set-up was applied to generate and detect SAW velocities along any specific direction. To enable measuring narrow-band SAW velocities along a single direction without any interference from multiple modes, an organic PDMS (polydimethylsiloxane) film of 1-D grating was placed on top of the sample surface to guarantee only one SAW mode survives to be detected. With modeling predictions and experimental measurements, either a forward simulation algorithm or a neural network machine learning method has been applied to extract the full elastic constants.

Polycrystalline samples of Ni, Al, Ta, Nb, Fe (bcc), Co (hcp) and β-Sn (tetragonal) have been used to benchmark the measurement accuracy. The extracted elastic constants from our method are within 6.8% of the corresponding values obtained from single-crystal samples for all seven pure metals. This new method completely frees us from growing single crystals. The high spatial resolution feature (~20 microns) in tests makes it highly applicable in obtaining high throughput composition-dependent elastic constants through localized measurements on a diffusion couple.

The power and versatility of this new method are illustrated with five measurement examples: (1) composition-dependent elastic constants from an Fe-Ni diffusion couple; (2) full elastic constants of Sn from its powders; (3) key elastic constants of the intermetallic compound Ni_3Sn_4 of the monoclinic crystalline symmetry; (4) full elastic constants of a

polycrystalline Ni-based superalloy René 88DT; and (5) Young's moduli of inorganic glass materials.

Several appendixes are provided and attached at the end of this dissertation, including bulk acoustic wave modeling, surface acoustic wave modeling, the transformation of coordinate systems among the sample coordinate system, the crystalline coordinate system and the PDMS based coordinate system, and MATLAB coding used in this dissertation.

Acknowledgments

I would like to express my sincere gratitude to my advisor Professor Ji-Cheng Zhao for providing me with this great opportunity of doing research on laser ultrasonics in his group at The Ohio State University (OSU). With his acute sense of practical applications and cutting-edge research directions, I started my research project full of perspectives, challenges and interests. Under his guidance, I learned how to focus, identified topics to explore, and took responsibilities for research. I also want to thank him for his guidance on how to interact with people and how to ask for help.

I also want to thank Professor David Cahill, Professor Alex Maznev and Professor Arthur Every for their help in my understanding the time-domain thermos-reflectance (TDTR) and SAW principles. Thanks for Dr. Dongyao Li and Dr. Qiye Zheng for useful discussions on experimental details in elastic constants and thermal conductivity measurements.

I also would like to acknowledge every member in Prof. Zhao's group (Peng Zhao, Siwei Cao, Beau Bullet, Jack Kuper, Changdong Wei, Qiaofu Zhang, Yi Li, Zhangqi Chen, Wei Zhong, Christopher Eastman, Jr. and Noah Kohlhorst) for their kind help, sharing and

experience in metallic glasses; and the help from Professor Sheng Zhang for solving the laser lasing issue.

Finally, I want to express my great gratitude to my family members, especially to my father Zhengxue Du and mother Xiaobei Chen. Their strong support allowed me to constantly focus on research. Thanks a lot also for Mengjia Yang for her support, company and encouragement.

Vita

2007-2011 ....B.S. Optical Engineering, Zhejiang

University, Hangzhou, Zhejiang, China

2011 to present ....Graduate Research Associate, Department of

Materials Science and Engineering, The Ohio

State University

Publications

Xinpeng Du and Ji-Cheng Zhao. First measurement of the full elastic constants of superalloy René 88DT. Scripta Materialia 152, 24 (2018)

Xinpeng Du and Ji-Cheng Zhao. Facile measurement of single-crystal elastic constants from polycrystalline samples. npj Computational Materials 3, 17 (2017)

Vinay S. Chauhan, M. Faisal Riyad, Xinpeng Du, Changdong Wei, Beata Tyburska-püschel, Ji-Cheng Zhao, Marat Khafizov. Thermal conductivity degradation and microstructural damage characterization by low dose irradiation using laser based techniques. Metallurgical and Materials Transactions E 4, 61 (2017)

Jie Kuang, Xinpeng Du, Xiaohui Li, Yangyang Yang, Alan A. Luo, Guoyi Tang. Athermal influence of pulsed electric current on the twinning behavior of Mg–3Al–1Zn alloy during rolling. Scripta Materialia 114, 151 (2016)

Brian T. Lejeune, Xinpeng Du, Radhika Barua, Ji-Cheng Zhao, Laura H. Lewis. Anisotropic thermal conductivity of magnetocaloric $AlFe_2B_2$. (Submitted to Scripta Materialia on April 6, 2018)

(Incoming publications)

Paul Garman, Jared Johnson, Vishank Talesara, Hao Yang, Xinpeng Du, Dan Zhang, Ying-Chieh Yen, Jianfeng Yu, Jose Castro, Wu Lu, J. C. Zhao, Jinwoo Hwang, L. James Lee. Silicon oxycarbide-catalyzed fast growth of 3D graphene networks for electronic and thermal applications

Xinpeng Du and Ji-Cheng Zhao. Facile measurement of composition-dependent elastic constants from a polycrystalline diffusion couple

Xinpeng Du, Li-Jen Yu, Yaxian Wang, C. Robert Kao, Stephen Niezgoda, Wolfgang Windl, Ji-Cheng Zhao. Determination of elastic constants of monoclinic Ni_3Sn_4 by integrating surface acoustic wave measurements with first-principles calculations

Xinpeng Du and Ji-Cheng Zhao. Laser-ultrasonic measurements of Young's modulus of inorganic Glasses

Jie Kuang, Xinpeng Du, Ji-Cheng Zhao, Guoyi Tang. Influence of pre-rolling reduction on the microstructure and texture evolution of Mg-1Ce alloy during electropulse treatment

Fields of Study

Major Field: Materials Science and Engineering

Table of Contents

xiv

List of Tables

xvi

xvii

List of Figures

Chapter 1: Introduction

1.1 Significance of elastic constants

Elastic constants, describing a material's resistance to elastic deformation when a force is applied to it, is one of the very fundamental material properties. They are essential data not only for constitutive and micro-mechanistic modeling of various properties (especially mechanical properties including plastic deformation and fracture)[1,2] but also for simulations of microstructure evolution during phase transformations and materials processing[3,4]. Moreover, since single crystals are directly used in many applications from microelectronic devices to jet engine turbine blades, anisotropic elastic constants are essential for the design of those devices and components.

Even though significant progress has been made in computing the elastic constants using density functional theory (DFT)[5–10] and molecular dynamics (MD)[11–14], accurate experimental measurements are still essential until the computed results are fully validated for accuracy.

In addition, elastic constants are highly related to thermal mechanical and dynamic properties of materials, such as thermal expansion coefficient[15,16], Debye temperature[17–19], lattice thermal conductivity[20] and specific heat capacity (or Grüneisen parameter)[21]. As a result, several thermal mechanical and dynamic properties or at least relevant components are correlated to elastic constants. In addition, a change of elastic constants of materials often implies a change of microstructure, which can help detect grain orientations, phase transitions or transformations, such as superconducting phase transition[22]. Therefore, elastic constants are very essential to understand and characterize materials in terms of both mechanisms and applications.

1.2 Fundamentals of elastic constants

Elastic constants C_{ijkl} intrinsically constitute a fourth rank tensor conjoining stress and strain in elastic deformation region through Hooke's law. It has 81 components in total but they are not completely independent from one another. Provided there is no body torque in the material, the stress under small deformations must be symmetric. This poses a constriction on the elastic constant components.

Stress symmetric:

$$\left.\begin{array}{c} \sigma_{ij} = C_{ijkl}\epsilon_{kl} \\ \sigma_{ji} = C_{jikl}\epsilon_{kl} \\ \sigma_{ij} = \sigma_{ji} \end{array}\right\} C_{ijkl} = C_{jikl} \qquad (1.1)$$

2

On the other hand, the strain by definition is also symmetric, this poses a second constriction on the elastic constants.

Strain symmetric:

$$\sigma_{ij} = C_{ijkl}\epsilon_{kl} \tag{1.1}$$
$$\sigma_{ij} = C_{ijlk}\epsilon_{lk} \Rightarrow C_{ijkl} = C_{ijlk}$$
$$\epsilon_{kl} = \epsilon_{lk}$$

Due to these two symmetry relationships, the 81 components in tensor notation reduce to 36, which can be expressed in a two-dimensional 6×6 matrix notation for sake of simplicity, called Voigt notation. But as the reduced form is not a physical tensor, any tensor transformation rule could not be applied directly on it. The original tensor expression is still necessary when transformation matrix is applied to change the base of coordinate systems.

Moreover, elastic constants are physically the second-order coefficient in the Taylor expansion series of the strain energy with respect to strain, it must satisfy Equation 1.3

$$\Psi = \Psi(0) + \frac{\partial \Psi}{\partial \epsilon_I}\epsilon_I + \frac{1}{2}\frac{\partial^2 \Psi}{\partial \epsilon_I \partial \epsilon_J}\epsilon_I \epsilon_J + O(\epsilon^2) \tag{1.2}$$

where Ψ is strain energy, ϵ is strain and $O(\epsilon^2)$ express the terms higher than the second order of the strain. The elastic constants are thus expressed as the second derivative of energy

$$\frac{1}{2}\frac{\partial^2 \Psi}{\partial \epsilon_I \partial \epsilon_J} = c_{IJ} \tag{1.4}$$

As the order of differentiation doesn't matter, Equation 1.4 also applies if we change the order of differentiation of ϵ_I and then ϵ_J to first ϵ_J and then ϵ_I. Thus, we can have $C_{IJ} = C_{JI} \Rightarrow C_{ijkl} = C_{klij}$, further reducing the number of independent elastic components to 21. For more details, readers are referred to the classical book by Nye[23].

The 21 independent components correspond to the most general case, such as a material in the triclinic crystal class. For the other six crystal classes, the number of independent components is further reduced due to the crystal symmetry defining them. Note that even within the same crystal class, the number of independent elastic components can be different. For example, tin (Sn) with a point group of 4/mmm has six independent components of elastic constants while Ashburtonite with a point group of 4/m has seven independent components of elastic constants. Generally, the number of independent components in each crystal class is: cubic (3), hexagonal (5), tetragonal (6 or 7), trigonal (6 or 7), orthorhombic (9), monoclinic (13), triclinic (21).

In addition, the form of the elastic constants is also dependent on the orientation of the symmetries. For instance, in monoclinic crystal class, the 2-fold axis parallel to the y axis or z axis will generate a different form of the elastic constants.

The physical restrictions and symmetries of materials discussed above determine the number of elastic constants. There are also numerical value restrictions on elastic constants that arise from the stability of the strain energy. For a crystal to stably exist, the strain

energy, which can be considered as the eigenvalue of the elastic constants matrix, must all be positive values. This is equivalent to saying the strain energy quadratic form $\frac{1}{2}C_{IJ}\epsilon_I\epsilon_J$ has to be positive and definite. One of the necessary and sufficient conditions for this is that the determinants of the 6×6 elastic constants from the first order to the full order are all positive, as numerically expressed in Equation 1.5. More details can be found in Ferrar's book[24].

$$C_{11} > 0, \begin{vmatrix} C_{11} & C_{12} \\ C_{21} & C_{22} \end{vmatrix} > 0, \ldots\ldots, \begin{vmatrix} C_{11} & \ldots & C_{16} \\ \ldots & \ldots & \ldots \\ C_{61} & \ldots & C_{66} \end{vmatrix} > 0 \qquad (1.5)$$

Generally, Equation 1.1 to Equation 1.5 describe all the conditions the elastic constants must satisfy.

1.3 Experimental methods of measuring elastic constants

Since full elastic constants are hard to measure, simplified moduli have been developed for practical use such as Young's modulus, defined to be the ratio of the longitudinal stress to the longitudinal strain; P-wave modulus, defined to be the ratio of the longitudinal stress to the longitudinal strain without any lateral strain; bulk modulus, defined to be the absolute ratio of the dilation to the hydrostatic pressure; shear modulus, defined to be the ratio of shear stress to shear strain; Poisson's ratio, defined to be the ratio of lateral strain to the longitudinal strain due to a uniaxial tension applied to the longitudinal direction. These moduli describe elastic mechanical behavior response under different external stress-strain

conditions. Standards of sample preparations and experimental protocols to measure those moduli have also been established and extensively used in industry and academia[25–27].

Those methods are very straightforward to apply; but the disadvantages are also obvious: (1) it needs a sample of quite a large size (at least mm) to measure; (2) it needs a standardized shape of samples, such as a dog-bone shape for Young's modulus; (3) it only measures an average effective modulus of the sample; and (4) it only measures several practical moduli rather than the intrinsic fourth rank tensor elastic constants.

In order to measure the full elastic constants, several experimental techniques have been developed. Most of current methods, however, more or less depend on single crystals to extract the full elastic constants, such as the RUS (Resonant Acoustic Spectroscopy) method, ASM (Acoustic Spectro-Microscopy), BS (Brillouin Scattering), SAM (Scanning Acoustic Microscopy), and PS/PR (Point-Source/Point-Receiver) measuring either bulk acoustic waves or surface acoustic waves. Their features and limitations are generally described below.

The RUS method generates acoustic waves into the sample through a contact transducer and measures resonant frequencies. It extracts the elastic constants by matching the simulated resonant frequency response patterns at given sample geometry, density and elastic constants with the experimental ones[28,29] . Since the resonant modes depend not only on the material itself but also on the geometry of the sample, regular shapes of samples

6

are often used, which poses a requirement on the sample preparation. Moreover, it measures the whole sample and thus no spatial resolution could be considered.

The ASM method also inputs acoustic pulses into the sample but it measures the acoustic velocity directly[30,31] rather than the resonant frequency. This configuration is appropriate for localized measurements and doesn't need to require a specific sample geometry except a polished surface. However, it needs a couplant liquid such as water to measure the velocity, which limits the types of samples and conditions of experiments. In addition, it requires a high accuracy of eucentricity during the rotational measurement and high position accuracy when switching between the optical unit and the ASM unit. This increases complexity and uncertainty.

The BS method essentially makes use of the inelastic scattering often induced by laser and measures the width of the shift frequency (the doublet) to determine propagation velocities to obtain the elastic constants[32,33]. The BS method also frees us from the constraint of sample geometry and macroscopic size, and also it has high special resolution. A good example of application of BS on cubic materials can be found in the paper by Benedek et al.[32]. However, as it needs an accurate alignment of incident light direction, the determination of orientation of the sample becomes extremely important. Moreover, it requires a bulk sample of high quality because and scattering from particles or defects along the way in transmitting across the bulk will lead to deterioration of the measurement

results. More details about the principle and analysis of BS in determining elastic constants can be found in the book of Hayes and Loudon [34].

The PS/PR method uses a point source and a point receiver to generate and detect acoustic waves and extract elastic constants through measuring acoustic velocities. Since the advent of laser, PS/PR methods have been improved to a large extent. A laser is employed to generate either surface or bulk acoustic waves, depending on experimental configurations. A systematic method conjoining phase velocity of bulk waves and elastic constants has been developed by Every[35]. Due to the anisotropy of materials, however, the experimentally measured acoustic velocities are actually group velocities rather than phase velocities. Early on, researched simply neglected the difference and substituted group velocities into the model built for phase velocities, which could lead to generate significant error[36]. In order to overcome the dispersion issue derived from material anisotropy, Every and Sachse established the technique to extract elastic constants directly through measuring group velocities of bulk waves[37]. A systematic explanation of the bulk wave features can be found in the book of Rosenbaum[38].

As bulk wave modeling is more straightforward and convenient, extraction of elastic constants from bulk acoustic waves has made great progress. However, as bulk microstructure can affect bulk acoustic wave propagation, especially if the wave passes through multiple phases or multiple grain orientations; experimental configurations for

bulk acoustic waves often need to access two sides of a sample with thickness between them known, which limits the applicability of this method to plate type samples.

To minimize the interference from bulk microstructure and deal with the possible lack of good availability of front and back sides of a sample, the relation between SAW velocities and elastic constants attracted more attention. Because surface waves only penetrate a very limited length, estimated to be the wavelength divided by 2π[39], it can significantly reduce constraints on the sample geometry. Farnell has made a concise description of the characteristics of SAWs[40].

Interdigital transducer (IDT) is widely used to generate and detect SAW velocities. Typically, it consists of an array of piezoelectric electrodes to launch SAWs and use another array of electrodes to receive them. More details in theoretical modeling and solution to SAWs generated by IDT can be found in the paper by Milsom et al.[41]. An example of applying this method in measuring elastic constants of AlN can be found in the paper by Bu et al.[42]. But this method is complicated in modeling as both mechanical and electrical boundary conditions need to be considered. Moreover, it needs relatively large single crystals, at least large enough to accommodate separate electrodes, for measurement. It also needs a transducer layer between electrodes and piezoelectric sample, which significantly reduces the applicability of this method in determining elastic constants.

SAWs generated by PS/PR method are mostly broadband waves. Two phenomena should be considered in measuring the SAW velocities. One is phonon focusing[43,44], which leads to stronger amplitudes of acoustic waves in certain directions even though the source generates uniform distribution of wave vectors. The other is cuspidal structure[45], which leads to the formation of some cusps in certain directions. These two phenomena bring confusions in wave characterization, such as multiple arrivals of SAW waves along a direction[46], thus affects the velocity measurement for the broadband waves. The dispersion between phase and group velocities in broadband waves as in bulk wave cases still significantly interfere velocity measurements.

In order to measure the full elastic constants accurately, generation and detection of narrow-band SAWs is more preferable. Usually, a periodic grating pattern needs to be put on the sample surface to obtain narrow-band SAWs by suppressing other wave modes and only allowing one mode of SAW wave to propagate along the grating vector with the wavelength equal to the period of the grating. So far, SLM (Spatial Light Modulator)[47–50], GMD (Grating Metal Deposit)[51–54] , ISTS (Impulsive Stimulated Thermal Scattering)[55–58] and OFG (Organic Film Grating) are often used to produce the grating pattern. These methods have successfully generated reliable single-mode SAW. The OFG method is adopted in this study.

On the modeling side, a robust mathematical solution has been first developed to compute the SAW velocity along any crystallographic orientation of any crystal structure type with

given elastic constants and density[59]. Such a solution with inclusion of the thermal expansion effect induced by localized heating of a Gaussian-shaped laser beam is essential to accurately correlate the SAW velocities to the elastic constant values. The solution includes full computation of all the bulk waves including the longitudinal (L) mode, the fast-transverse (FT) mode, and the slow transverse (ST) mode as well as SAWs including both the Rayleigh wave (RW) and the pseudo surface acoustic wave (PSAW).

On the experimental side, a Ti:sapphire femtosecond laser was employed to generate and detect narrow-band SAW waves assisted by a 1-D grating PDMS film. This leads to high spatial resolution to enable measurement on individual grains on a polished surface of a polycrystalline sample. The experimental SAW velocities were fitted through either a forward simulation method or neural network machine learning method, aimed at obtaining a set of optimum elastic constants that reproduce calculated SAW velocities with minimum difference with experimental ones. The optimum elastic constants are taken as the elastic constants of the material. More details will be given in following chapters.

Chapter 2: Theoretical Modeling

(This chapter is mostly based on the paper: Xinpeng Du and Ji-Cheng Zhao. Facile measurement of single-crystal elastic constants from polycrystalline samples. npj Computational Materials 3, 17 (2017).)

2.1 Model establishment

In order to predict surface acoustic wave velocities along any arbitrary crystallographic orientation at given crystal structure, orientation, elastic constants and density, a model based on the elastodynamic equation has been developed[59]. On the assumption of linear elastic deformation in a homogeneous anisotropic medium and the absence of body force, body torque, dissipative process or external fields, the governing equation is expressed as follows:

$$C_{ijkl} \frac{\partial^2 U_l}{\partial x_j\, \partial x_k} = \rho \frac{\partial^2 U_i}{\partial t^2} \qquad x_3 \leq 0 \qquad (2.1)$$

where U is the displacement, ρ material density and C_{ijkl} the elastic constants. The variables x and t stand for space and time, respectively. The $x_3 \leq 0$ condition refers to a

12

semi-infinite system and only the lower half space is taken into consideration. Here the Einstein summation convention is implied. If the restriction of the half space is removed out from Equation 2.1, the equation corresponds to pure bulk wave modeling and the solutions correspond to the three (and only three) bulk wave modes: the L wave (longitudinal wave), the FT wave (fast transverse wave), and the ST wave (slow transverse wave), respectively.

These bulk wave solutions from the unconstrained Equation 2.1 are obtained by assuming the displacement U has an exponential form and then substituted into Equation 2.1. This method is elegantly summarized by Rosenbaum[38]. Our bulk wave model is coded accordingly. More details on the bulk acoustic wave model are provided in Appendix B.

In order to solve for SAWs, initial and boundary conditions need to be added for the response of the surface displacement under a point stimulus exerted by an external force in a semi-infinite system. The evolution of the surface displacement provides information to predict SAW velocities along any orientation of interest at given elastic constants, orientation and density. The corresponding boundary conditions are set as:

$$\sigma_{i3}|_{z=0} = C_{i3kl}\frac{\partial U_l}{\partial x_k}|_{z=0} = \delta_{i3}\delta(x,y)\delta(t) \tag{2.2}$$

$$U_i(x,y,z,t) = 0, \quad \text{when } x,y,z,t \rightarrow \infty \tag{2.3}$$

Where,

$$\delta_{i3} = \begin{cases} 1 & i = 3 \\ 0 & i \neq 3 \end{cases} \tag{2.4}$$

13

$$\delta(x, y) = \delta(x)\delta(y) \tag{2.5}$$

$$\text{and } i, j, k, l = 1,2,3 \tag{2.6}$$

The corresponding initial condition is determined by the causality principle

$$U_i\ (x, y, z, t) = 0\ for\ t < 0 \tag{2.7}$$

Boundary condition (2.2) refers to beginning when the force only exerts on the origin and the stress only has a non-vanish component normal to the surface. Boundary condition (2.3) refers to the vanishing displacement on the surface at infinite time or space. Initial condition (2.7) refers to the zero displacement before any trigger (laser impingement).

2.2 Model solution of SAWs

Various ways to solve surface waves models are carefully reviewed by Every et al.[60] and Favretto-Cristini et al.[61] . They include Fourier-Laplace transform which is later improved and finally combined to be the Cagniard-de Hoop method[62]; and Fourier-Radon transform[63]; What is adopted here is a method of performing triple Fourier transform merely on the time variable and space variables parallel to the surface, leaving the third vertical space variable intact. Since only the wave velocities rather than the displacements are of interest, the inverse Fourier transform becomes unnecessary. The SAW velocities can be obtained in the Fourier-transformed space, saving a significant amount of computing time.

Results from this new surface acoustic wave modeling are consistent with the work of Every et al.[60] but the new model is much easier to implement in computer coding, especially for handling low-symmetry orientations that are essential for measurements on polycrystalline samples. A broader and in-depth understanding on acoustic wave modeling, can be found in an elegant review by Favretto-Cristini et al.[61]. More details on how to solve the surface acoustic wave model can be found in Appendix A.

The capability of the models and algorithms in predicting all the bulk and SAW modes is demonstrated in Figure 1, which shows modeling results for pure Ni on its (001) plane and is plotted in the slowness space – the slowness is the reciprocal of the phase velocity by definition and it is widely used to simplify the plotting. A separate fast-acting model is used to compute the bulk waves (Figure 1(b)) so they can be quickly identified from the general model result (Figure 1(a)). Here we use the term Surface Acoustic Wave (SAW) and the term Rayleigh Wave (RW) interchangeably. By qualitatively matching those bulk wave modes in the surface modeling results, the rest two surface modes (RW and PSAW, Pseudo Surface Acoustic Wave) can be identified quickly. A careful comparison of the bulk-wave-only behaviors without the surface waves (Figure 1(b)) with those in the presence of SAWs (Figure 1(a)) shows that the FT wave behavior was slightly altered by the SAWs but the L wave is unaffected; thus the FT wave position matching between the bulk-wave-only results and those of full calculations can only be qualitative. The PSAW is "supersonic" since its velocity exceeds the limiting bulk velocity which is defined as the slowest bulk wave velocity, i.e., the velocity of the ST wave along the orientation of

15

interest. In contrast, RW is "subsonic" and thus it can be identified along any given propagation orientation as the peak with a velocity lower (higher slowness) than that of the ST wave (Only in extremely rare cases the RW velocity is "supersonic" and such situations can be identified by the full surface and bulk wave calculations)[60,61]. For orientations along which the RW is too weak to be observable, the PSAW is selected as the SAW. This is accomplished by a first search of the RW peak in the slowness region above that of the ST wave; and in the absence of an observable RW peak, the program/algorithm selects the first peak with the slowness lower than that of the ST wave. The SAW velocity is simply the reciprocal of the slowness of the identified SAW/PSAW peak.
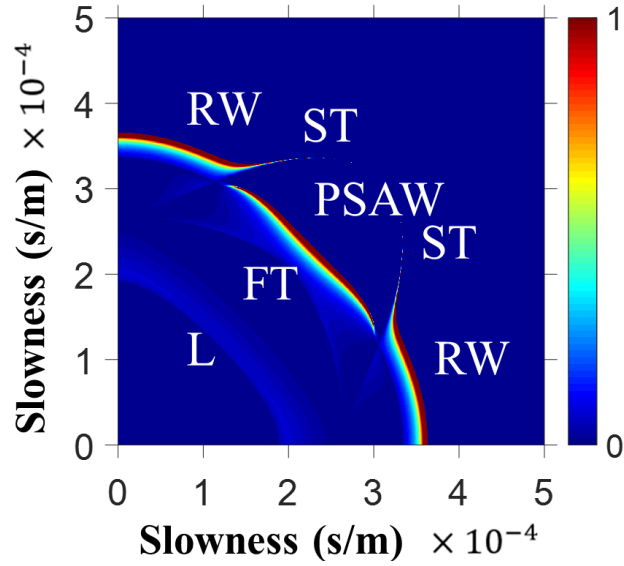
(a)
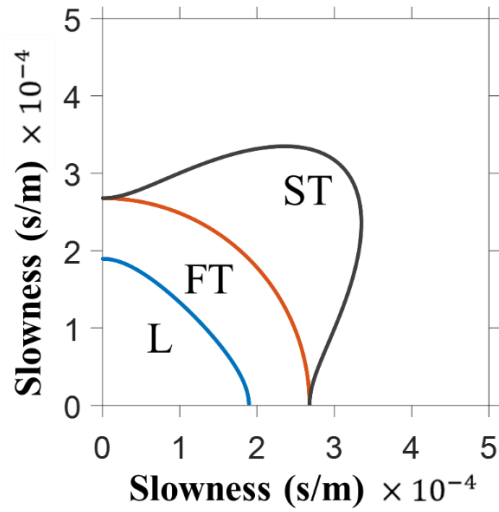
(b)

Figure 1. Computed acoustic wave behavior on the (001) surface of pure Ni plotted in the slowness (reciprocal of velocity) space: (a) full solution with both surface waves and bulk waves; and (b) bulk wave solutions only. The fast-acting bulk wave solutions in (b) for the L, FT, and ST modes help the identification of the two surface waves: the RW and the PSAW. The color in (a) shows the relative magnitude of the wave displacement on the surface.

17

The presence of multiple bulk and surface waves along a low symmetry orientation is shown in Figure 2(b) as an example, in contrast to a high-symmetry [010] orientation in Figure 2(a) (the same orientation as the vertical axis of Figure 1(a)), both for pure Ni. The slowness (reciprocal of velocity) of the ST wave is also computed for each orientation from the bulk wave model and is denoted as the dashed lines in Figure 2. Even though the ST peak happens to be too weak to be observable in both orientations in Figure 2, the computation of its position from the bulk wave model is essential to help identify the RW peak. The RW peak can be identified since it has lower velocity (higher slowness) than the corresponding ST wave along the same orientation.
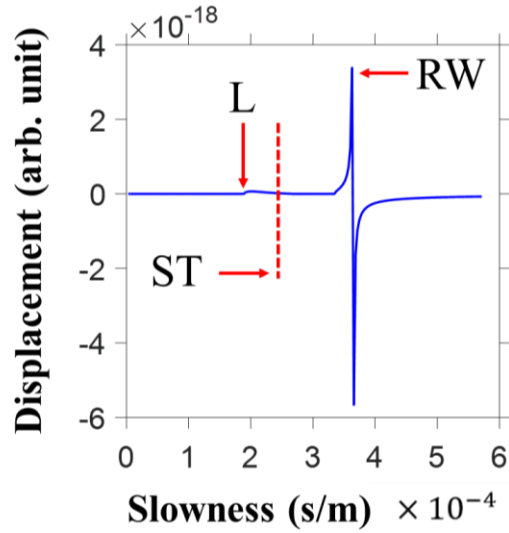
(a)
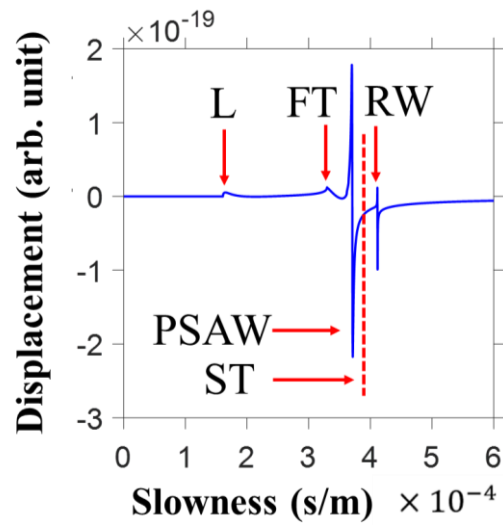
(b)

Figure 2. Computed wave displacement as a function of slowness for pure Ni along (a) a high-symmetry direction [010] and (b) a low-symmetry direction [0.69 0.59 -0.42], showing the presence of several wave modes along the low-symmetry orientation. The bulk wave modeling helps identify the bulk L and FT modes and can compute the slowness of the ST mode even though its displacement is too low to be observable along these two orientations. The computed ST mode information is essential for the identification of the SAW.

In order to identify the RW peak, bulk wave modeling by using the same elastic constants, orientation and density was applied as mentioned. L and FT modes are easy to match as the peaks match well in both calculations. ST mode is also obtained externally but as it's interfered by other two peaks, there is no significant peak appearing there, thus we draw a dashed line to denote where it is. Based on what we mentioned above, the wave velocity of ST is the limiting velocity, above which is PSAW peak while below which is RW peak. Thus, we could easily recognize RW and PSAW peaks, respectively. Note the relative heights of peaks are not the right way to judge which mode is which. Similarly, we take the reciprocal of RW slowness to get the surface acoustic wave velocity along that general direction. Our surface modeling result is in accordance with Every's work[60]. Readers can refer to that book to get more details.

The above description introduced modeling procedures to calculate SAW velocities alone any arbitrary orientation at given elastic constants and density. The default orientation of the grain plane in the above example is the (100) plane expressed in the sample coordinate system. The default reference direction for surface acoustic wave velocity is the sample transverse direction (TD).

As SAW velocities are measured under the sample coordinate system while calculations are performed under crystalline principle coordinate system, electron backscatter diffraction (EBSD) is employed to connect these two coordinate systems. EBSD measures grain orientations by comparing electron diffraction patterns (Kikuchi pattern) with

reference patterns and returns the Euler angles that represent three consecutive rotations, bringing the sample coordinate system into coincidence with the crystalline coordinate system. Thus, the direction of the SAW velocity can be expressed in terms of crystalline coordinate system through the Euler angles. A polycrystalline Ni sample is provided as an example here.
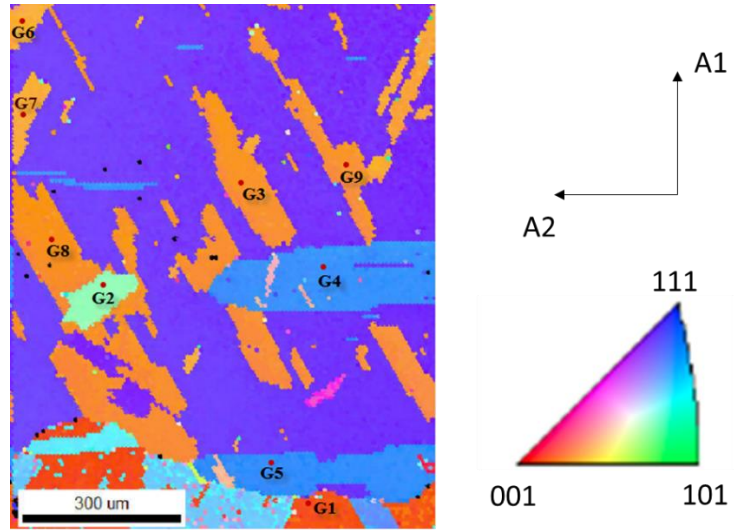
(a)
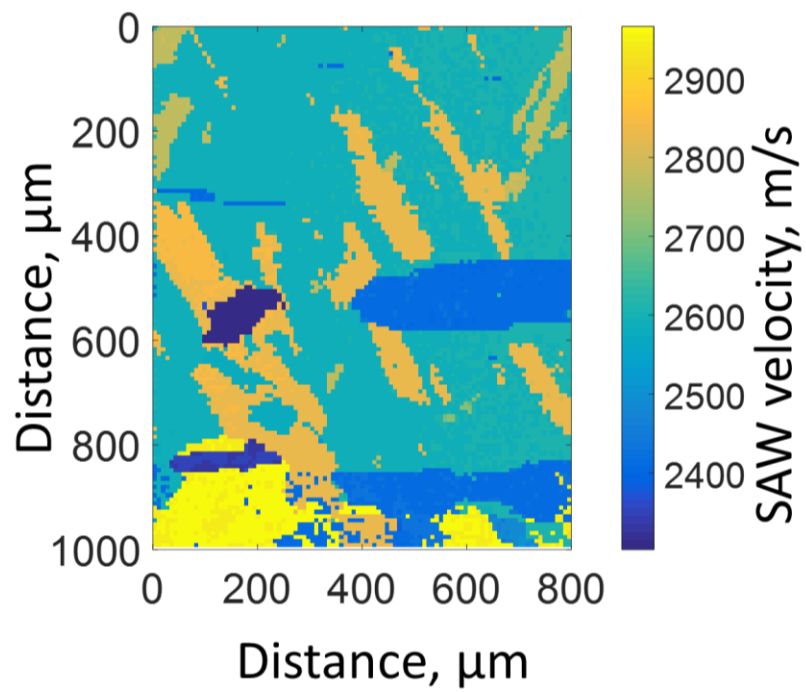
(b)

Figure 3. Schematic showing (a) EBSD orientation map and (b) SAW velocity map along the reference TD direction for a polycrystalline Ni sample. Both maps captured similar characteristics of the sample surface, confirming the validity of our model.

The EBSD inverse pole figure of a region on a polycrystalline Ni is shown in Figure 3(a). With the Euler angles, the coordinate system transformation could be applied on the governing equation and then the surface acoustic wave velocities along a certain direction could be calculated. The surface acoustic wave velocity map along the reference TD direction was shown in Figure 3(b), which captures most of the characteristics in the EBSD orientation map, showing the consistency with each other.

Chapter 3: Experimental Measurements

(This chapter is mostly based on the paper: Xinpeng Du and Ji-Cheng Zhao. Facile measurement of single-crystal elastic constants from polycrystalline samples. npj Computational Materials 3, 17 (2017).)

3.1 Experimental set-up.

Time-domain Thermoreflectance (TDTR) was employed to generate and detect SAW velocities[64], as is shown in Figure 4. The main Ti:sapphire laser, pumped by a semiconductor (Nd:YVO) laser, emitted a laser beam with a wavelength adjusted to be 780 nm. The beam passed through several optical components and was then split by a PBS (Polarizing Beam Splitter) into two branches: one was the pump beam, which was modulated at 9.3 MHz by an EOM (Electro-Optic Modulator) and used to trigger acoustic waves on the sample surface; and the other was the probe beam, used to detect acoustic waves through the change of the surface displacement profile that was confined within the parallel grating lines of the PDMS grating film. The mechanism of the TDTR signal is explained in detail by Li *et al.*[65]. A delay-stage was employed to adjust the optical path

length travelled by the pump beam relative to the probe beam; and hence the time difference/delay of the arrivals of the two beams on the surface. Therefore, the intensity of the signal could be obtained as a function of the time delay between the pump and probe beams. The probe beam with a diameter of ~5 µm was placed at the exact location of the pump beam with about the same laser beam diameter. When the pump beam was moved away from the probe beam in this pump-probe measurement, the signal diminished very quickly; indicating that the generated SAW was confined close to the pump beam diameter and thus the spatial resolution of the measurement can be on the order of 10–15 µm. In order to increase the signal-to-noise ratio, lock-in modulation technique was adapted here. A signal generator generated a square wave of frequency 9.3 MHz, which was used to modulate the EOM and set as the reference frequency for the lock-in amplifier, which was used to demodulate the signal into in-phase and out-of-phase parts for signal analysis. A CCD camera was used to observe and check the optical alignment and the laser spot shape in the entire process. Once the set-up is ready, the entire measurement process was controlled and monitored by a custom programmed main LabVIEW VI (Virtual Instrument) code with a graphic interface.
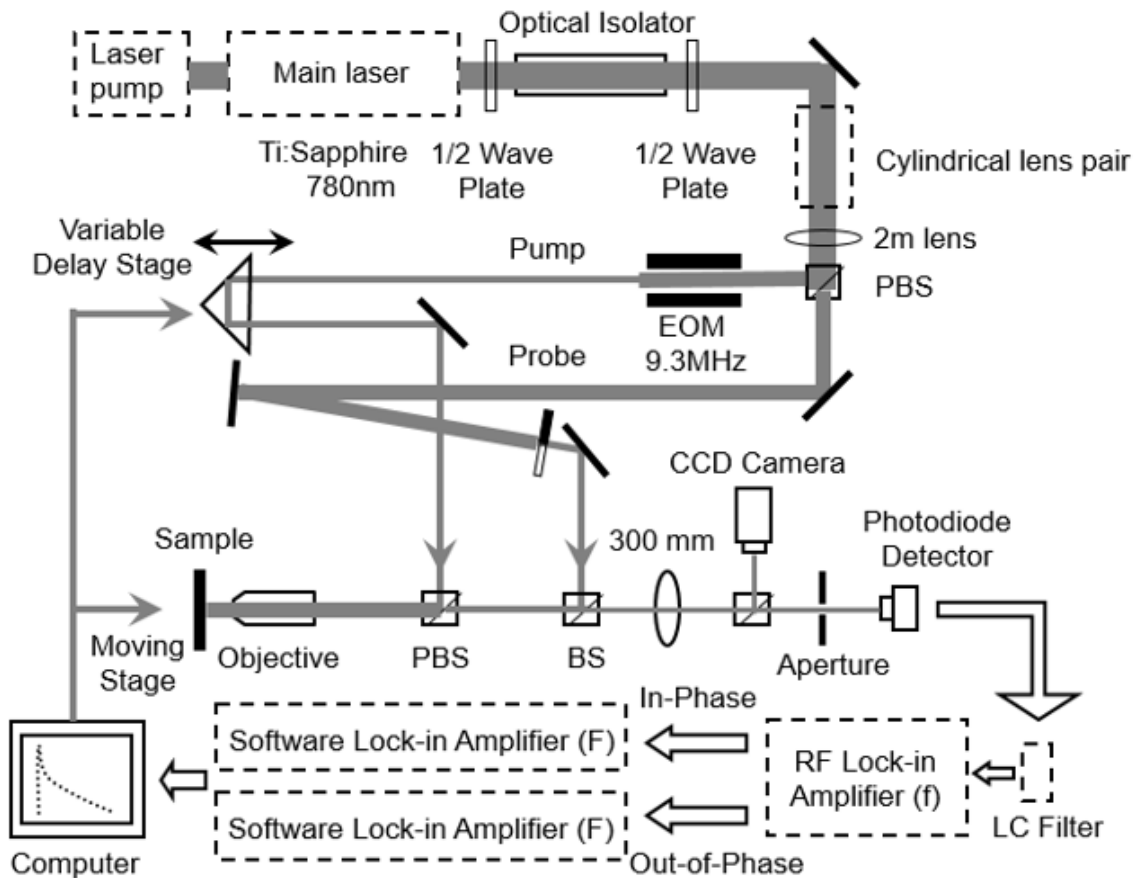
Figure 4. Schematic showing the TDTR experimental setup. Optical paths of laser beams, and the corresponding optics and instruments are all labeled.

The main LabVIEW VI consists of several sub-VIs for data acquisition and delay stage motion control. As the experimental procedures mature, more features like experimental mapping, data auto-fitting, data auto-saving and results display were incorporated into the main VI with each function achieved in a specially programmed sub-VI. A MATLAB script node was used in LabVIEW to facilitate linkage to MATLAB programs, which brought tremendous convenience.

26
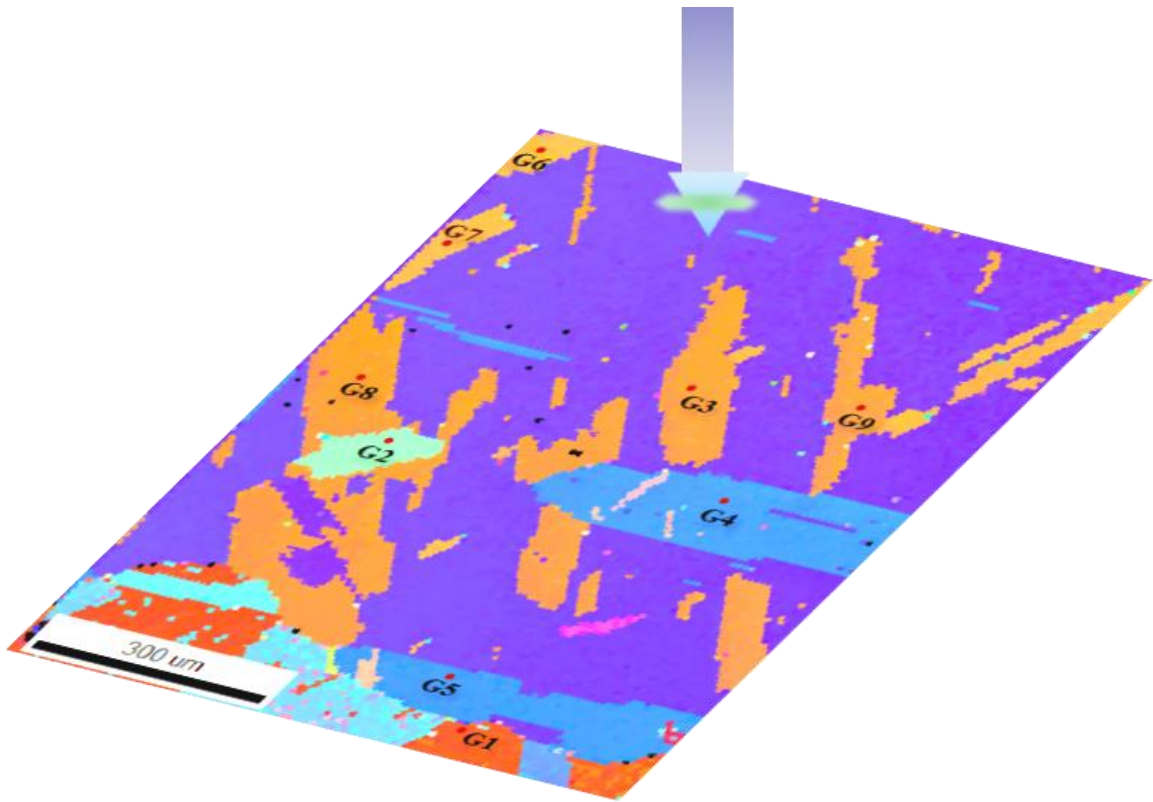
Figure 5. Schematic showing the relative configuration of laser illumination on the polycrystalline Ni sample surface.

During each TDTR experiment, the optical paths of the laser beams need to be optimized first. The laser illuminated the polycrystalline sample surface locally with a complete overlay of the pump and probe beams, as shown in Figure 5. Both the pump and probe beams are of similar spot size. They were then converged by a 20X object lens to form a coincident spot ~5 μm in radius on the sample surface.

A biased Si photodiode detector was used to detect the signal intensity. This diode has a wide response wavelength range from 200 nm to 1100 nm and very fast response time (about 1 ns rise time). The delay stage stopped for 300 ms at each step as it proceeded to change the time delay, which took much longer than 1 ns. Therefore, this detector is fast enough to capture signal features. A typical signal intensity profile is displayed in Figure 6. At zero time delay, both pump and probe arrived on the sample surface at the same time, the intensity reached the maximum. With the time delay increasing, the signal intensity kept decreasing due to the decreasing surface temperature as the local heat deposited by the pump beam was transmitting into the bulk and dissipating away before the probe beam could arrive to detect. This gradual decreasing curve could be fitted with an exponential function.

28
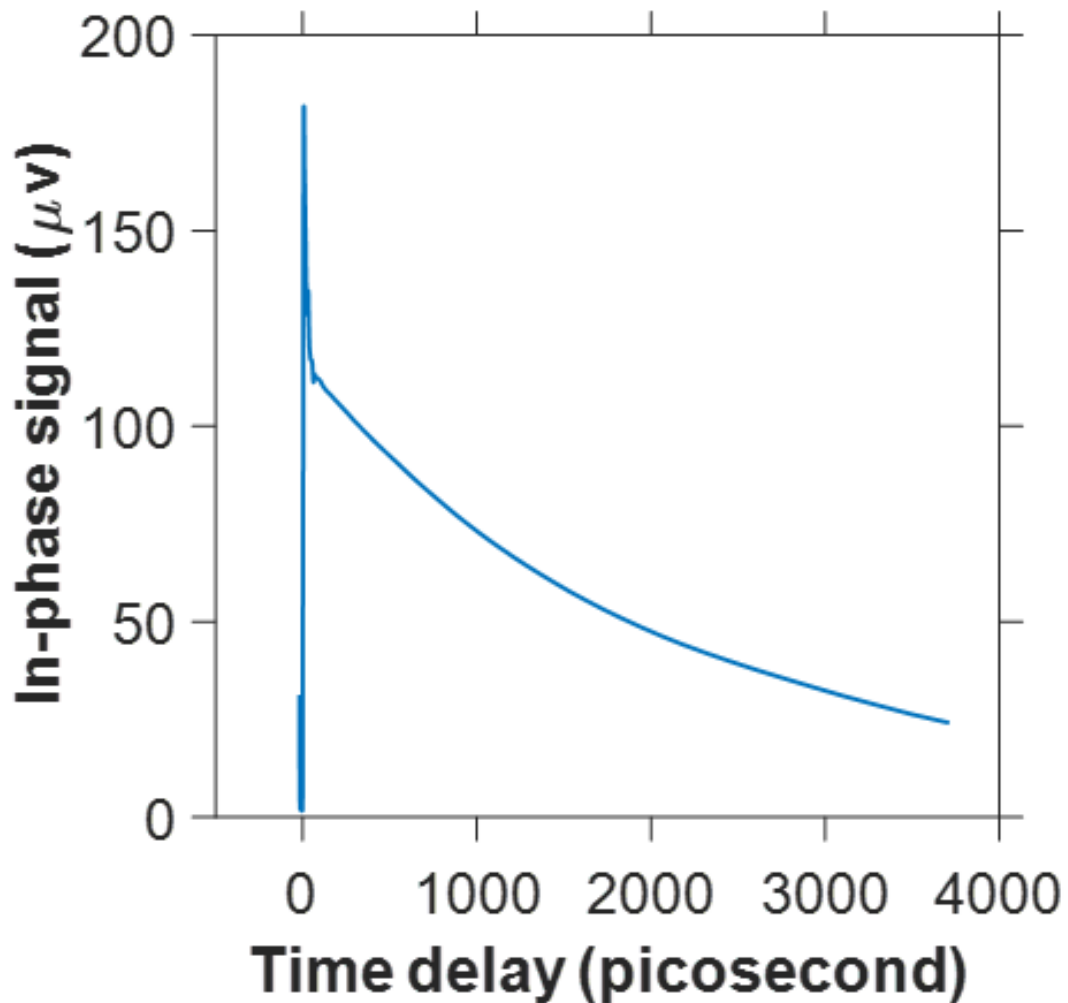
Figure 6. TDTR signal in the time domain without PDMS grating modulation showing a decreasing trend because of the heat conduction into the sample.

It is worthwhile to contemplate the time scale. The change of optical reflectivity ΔR of the material was due to the temperature change induced by the deposited heat from the pump laser, which would generate acoustic wave through the thermo-elastic effect[66]. Typically, the time scale for the acoustic wave propagation in metals is usually in picoseconds[67]. The

laser pulses have a repetition frequency of 80 MHz and pulse duration of 200 femtoseconds (fs), which are adequate in time resolution to capture the fast-changing signal. Before the appearance of femtosecond mode-locked laser, interferometric or diffraction techniques was applied to determine acoustic signals[68], which was compatible with a pulse duration much longer than femtoseconds. Thus, the TDTR laser experimental setup is very critical to ultrafast acoustic research.

3.2 Sample preparations

Seven polycrystalline pure metals were purchased and prepared. They are Al, Co, Fe, Sn, Ni, Nb, and Ta. All of them were purchased from commercial sources: Al (99.9995 wt.% purity) from Alfa Aesar; Co (99.95 wt.% purity), Fe (99.95 wt.% purity), Sn (99.95 wt.% purity) and Ni (99.95 wt.% purity) from the Micron Metals, Inc.; and Nb (99.95 wt.% purity) and Ta (99.95 wt.%) from Kamis Inc.

To help grow the grain size and to reduce potential residual stresses, each sample was subject to a heat treatment. The temperature and time were selected based on the melting point of the metals.

After the heat treatment, small pieces of each sample were sectioned from a bulk and mounted into conductive bakelites (either graphite- or cooper-based). All samples went through the usual metallographic preparation procedures including grinding with

progressively finer grit SiC grinding papers (from 120, 320, 600, 800 up to 1200 grit) and polishing with 1 μm diamond paste. A final step was the usual process for EBSD sample preparation, either a vibratory polishing with 0.05 μm colloidal silica spheres suspended in water or an electro-polishing for very soft metals such as Al.

As mentioned before, a PDMS film with periodic pattern was made and used to generate narrow-band SAWs. The PDMS films of about 1×1 cm squares were prepared from a pure Si grating mold with parallel groves of 700 nm periodicity, 50% duty cycle and 350 nm groove depth (SNS-C14.3-0808-350-D45-P, LightSmyth Technology). The PDMS solution (Sylgard 184, Dow Corning) and its curing agent with a ratio 10:1 were well-mixed and poured onto the Si wafer mold, degassed at ambient temperature in a desiccator linked to a mechanical vacuum pump for several hours, and then cured at 80 °C in a reduced vacuum oven for at least one day to achieve full curing. The PDMS film was then peeled off from the Si mold and placed onto the polished surface of the samples with the PDMS film grating lines touching the surface. The PDMS film worked like a set of comb transducers, playing the role of confining the acoustic mode propagating along the direction parallel to the film grating vector with a wavelength the same as the film periodicity. The PDMS film fabrication process is mostly following the literature practice, but modified with one formula instead of two. More details about the functionality and the fabrication of the PDMS film can be found elsewhere[65]. Optical microscopy at 1000X magnification was often used to check whether the grating structure was successfully transferred from the Si mold to the PDMS film.

The longer the curing time, the longer the film can keep the grating structure. However, curing for too long, say, half a year, resulted in impaired mechanical property of the PDMS film. The film became very vulnerable to tearing and peeling. Even though the PDMS films can be peeled off and attached to samples repeatedly, it was preferred to apply a fresh PDMS film for a different sample in case of any contamination or film damage.

3.3 Determination of SAW propagation directions

The direction of the SAW wave was determined by two orientations. One is the grain orientation and the other is the PDMS film orientation. EBSD was employed to measure the grain orientation. Several indents were placed on a polycrystalline sample surface to encompass a region in interest, then EBSD mapping was performed to get the Euler angles that connected the sample coordinate system and crystalline coordinate system.

As SAWs propagated along the direction parallel to the PDMS film grating (perpendicular to the grating lines), which was not necessary the transverse direction in the sample coordinate system, a new coordinate system was constructed to take that into account. The new coordinate system comprised the real propagation direction, the direction pointing out of paper and a third direction that made it a right-hand Cartesian coordinate system. Optical microscopy was employed to measure the deviation angle between the reference direction (often the transverse direction) and the grating vector. As this new coordinate system differed from the sample coordinate system by just an in-plane rotation, the deviation angle

32

was enough to connect these two coordinate systems through a coordinate system transform in a similar fashion as the evaluation of the Euler angles. The direction of the film grating vector (the same as the propagation direction of the measured SAW) was often brought into coincidence with the transverse direction. A microscopic image of the PDMS film and corresponding coordinate system relations can be seen in Figure 7. More details about the mathematical transforms connecting the various coordinate systems are shown in Appendix C.
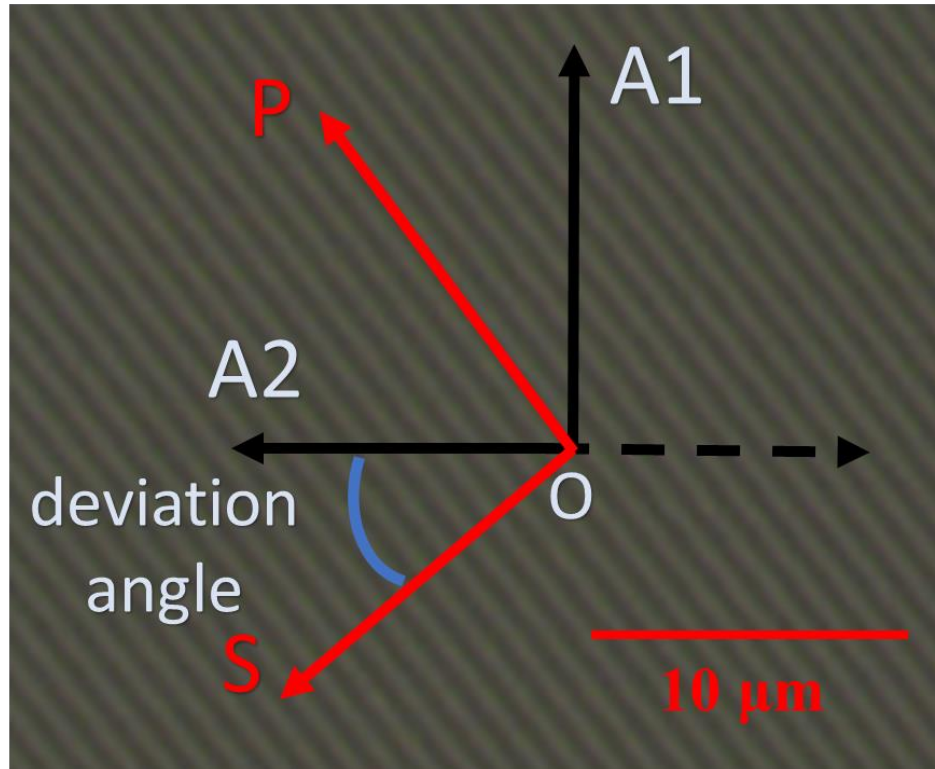
Figure 7. Optical image of the PDMS film and corresponding angle relations in different coordinate systems. A1 and A2 stand for RD and TD directions in the sample coordinate system. The ND direction points out of the paper. They formed the sample coordinate system. OP stands for the PDMS film grating line direction while OS stands for the direction of SAW propagation. OP and OS are perpendicular to each other.

3.4 Measurements of SAW velocities

As displayed in Figure 5, a small region (800 μm × 1000 μm) in the polycrystalline Ni sample was selected for EBSD orientation measurements with step size 8 μm for either direction. Nine representative locations based on the distribution and size of grains were selected for TDTR measurement. Repeated measurements were performed on each location to obtain SAW velocities to show repeatability. The indents put on the sample surface previously helped mark positions and facilitate locating successive spots for laser measurements. To avoid any grain boundary interference, large grains of size above 100 μm were preferred and the laser beam was moved to the grain center for measurement. About 400 temporal points within 3500 ps were linearly sampled as the delay stage moved in its path to complete each measurement, which took about 4.5 minutes. Usually 4 measurements were performed in a small area within 10 μm of the grain center to get the SAW velocity along a single crystalline direction. Thus, it usually took 18 minutes to obtain one SAW velocity.

A representative signal intensity profile, with grating modulation, as a function of delay time between the pump and probe beam is displayed in Figure 8(a) in the time domain and in Figure 8(b) in the frequency domain. The intensity profile was no longer a simple gradual decreasing curve as displayed in Figure 6. Rather, the signal had a periodic modulation with a gradual decreasing envelop. The gradually decreasing envelop was attributed to the heat transport inward to the sample. The periodic modulation was due to SAW as it was

confined by the PDMS grating structure. The detailed mechanism of the generation of the

TDTR signal by the interaction of SAW with the PDMS grating is explained by Li et al.[65]

As the SAW velocity is equal to the wavelength times the frequency, and the wavelength

is equal to the period of the PDMS grating film (700 nm in this case), and thus the

frequency is measured from TDTR signals. Here the Fourier transform was applied to

convert the time domain signal to frequency domain signal, as shown in Figure 8, where

the SAW peak could be obtained to calculate the SAW velocity.

The Fourier transform, or more accurately discrete Fourier transform, was conducted

through FFT (Fast Fourier Transform) algorithm built in MATLAB[69]. The data acquisition

rate was 400 data points in 3500 ps delay time, which leads to a frequency bandwidth of

roughly 114 GHz. Then the data points were extended to 2 to the power of 16 by padding

zeros to get sharper FFT bins. Thus, the frequency interval was $\Delta f = 114\,\text{GHz}/2^{16} =$

1.74 MHz, which was the frequency resolution. Hanning (Hann) window[70] was applied to

lower the aliasing with the tradeoff of slight widening in the main lobe.

There are several peaks in Figure 8(b). The highest peak corresponded to the RW (Rayleigh

wave) mode. The DC frequency (zero frequency) peak along with its weak side lobes was

ignored as it didn't carry any information. Several low frequency peaks often appear in the

frequency domain, they were thought to be associated with the eigen-mode of the PDMS

film itself as their positions do not change with sample positions or orientations. The

higher-frequency lower-intensity peak, if it emerged, was the result of the harmonics of the

PDMS film since it was always at exactly twice the frequency of the RW peak. Generally,

the RW peak was obvious to locate and the SAW velocity was then just the product of the

wavelength and the RW frequency.
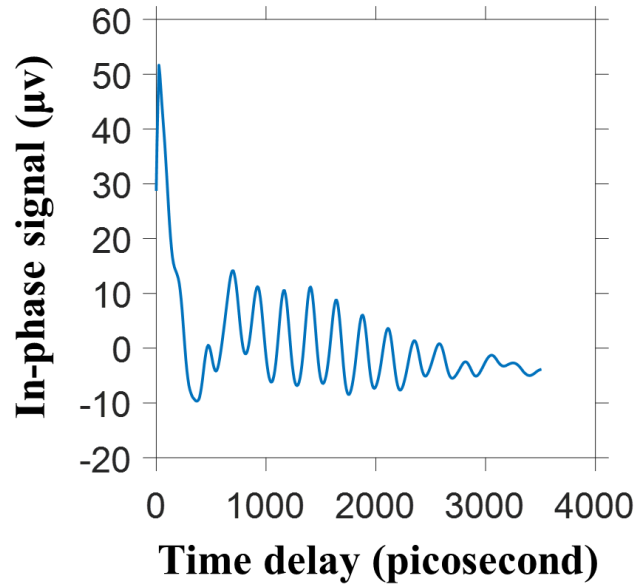
(a)
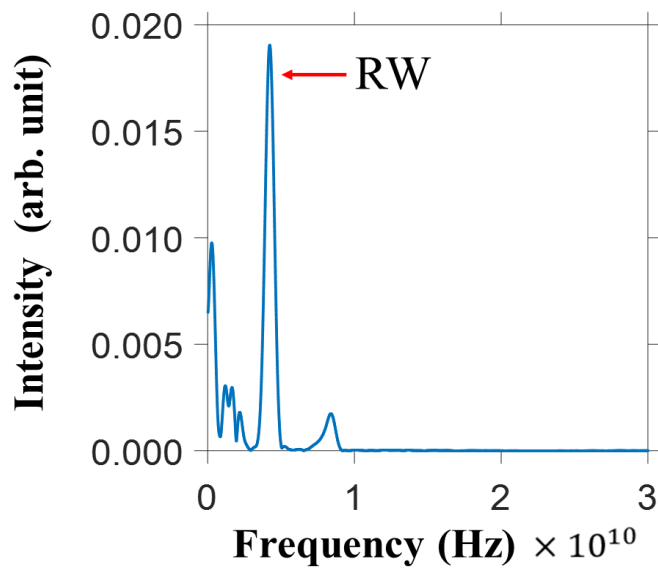
(b)

Figure 8. Example outputs from a TDTR measurement showing in both (a) the time domain and (b) the frequency domain. In the time domain, periodic modulation is due to the interaction of the SAW with the PDMS parallel line grating, which leads to a temporary standing wave before it dies out. The SAW velocity is equal to the wavelength (700 nm) times the SAW frequency.

3.5 Benchmark results and discussion

The experimentally measured SAW velocities on the nine locations as shown in Figure 5 along the same reference direction (one PDMS film orientation) are listed in Table 1. The SAW velocities calculated with reference elastic constants (single-crystal data from the literature) are listed as V_{model}. The corresponding grain orientations, PDMS orientation and differences between modeling velocities and measured velocities ($V_{expt.}$) are also listed in the table.

It can be seen from the table that the velocity measurements were robust and had good repeatability. As mentioned before, the frequency resolution was 1.74 MHz, and the PDMS film period was 700 nm. Therefore, the velocity resolution was 1.22 m/s, which has sufficient accuracy in the SAW velocity range. The resultant differences of the acoustic velocities between V_{model} values and measurements ($V_{expt.}$) were less than 3.1%, showing excellent agreement.

The experimental velocities for the pure Ni sample spanned a range of 518.3 m/s, which occupied roughly 80% of the total range of 663.5 m/s that could be spanned due to the anisotropy of Ni. This wide spread of velocity guaranteed a good convergence in the forward simulation to obtain elastic constants as to be discussed in the next chapter. Since the measured and computed SAW velocities were close to each other, we could expect the

extracted elastic constants from this experiment to be also close to the reference elastic constants.

Table 1. Comparison of the SAW velocities between experiments and modeling.

Grain	Euler angles (radian)			PDMS orientation (degree)	V_{model} (m/s)	$V_{\text{expt.}}$ (m/s)	Difference (%)
G1	6.1857	2.2641	4.6373	8.0	2976.2	2886.7	3.1
G2	4.3537	2.4559	5.6268	8.0	2437.3	2396.0	1.7
G3	1.3703	1.5124	5.9412	8.0	2902.2	2914.3	-0.4
G4	4.9150	2.7210	0.9819	8.0	2621.7	2612.7	0.3
G5	4.8803	2.7069	5.6597	8.0	2629.6	2640.3	-0.4
G6	1.8460	1.5427	0.1308	8.0	2868.9	2812.3	2.0
G7	1.8413	1.5579	0.1312	8.0	2866.5	2808.1	2.1
G8	1.3812	1.5116	5.9108	8.0	2907.0	2897.3	0.3
G9	1.3606	1.5239	5.9416	8.0	2895.0	2899.4	-0.2

Pure metal samples of Ta, Nb, Fe, Co and Sn were sectioned, mounted, girded and polished in the same process as we did for Ni. Al was very soft, so it was grinded through 400, 600, 800, 1200 grit size of sand paper and then subject to an electron-polishing as the final sample preparation step. The electro-polishing solution was a mixture of 800 mL absolute ethanol and 200 mL 70% perchloric acid. Stainless steel was used as the cathode. The

sample was roughly 2 cm in height and clamped between the cathode and a cushion immersed in the electrolyte. A very good shining surface was obtained after electron-polishing for 1 minute under the current 2.5 A (40 V).

The SAW signal was relatively weak for Ta, so a very thin Al film (less than 20 nm) was deposited as an effective transducer to enhance the signal intensity. The coating was done through a PVD (Physical Vapor Deposition) sputtering machine, where Al target was vaporized into gas phase in high vacuum due to electron bombardment and deposited onto the surface of Ta sample. The coating thickness could be well controlled by setting the sputtering power and time. High vacuum and good surface was required to guarantee a good quality of coating.

The next step is to extract elastic constants from the experimental SAW velocities along multiple distinct crystalline directions. Ni will be used as the example to illustrate. All extracted elastic constants will be given as a benchmark for pure metal samples to check the measurement accuracy.

Chapter 4: Extraction of Elastic Constants

(This chapter is mostly based on the paper: Xinpeng Du and Ji-Cheng Zhao. Facile measurement of single-crystal elastic constants from polycrystalline samples. npj Computational Materials 3, 17 (2017).)

An elastodynamic model has been established to predict the SAW velocity along any direction provided the elastic constants and density are given, as described in Chapter 2. A TDTR-based experimental technique assisted by a 1-D PDMS grating film modulation has been developed to measure SAW velocities along various crystallographic directions on several grains of a polycrystalline sample. The next step is to find a way to extract elastic constants from the measurements of SAW velocities and orientation data. Either forward simulation or neural network machine learning can be applied, as explained below.

4.1 Forward simulation

Forward simulation: an initial value of input was put into the model and an output was obtained afterwards. Then the output was compared with experimental results and the

difference was recorded as a feedback. The input will keep updated to generate better outputs until it ends up with an output that has minimized difference with the experimental results. As this method only returns a local optimum, various initial values will be provided to get the best local minimum and considered to be the "global" minimum. This method is very useful and powerful, particularly in cases where there is no analytic solution between the input and output variables. If the output variable can be measured experimentally, and the input variables are of interest, forward simulation is adequate to apply. In our case, the SAW velocity is the output variable and can be measured experimentally. The elastic constants are the inputs we need to extract, thus forward simulation is our preferred selection here.

The searching algorithm employed for updating the input C_{ij} values in forward simulations is called Nelder-Mead simplex algorithm[71]. This algorithm looks for an optimum value of an objective function without knowing any order of derivative implicitly or explicitly, so it is one of the direct search algorithms. Assuming the number of the input variables that are of interest is n. In the beginning, the initial value is defined as x_0, which is a n-component vector, and then this algorithm forms other n points by adding each component by 5% (if that component is not zero) or 0.025% (if that component is zero) to form new points (or called vertices $x_1 \ldots x_n$). Namely,

$$x_i = x_0 + h(x_0, i) * u_i, \qquad i = 1,2,3 \ldots \ldots n \qquad (4.1)$$

42

$$\text{where } h(x_0, i) = \{ \begin{matrix} 0.05 & if \ u_i \neq 0 \\ 0.00025 & if \ u_i = 0 \end{matrix}, \quad u_i \text{ is the ith component of } x_0$$

Then it calculates the differences from $f(x_0)$ through $f(x_n)$ with the reference values (i.e. the experimental SAW velocities) and sorts them in the increasing order. The worst point x_i is discarded and replaced with a new vertex point which is generated through any one of the four types of transformation: reflection, expansion, contraction, and shrink. More details of this optimization scheme can be found elsewhere[71]. Generally, by adjusting the simplex shape, the local optimum point converges eventually.

Using Ni as the example, fixing known input parameters such as density and orientations, there were only three independent components (C_{11}, C_{12}, C_{44}) of elastic constants that needed to be determined. A random initial value (C_{11}, C_{12}, C_{44}) was provided and plugged into the model to predict SAW velocities along specified orientations listed in Table 1. The difference between the predicted V_{model} and experimental SAW velocities ($V_{expt.}$) was defined in Equation 4.2.

$$\Delta = \sum_i \left(\frac{V_{expt.} - V_{model}}{V_{expt.}} \right)^2 \tag{4.2}$$

Nelder-Mead algorithm kept updating C_{11}, C_{12} and C_{44} until the minimum difference Δ was obtained, which corresponded to a local optimum set of elastic constants (C_{11}^*, C_{12}^*, C_{44}^*). Other local optima of different initial values were also obtained through the same process.

The obtained (C_{11}*, C_{12}*, C_{44}*) that referred to the least difference in SAW velocities compared among all returned updated elastic constants was claimed as the global optimum elastic constants (C_{11}**, C_{12}**, C_{44}**) for the sample material.

In order to have uniform sampling in initial values, C_{ij} with equal spacing in the ranges of C_{11} (1GPa~800GPa), C_{12} (2GPa~300GPa), C_{44} (2GPa~300GPa) were adopted. Those C_{ij} ranges cover most of engineering materials, thus no assumption of any pre-known C_{ij} of the material was necessary.

Table 2. Comparison of the C_{ij} values for pure Ni from this study on a polycrystalline sample with single-crystal data reported in the literature[72].Table 2 compares the extracted elastic constants by the forward simulation and the reference elastic constants of Ni from single-crystal measurement[72], showing that the extracted elastic constants are within 3.5% deviation. The difference was even smaller than those in the SAW velocity measurements (Table 1). The reason might be that SAW velocity data from nine orientations were used to evaluate only three independent C_{ij} values (variables). More measurements along distinct orientations could assist the convergence and hence decrease the error. It turns out that more locations for measurements could help counteract the differences in velocity measurements but the tradeoff was the increased computing time spent in the forward calculation. The adequate number of grains (crystalline directions) needed to obtain the elastic constants was a function of the number of the independent components of elastic constants, which will be discussed later.

44

Table 2. Comparison of the C_{ij} values for pure Ni from this study on a polycrystalline sample with single-crystal data reported in the literature[72].

	Extracted C_{ij} (GPa) from the polycrystalline sample	Reference C_{ij} (GPa) from single crystals	Difference
C_{11}	256.5	248.1	3.4%
C_{12}	151.5	154.9	-2.2%
C_{44}	123.9	124.2	-0.2%

In addition to Ni, the elastic constants measurements of Al, Ta, Nb and Fe (bcc), Co (hcp) and β-Sn (tetragonal) were also performed. All the results of this study are listed in Table 3 in comparison with those reference elastic constants[72–78] obtained from single crystals.

It is noted that, Al has a very low anisotropy, and thus the normal initial value setting can only lead to accurate C_{44} and anisotropic ratio. In other words, only C_{44} and C_{11}-C_{12} can be accurately extracted for the typical forward simulation setting. In order to also obtain accurate C_{11} and C_{12}, the number of initial sets was increased and the step size was much reduced to result in the reported C_{ij} values in Table 3 and Figure 9.

Table 3. Comparison of the elastic constants of seven pure metals obtained from polycrystalline samples of this study with those obtained from single crystals reported in the literature[72–78].

Sample	C_{11} (GPa)			C_{12} (GPa)			C_{44} (GPa)		
	This study	Single-crystal data	Difference	This study	Single-crystal data	Difference	This study	Single-crystal data	Difference
Ni	256.5	248.1	3.4%	151.5	154.9	-2.2%	123.9	124.2	-0.2%
Al	105.5	106.8	-1.2%	59.5	60.4	-1.5%	27.6	28.3	-2.5%
Ta	261.7	260.2	0.6%	156.7	154.5	1.4%	79.2	82.6	-4.1%
Nb	240.1	246.5	-2.6%	141.0	134.5	4.8%	29.7	28.7	3.5%
Fe	224.7	226.0	-0.6%	135.9	140.0	-2.9%	109.9	116.0	-5.3%
Co	306.7	307.1	-0.1%	170.0	165.0	3.0%	70.4	75.5	-6.8%
Sn	71.1	72.4	-1.7%	57.3	58.5	-2.1%	21.3	22.0	-3.1%
Sample	C_{13} (GPa)			C_{33} (GPa)			C_{66} (GPa)		
	This study	Single-crystal data	Difference	This study	Single-crystal data	Difference	This study	Single-crystal data	Difference
Co	105.7	102.7	2.9%	363.5	358.1	1.5%			
Sn	39.5	37.4	5.6%	84.2	88.3	-4.6%	23.4	24.4	-4.3%

Figure 9 summarizes all the results in this benchmark study, showing an excellent agreement with all the 26 C_{ij} values from polycrystalline samples to be within 7% deviation from those measured from single crystals.
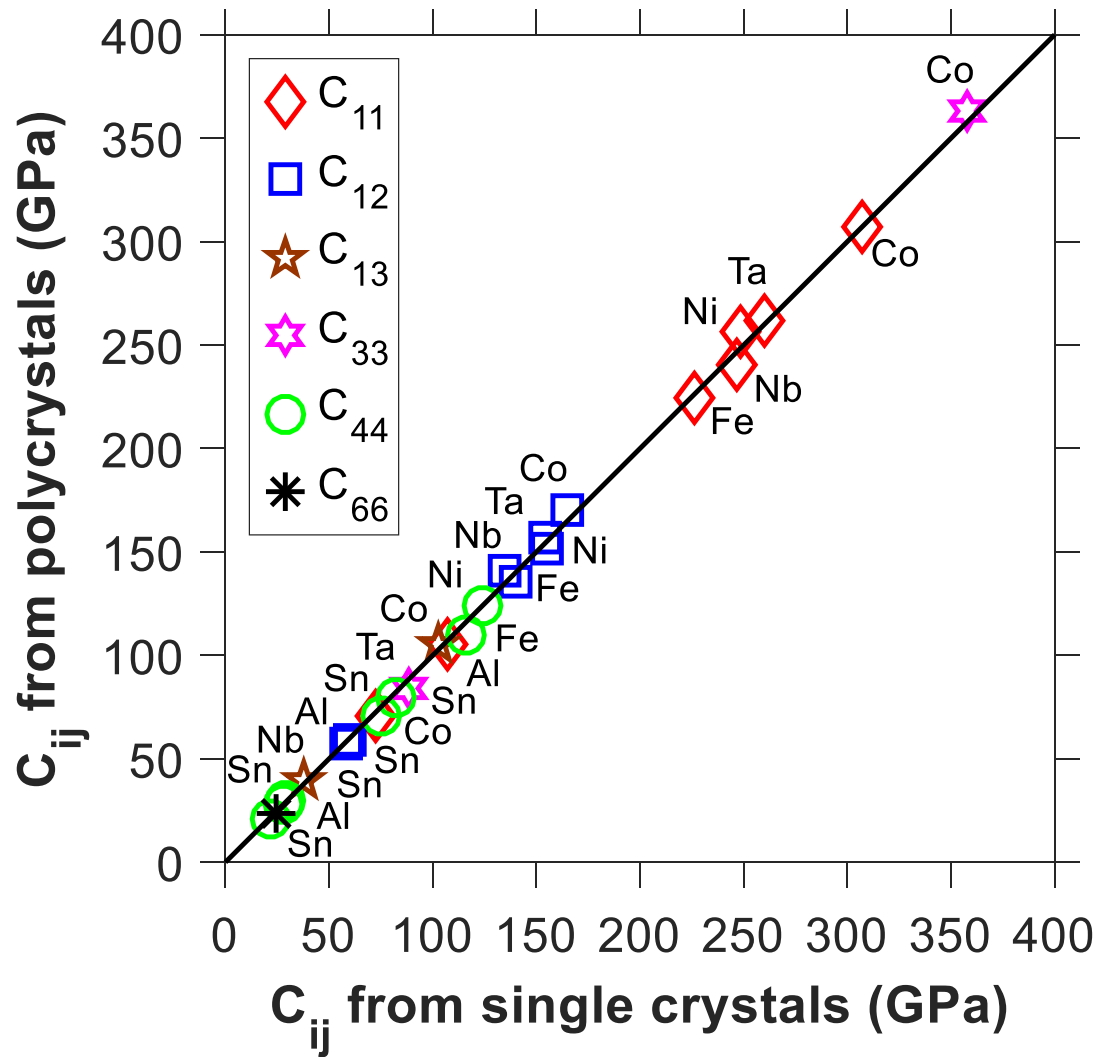
Figure 9. Comparison of the elastic constants measured from polycrystalline Al, Co, Fe, Nb, Ni, Sn, and Ta samples using ultrafast laser-generated SAWs with those reported in the literature measured from single crystals[72–78].

The corresponding EBSD inverse pole figures as well as the comparisons between calculated and experimental SAW velocities of the benchmark materials are all shown in Figures 10 to 15 as well as Tables 4 to 9.
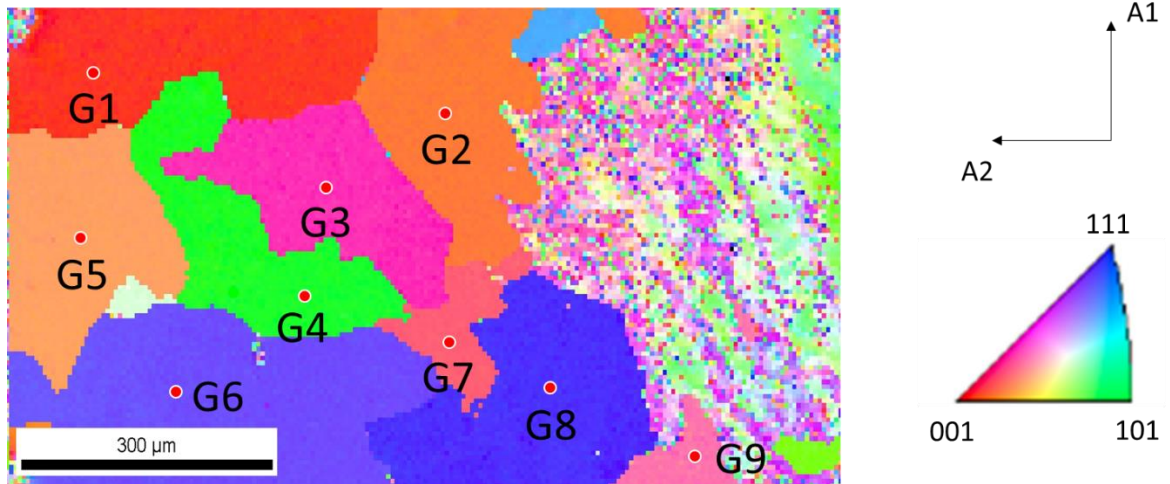
Figure 10. EBSD inverse pole figure of pure Al with the reference frame and orientation map shown. Grains selected for TDTR measurements are also labelled.

Table 4. Comparison of the experimental ($V_{expt.}$) and computed (V_{model}) SAW velocities of pure Al.

Grain	Euler angles (radian)	PDMS orientation (degree)	V_{model} (m/s)	$V_{expt.}$ (m/s)	Difference (%)
G1	3.8767 3.0891 1.9400	7.7	2973.4	2949.1	0.8
G2	3.7008 2.9686 0.1404	7.7	2924.7	2942.5	-0.6
G3	1.5903 1.3503 6.0287	7.7	2920.1	2935.8	-0.5
G4	2.3340 0.8021 3.1641	7.7	2875.7	2920.4	-1.5
G5	2.0248 0.2881 1.3565	7.7	2974.1	2933.6	1.4
G6	2.3529 1.0877 0.9211	7.7	2869.8	2913.7	-1.5
G7	3.4601 1.3748 6.1796	7.7	2950.4	2977.8	-0.9
G8	3.7851 2.1604 4.0336	7.7	2846.3	2911.5	-2.2
G9	4.0123 0.3531 0.5562	7.7	2920.4	2935.8	-0.5
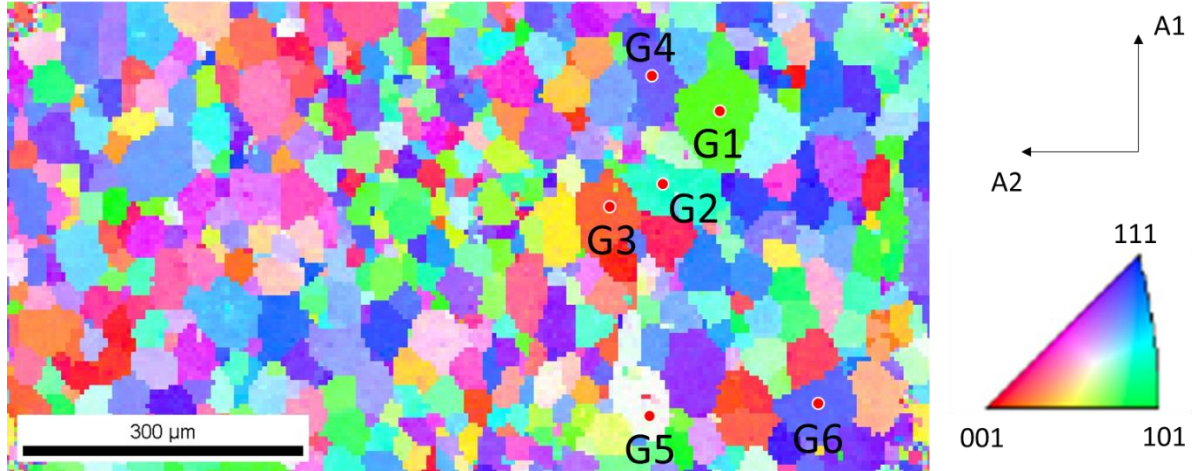
Figure 11. EBSD inverse pole figure of pure Ta with the reference frame and orientation map shown. Grains selected for TDTR measurements are also labelled.

Table 5. Comparison of the experimental ($V_{expt.}$) and computed (V_{model}) SAW velocities of pure Ta.

Grain	Euler angles (radian)	PDMS orientation (degree)	V_{model} (m/s)	$V_{expt.}$ (m/s)	Difference (%)
G1	5.7594 2.4455 6.2753	10.5	1788.7	1752.7	2.1
G2	5.3614 1.3642 2.3662	10.5	1835.6	1854.6	-1.0
G3	4.6369 1.4480 4.7503	10.5	1936.8	1936.6	0.0
G4	5.3198 2.3721 2.4608	10.5	1787.8	1709.0	4.6
G5	3.1384 0.5328 1.2012	10.5	1806.4	1718.7	5.1
G6	5.3074 1.1003 2.2656	10.5	1768.6	1738.1	1.8
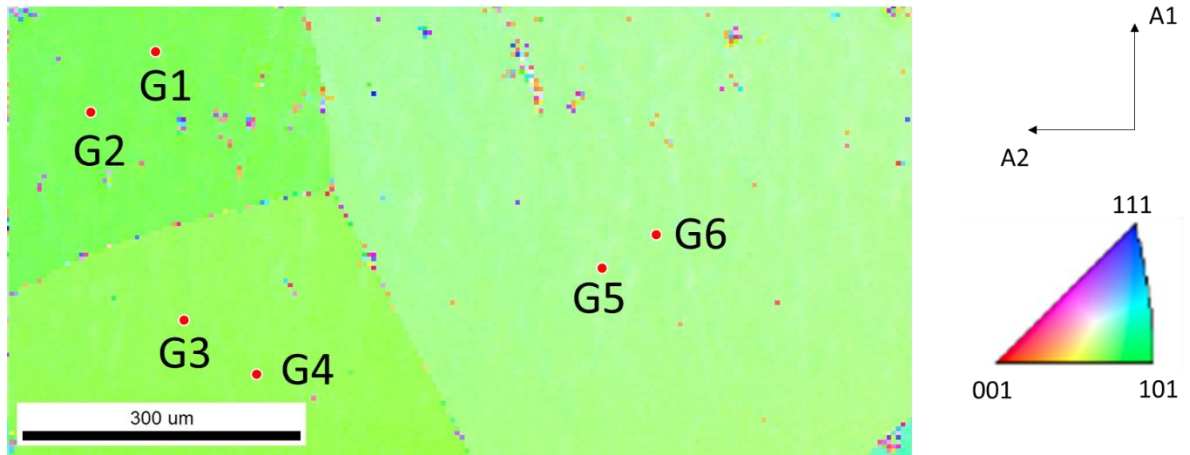
Figure 12. EBSD inverse pole figure of pure Nb with the reference frame and orientation map shown. Grains selected for TDTR measurements are also labelled.

Table 6. Comparison of the experimental ($V_{expt.}$) and computed (V_{model}) SAW velocities of pure Nb.

Grain	Euler angles (radian)	PDMS orientation (degree)	V_{model} (m/s)	$V_{expt.}$ (m/s)	Difference (%)
G1	1.4057 1.6255 4.0600	87.4	1806.6	1849.8	-2.3
G2	1.4129 1.6148 4.0729	87.4	1806.5	1840.1	-1.8
G3	1.5425 1.6205 4.1218	87.4	1795.9	1810.9	-0.8
G4	1.5407 1.6249 4.1317	87.4	1795.9	1820.7	-1.4
G5	5.9371 2.5579 6.0806	87.4	1841.5	1849.8	-0.4
G6	5.9457 2.5582 6.0868	87.4	1841.6	1883.8	-2.2
G7	4.4008 0.9500 3.9222	87.4	2027.0	2039.1	-0.6
G8	2.4648 1.1112 5.1327	87.4	1988.8	2024.6	-1.8

50

As the Nb grain size in this EBSD region is too big to obtain enough anisotropic grain

orientations. Two more locations outside the displayed EBSD region were selected for
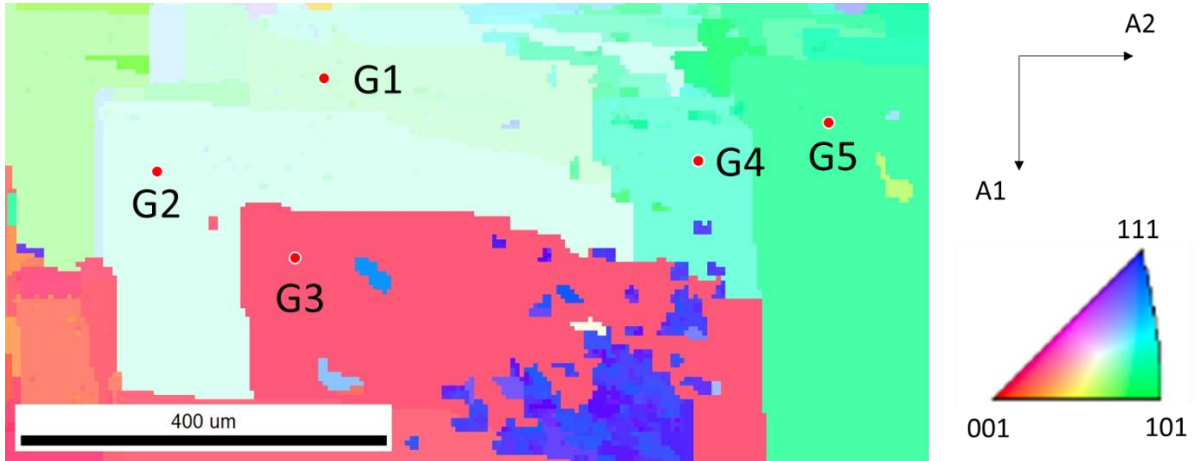
TDTR measurements.

Figure 13. EBSD inverse pole figure of pure bcc Fe with the reference frame and orientation map shown. Grains selected for TDTR measurements are also labelled.

Table 7. Comparison of the experimental ($V_{expt.}$) and computed (V_{model}) SAW velocities of pure bcc Fe.

Grain	Euler angles (radian)	PDMS orientation (degree)	V_{model} (m/s)	$V_{expt.}$ (m/s)	Difference (%)
G1	5.7594 2.4455 6.2753	147.6	2633.1	2621.7	0.4
G2	5.3614 1.3642 2.3662	147.6	2734.4	2607.2	4.9
G3	4.6369 1.4480 4.7503	147.6	2555.2	2544.1	0.4
G4	5.3198 2.3721 2.4608	147.6	2598.3	2665.4	-2.5
G5	3.1384 0.5328 1.2012	147.6	2720.7	2699.4	0.8
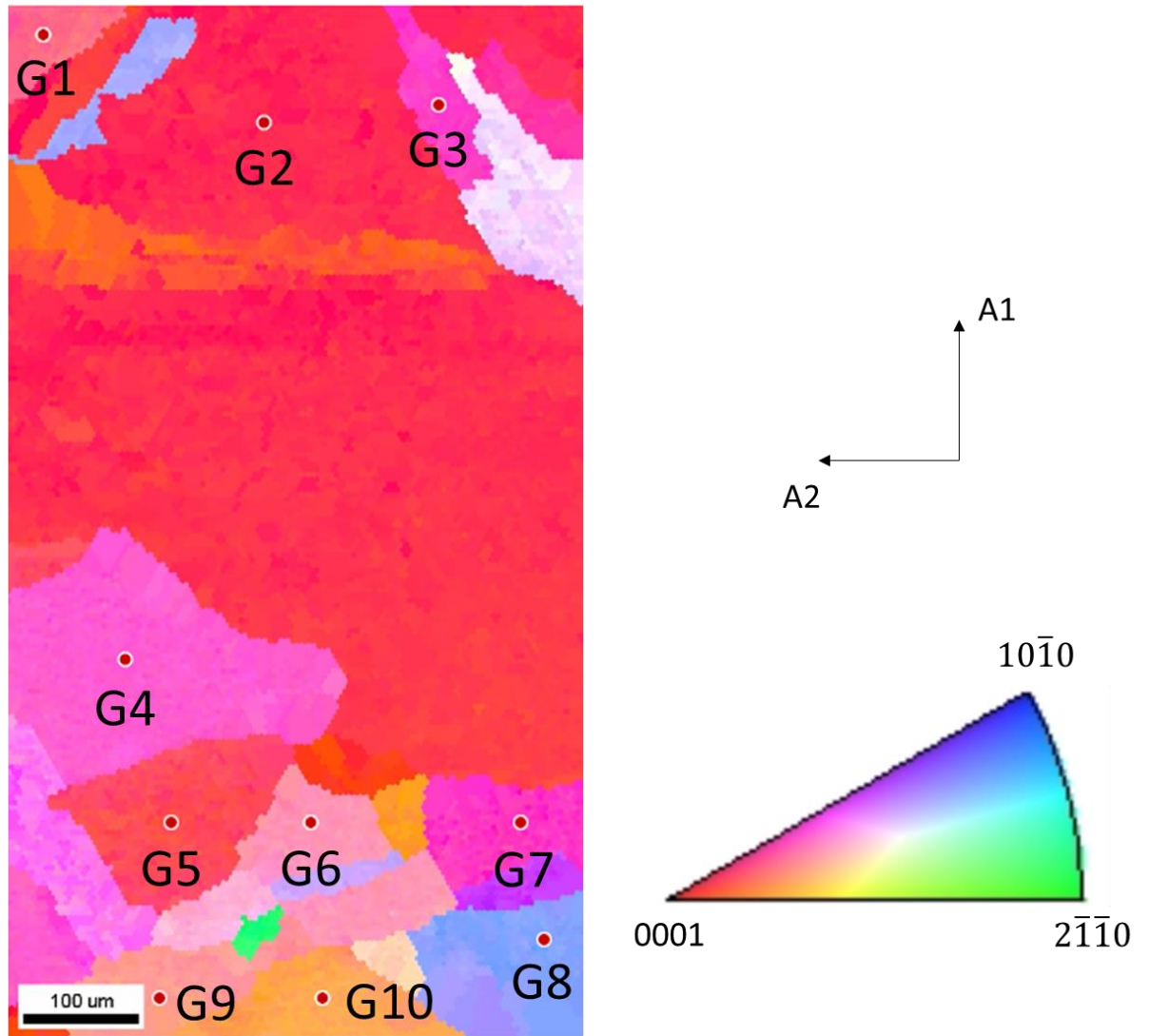
Figure 14. EBSD inverse pole figure of pure hcp Co with the reference frame and orientation map shown. Grains selected for TDTR measurements are also labelled.

Table 8. Comparison of the experimental ($V_{\text{expt.}}$) and computed (V_{model}) SAW velocities of pure hcp Co.

Grain	Euler angles (radian)	PDMS orientation (degree)	V_{model} (m/s)	$V_{\text{expt.}}$ (m/s)	Difference (%)
G2	0.6391 2.9570 5.3719	12.9	2738.7	2738.0	0.0
G3	3.6161 2.5231 4.1407	12.9	2775.6	2666.0	4.1
G4	5.1627 2.4531 0.1088	12.9	2740.8	2656.0	3.2
G8	1.7273 1.3540 3.2978	12.9	2649.5	2612.0	1.4
G10	2.1837 0.5584 0.6312	12.9	2775.6	2665.0	4.2
G1	1.7996 0.5106 6.0976	88.8	2829.4	2786.8	1.5
G2	0.6391 2.9570 5.3719	88.8	2734.4	2733.4	0.0
G3	3.6161 2.5231 4.1407	88.8	2719.5	2709.1	0.4
G4	5.1627 2.4531 0.1088	88.8	2806.7	2806.3	0.0
G6	4.8492 2.4256 2.9254	88.8	2829.4	2859.6	-1.1
G9	4.7569 2.4713 0.7931	88.8	2829.4	2864.5	-1.2
G1	1.7996 0.5106 6.0976	3.6	2711.1	2753.7	-1.5
G4	5.1627 2.4531 0.1088	3.6	2721.6	2747.3	-0.9
G6	4.8492 2.4256 2.9254	3.6	2684	2715.3	-1.2
G7	5.0670 2.5879 3.1229	3.6	2719.5	2755.9	-1.3
G10	2.1837 0.5584 0.6312	3.6	2753.7	2784.4	-1.1
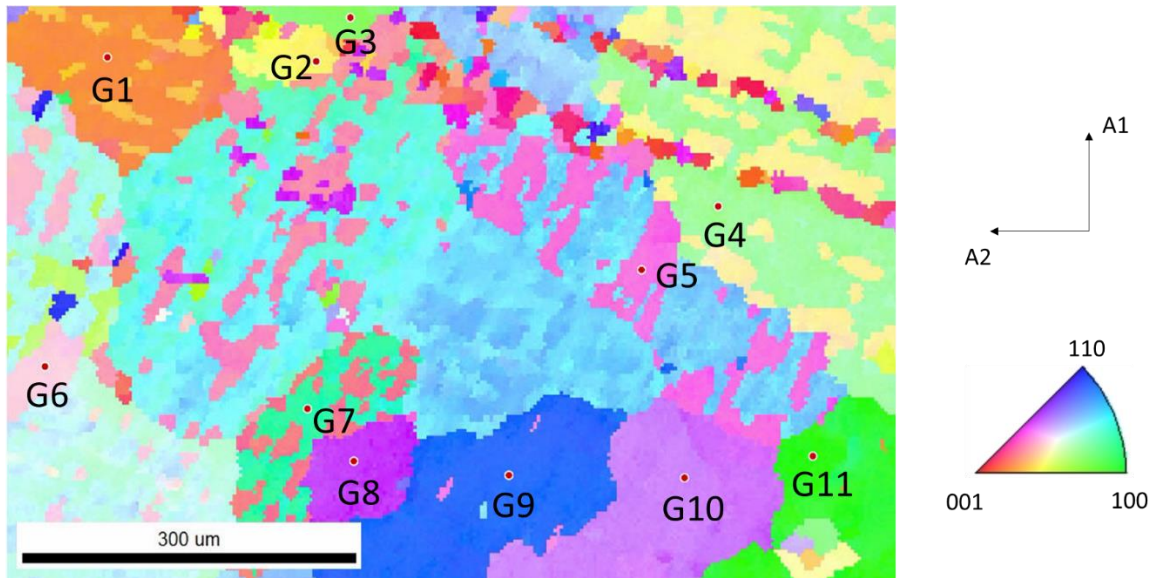
Figure 15. EBSD inverse pole figure of pure tetragonal β-Sn with the reference frame and orientation map shown. Grains selected for TDTR measurements are also labelled.

Table 9. Comparison of the experimental ($V_{\text{expt.}}$) and computed (V_{model}) SAW velocities of pure tetragonal β-Sn.

Grain	Euler angles (radian)	PDMS orientation (degree)	V_{model} (m/s)	$V_{\text{expt.}}$ (m/s)	Difference (%)
G1	1.9711 0.4182 0.1402	37.8	1375.2	1383.8	-0.6
G2	2.1866 2.3146 1.7054	37.8	1134.5	1204.0	-5.8
G3	2.0323 1.2694 4.8233	37.8	1288.2	1196.6	7.7
G4	2.5519 1.9074 0.1895	37.8	1194.5	1199.1	-0.4
G5	0.9143 0.7934 5.3464	37.8	1260.8	1262.1	-0.1
G6	1.5530 0.9348 1.9844	37.8	1302.1	1383.8	-5.9
G7	0.8741 1.5972 1.3232	37.8	1618.1	1602.3	1.0
G8	1.6460 1.5451 3.1361	37.8	1429.2	1388.8	2.9
G9	4.8375 0.9819 5.5346	37.8	1417.0	1412.6	0.3
G10	1.6646 1.6145 2.2199	37.8	1366.7	1257.0	8.7
G11	4.5249 1.0205 5.6601	37.8	1527.1	1495.2	2.1
G1	1.9711 0.4182 0.1402	44.5	1527.7	1524.6	0.2
G2	2.1866 2.3146 1.7054	44.5	1234.6	1165.5	5.9
G3	2.0323 1.2694 4.8233	44.5	1298.7	1286.6	0.9
G4	2.5519 1.9074 0.1895	44.5	1254.0	1250.2	0.3
G5	0.9143 0.7934 5.3464	44.5	1191.7	1223.6	-2.6
G6	1.5530 0.9348 1.9844	44.5	1399.4	1398.6	0.1
G7	0.8741 1.5972 1.3232	44.5	1617.4	1665.3	-2.9
G8	1.6460 1.5451 3.1361	44.5	1382.3	1434.7	-3.7
G9	4.8375 0.9819 5.5346	44.5	1339.5	1271.9	5.3
G10	1.6646 1.6145 2.2199	44.5	1292.0	1325.1	-2.5
G11	4.5249 1.0205 5.6601	44.5	1479.9	1405.6	5.3

The forward simulation can extract elastic constants, especially for cubic materials, but the computing time is an issue worth considering. Based on experience on many samples, the number of crystallographic orientations needed to extract elastic constants are listed in Table 10, together with the number of independent components of elastic constants and computing time spent in the forward simulations. For cubic crystals, for instance, there are three independent components of elastic constants and hence more than three SAW velocity measurements along different directions (preferred to be selected on different crystalline planes) are required to extract the full elastic constants. To increase the convergence rate and decrease the experimental error, five or more velocity measurements were often performed. The computing time spent to find the best-match C_{ij} values is 18 h for 72 sets of initial C_{ij} inputs. This computing time is acceptable. But for low crystalline symmetry materials, say the monoclinic class, there are 13 independent elastic constants to be determined. The computing time spent was more than one hundred hours for just 8 initial sets of values for 63 measured SAW velocities. The forward-simulation algorithm still did not reach an acceptable minimum since each set of input C_{ij} values leads to a different local minimum, as to be described in the next chapter for Ni_3Sn_4. The large ranges of elastic constants in each C_{ij} bring a tremendous challenge to initial value sampling in forward simulations in terms of time efficiency.

Table 10. Computing time in forward simulations for different situations. The number of independent elastic constants in different crystal classes, the number of velocity measurements used to extract elastic constants, and the number of initial values are all affecting the time needed in forward simulations.

Crystal Class	Independent # of C_{ij}s	# of SAW measurements	Computing time
Triclinic	21		
Monoclinic	13	63	>100h for 8 sets
Orthorhombic	9		
Tetragonal	7 (or 6)	20	65 h for 24 sets
Trigonal	7 (or 6)		
Hexagonal	5	10	36 h for 64 sets
Cubic	3	5	18 h for 72 sets
Isotropic	2	/	/

4.2 Neural network machine learning

To solve the computing time issue, the neural network machine learning approach, in addition to the forward simulations, has been employed to achieve faster extraction of elastic constants.

Neural network (or artificial neural network) is a method that imitates how human brain works in perceiving and solving problems. This method was first developed in 1943 by Warren McCulloch and Walter Pitts[79]. The principle is to employ many artificial neurons linking each other in a layered structure. Each neuron will be stimulated or inhibited by surrounding neurons in the 'signal' transition process. By providing inputs and expected

57

outputs, neurons will each get trained to have the right weighs to respond. Eventually, a model connecting the inputs and outputs will get established. Even through the model is not explicitly obtained, the network can work well in providing numerical solutions.

There are many types of neural networks. the most widely used type is Feedforward network, which doesn't need any recurrent feedback connections, thus there is no ring or loop in neurons of the Feedforward networks. The Feedforward networks are extensively used in pattern recognition, nonlinear fitting function and predictions.

Assuming a cubic crystal material and SAW velocities have been measured for five directions. A lot of sets of C_{11}, C_{12} and C_{44} are randomly generated and used to calculate the SAW velocities for the same five directions through the elastodynamic model. Those [C_{11}, C_{12}, C_{44}; v1, v2, v3, v4, v5] pairs are subject to the neural network training program in MATLAB Neural Network toolbox for training. The purpose is to get back a function (network) that can extract the relation between C_{ij} and SAW velocities. When five experimental velocities along specified directions are provided into the network, the full elastic constants can be automatically extracted directly, skipping any searching iteration in forward simulations. This application of neural network has been demonstrated to obtain the same C_{ij} values as the forward simulations. Applications of the neural network method to other materials will be given in Chapter 5.

Chapter 5: Applications

In addition to the benchmark work on polycrystalline pure metals, the new SAW-PDMS-TDTR-MODEL method has been applied to the measurements of: (1) composition-dependent elastic constants of Fe-Ni diffusion couple; (2) elastic constants from powder Sn sample; (3) the elastic constants of intermetallic compound Ni_3Sn_4 of monoclinic crystalline symmetry; (4) the full elastic constants of Ni-based superalloy René 88DT; and (5) Young's modulus of inorganic glass materials. These examples are described in detail in this Chapter.

5.1 Measurement of composition-dependent elastic constants from an Fe-Ni diffusion couple

As mentioned before, elastic constants are essential for both physics-based mechanical modeling[80–82] and simulation of micro-structural evolution[83–85]. Elastic constants as a function of composition are needed to take into account the compositional effect on the elastic constants. Without such data, the anisotropic properties of the pure elements and

linearly interpolated data are often used as model inputs, which can lead to significant error in the simulated/computed properties.

The Vegard's law of the linear dependence of elastic constants on composition[86,87] works for some systems but fails for others[88]. Various calculation methods have also been developed to calculate elastic constants, including valance force field methods[89,90], ab-initio first-principles calculations[5–10] and molecular dynamics (MD)[11–14]. The computed results are better than linear interpolation, but still not as reliable as accurate experimental measurements.

Composition-dependent elastic constants have been measured for several material systems[91–95] using single crystals of individual compositions, which is quite time-consuming and labor-intensive. For this reason, only a few systems have such detailed measurements been performed.

The high-throughput diffusion multiples[96–99] generate composition gradients through high-temperature interdiffusion of elements. The idea here is to perform localized elastic constant measurements on the composition gradient to obtain composition-dependent elastic constants without making single crystals of individual compositions.

5.1.1 Sample preparations and characterizations

The Co-Cr-Fe-Mo-Ni diffusion multiple used for the current measurements was made by Dr. Siwei Cao during her Ph.D. study at Ohio State, as described in detail elsewhere[100]. All pure bulk metals were from commercial sources with a purity of Ni (99.9%), Fe (99.8%), Co (99.9%), Mo (99.95%) and Cr (99.9%). All sample pieces were cut by EDM (electro-discharge machining) and then well grinded and polished before they were assembled into a pure Ni cartridge. Then the assembled sample was subject to HIP (hot isostatic pressing) after it was sealed under vacuum during electron-beam welding. The HIP was conducted at 1200 °C under 207 MPa pressure of argon for 8 h. The sample was encapsulated in a quartz tube filled with argon for heat treatment at 1200 °C for 500 h.

The sample was water quenched to room temperature and a slice of sample of ~ 5 mm in thickness was cut off and was grinded and polished through 240, 400, 600, 800, 1200 grit size of sand paper, 1 μm diamond paste and then 0.05 μm colloidal silica suspension to obtain a high-quality metallographic finish. The final appearance of the sample is displayed in Figure 16.

61

Figure 16. Photo of the polished Co-Cr-Fe-Mo-Ni diffusion multiple sample after being assembled, HIPed and heat treated. The sample was glued to a bakelite mount for experimental convenience.

The brick-laying elements can be seen in Figure 17, creating ten diffusion couples as well as eight diffusion triples (two repeats). The Fe-Ni diffusion couple was selected as the measurement region, denoted by the double-arrow in Figure 17. This selection was based mostly on the fact that composition-dependent C_{ij} values are available in the literature (from measurements on single-crystals of many individual compositions) for this binary system for a direct comparison of the measurement accuracy of the new method.
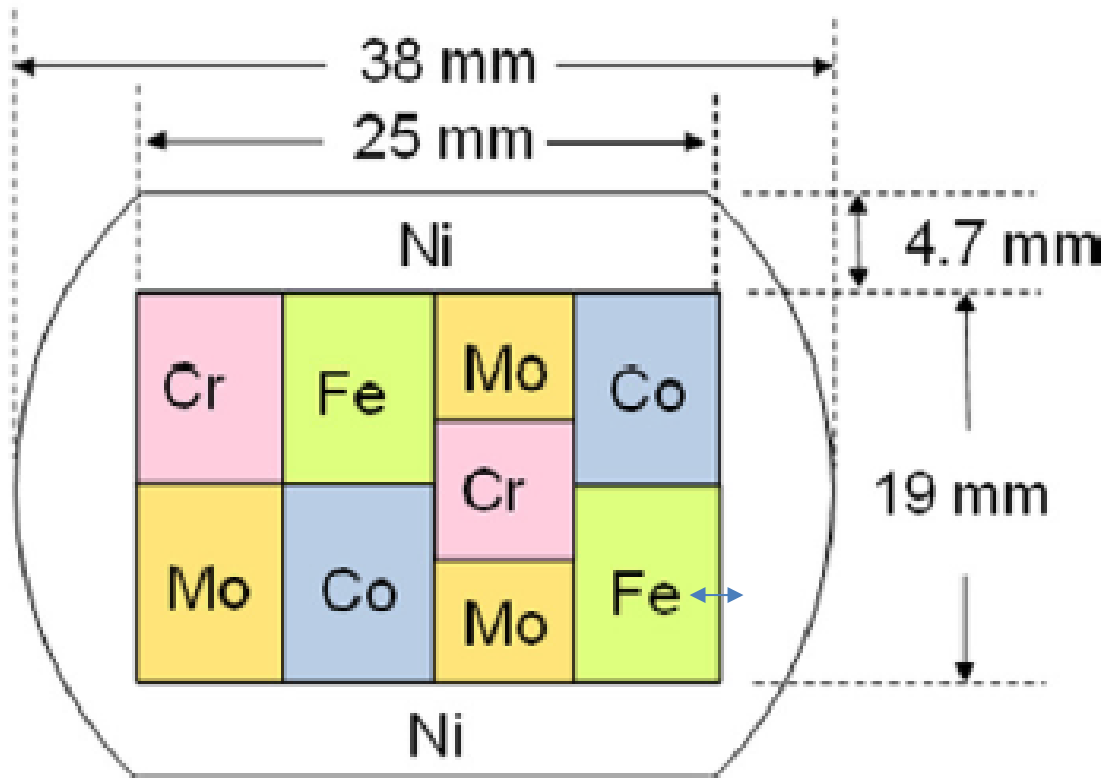
Figure 17. Schematic showing the element arrangement and the sizes of the assembled Co-Cr-Fe-Mo-Ni diffusion multiple. The double-arrow denotes the region of the Fe-Ni diffusion couple for the composition-dependent C_{ij} measurement.

Figure 18 is an optical image of the selected Fe-Ni diffusion couple region, showing Kirkendall voids in the middle and micro-indents that were placed on the region to help locate the position on the diffusion multiple and to serve as reference marks to correlate the EBSD, SAW TDTR, and composition analysis using energy dispersive spectroscopy (EDS)
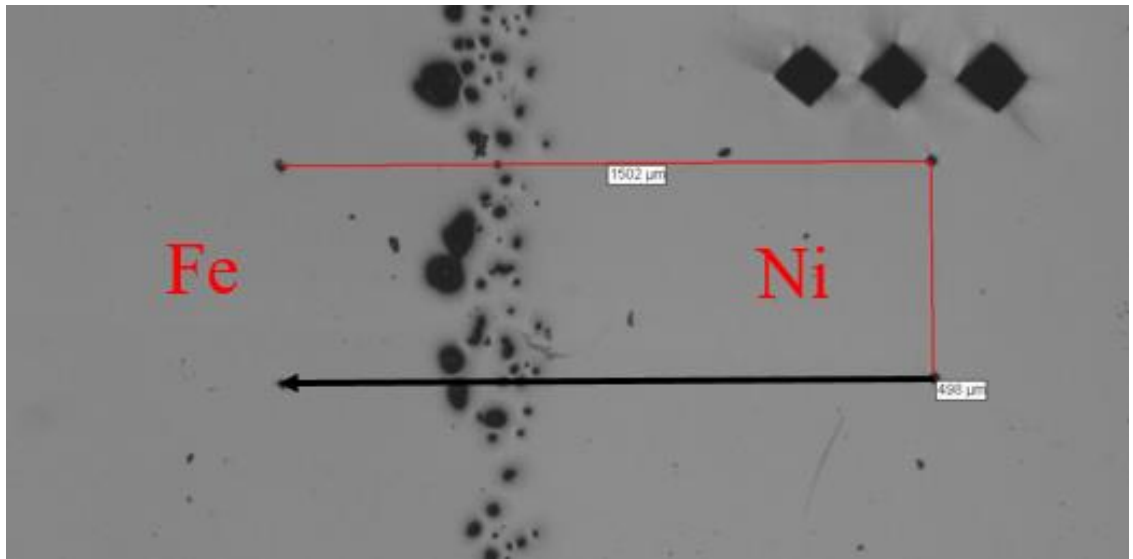
Figure 18. Optical image showing the measurement region. The 4 small corner indents denote the boundary of the entire region. The three big indents in the upper right corner were used to assist finding the region from the whole sample during characterization. The vertical column of porosity is likely due to Kirkendall voiding.

The EDS composition profile was obtained using a XL-30 ESEM. The measurement was scanned along the line connecting the two top indents in the selected region across the Fe-Ni diffusion couple. The measurement was conducted at 20 kV for 0.2 s dwell time for each point with a step size of 5 μm. The composition profile is shown in Figure 19.
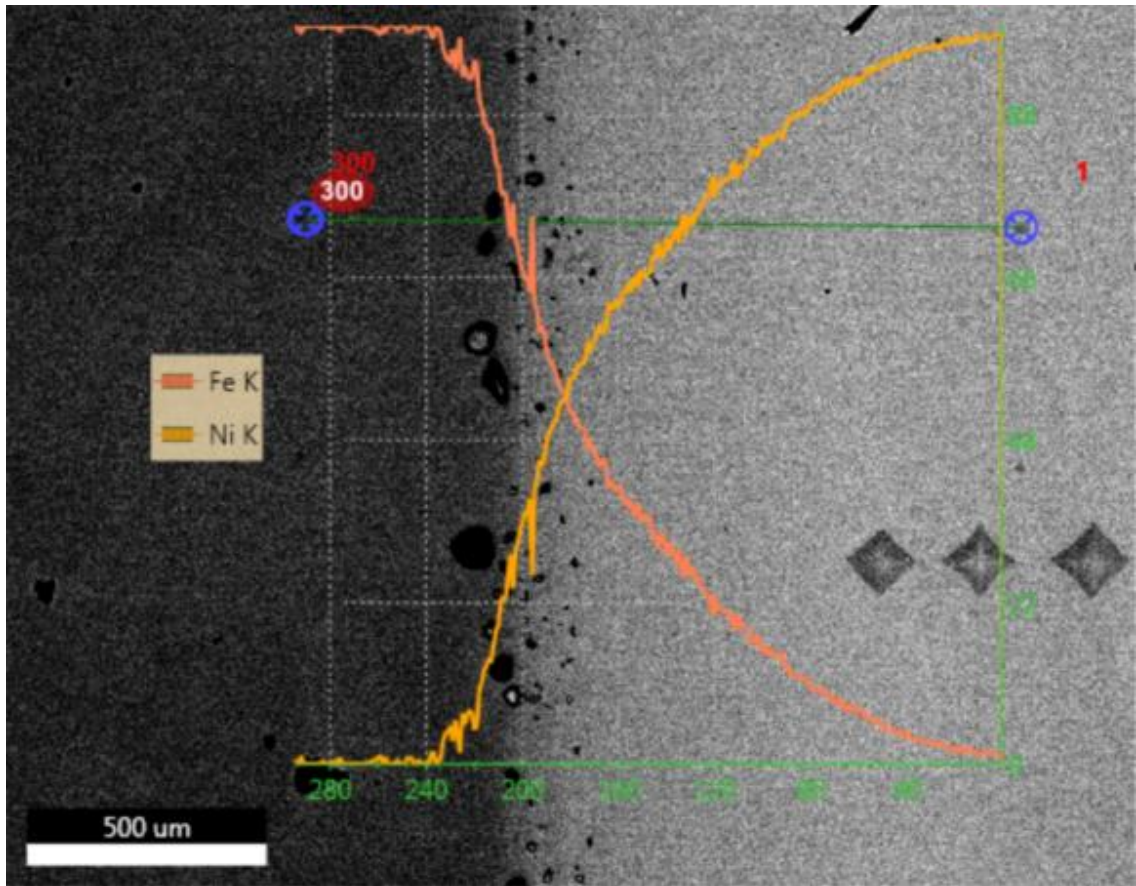
Figure 19. The composition profile of the Fe-Ni diffusion couple along the line as indicated by the black arrow connecting the lower two indents in Figure 18. The composition for either Fe or Ni is nearly from 0 % to 100% with a diffusion distance of ~ 1.5 mm.

EBSD equipped with XL-30 ESEM with an EDAX TSL detector was employed to map

the grain orientations. Instead of scanning a single line as in EDS, the entire selected

region was mapped for grain orientations. EBSD was performed at an accelerating

voltage of 20 kV and a working distance at 23 mm. The scanning region was 1000 μm X

500 μm from the Ni-rich side. The step size was 5 μm in both scanning directions.

Orientation data was analyzed using the software of TSL OIM Analysis from which

Euler angles (based on Bunge's convention) were obtained and put into our SAW model for 3D orientation indices. The inverse pole figure of the EBSD scanning region is shown in Figure 20.
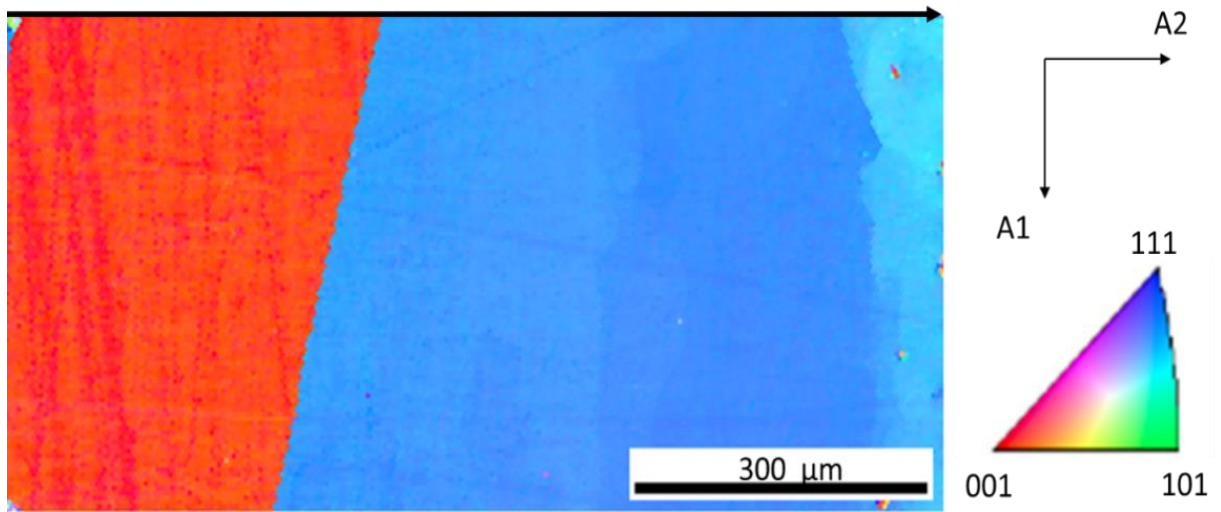
Figure 20. EBSD inverse pole figure for the indented region of the Fe-Ni diffusion couple. Sample coordinate system is also shown.

The EBSD orientation map in Figure 20 clearly shows large grain as a result of the high temperature (1200 °C) and long-duration (500 h) diffusion heat treatment. These large grains facilitate the SAW velocity measurements but limits the number of distinct crystallographic orientations. PDMS film rotations were employed to increase the number of SAW velocity measurements.

As discussed before, density is an input parameter to the SAW velocity model, thus the density of the fcc phase of Fe-Ni alloys as a function of composition needs to be evaluated. Figure 21 shows the data obtained and summarized by Tomlinson and Andrews[101]. The composition-density curve deviates significantly from the Vegard's law, with a minimum density around Fe-40Ni.

O calculated from lattice parameters
O from hydrostatic weighing
□ from Ref. 7
△ calculated hypothetical fcc structure (see text).
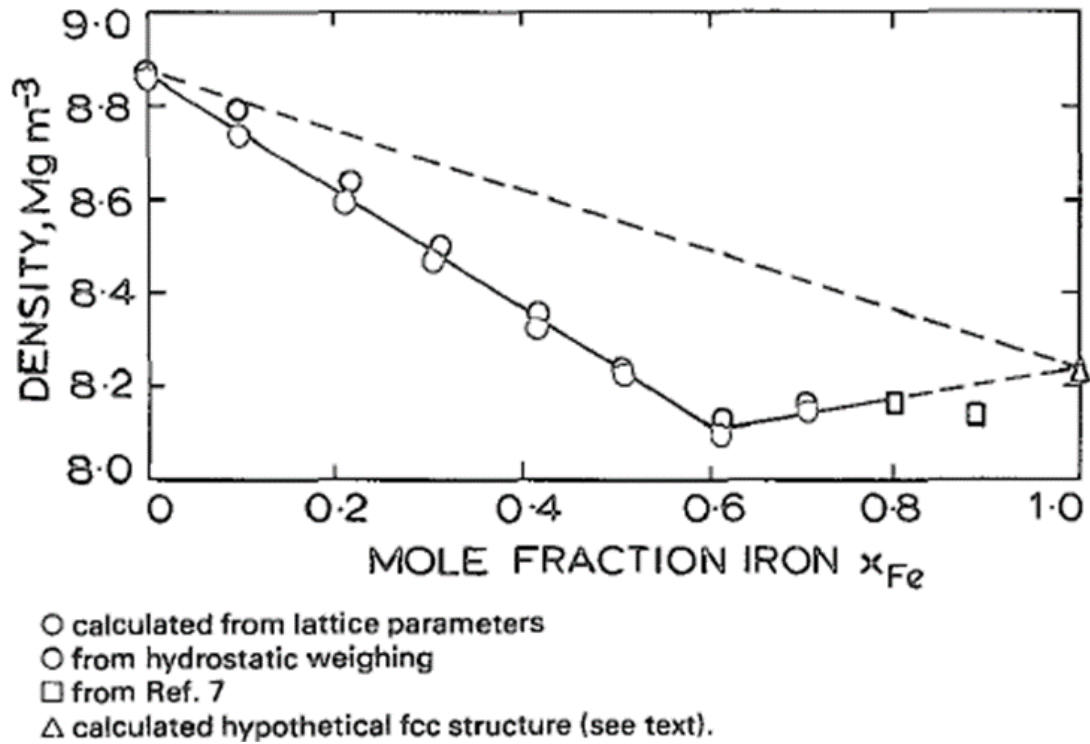
Figure 21. Composition-dependent density of Fe-Ni alloys[101].

5.1.2 SAW velocity measurements

Unlike the pure Ni case where SAW measurement can be performed at any location, the composition gradient limited the positions for SAW measurements for each composition. In order to increase the number of orientations for SAW velocity measurements with fixed position, the PDMS films were rotated for five orientations as schematically shown in Figure 22. For each PDMS film orientation, the SAW scanning was made along the pre-set scanning line denoted by the black arrows in Figure 20.

The PDMS films were randomly rotated to cover a wide range of orientations and those angles relative to the reference direction (TD direction) were measured to be [179, 84, 77, 70, 25] degrees under a light microscope, which were incorporated in the SAW velocity model as described in more detail in Appendix C.
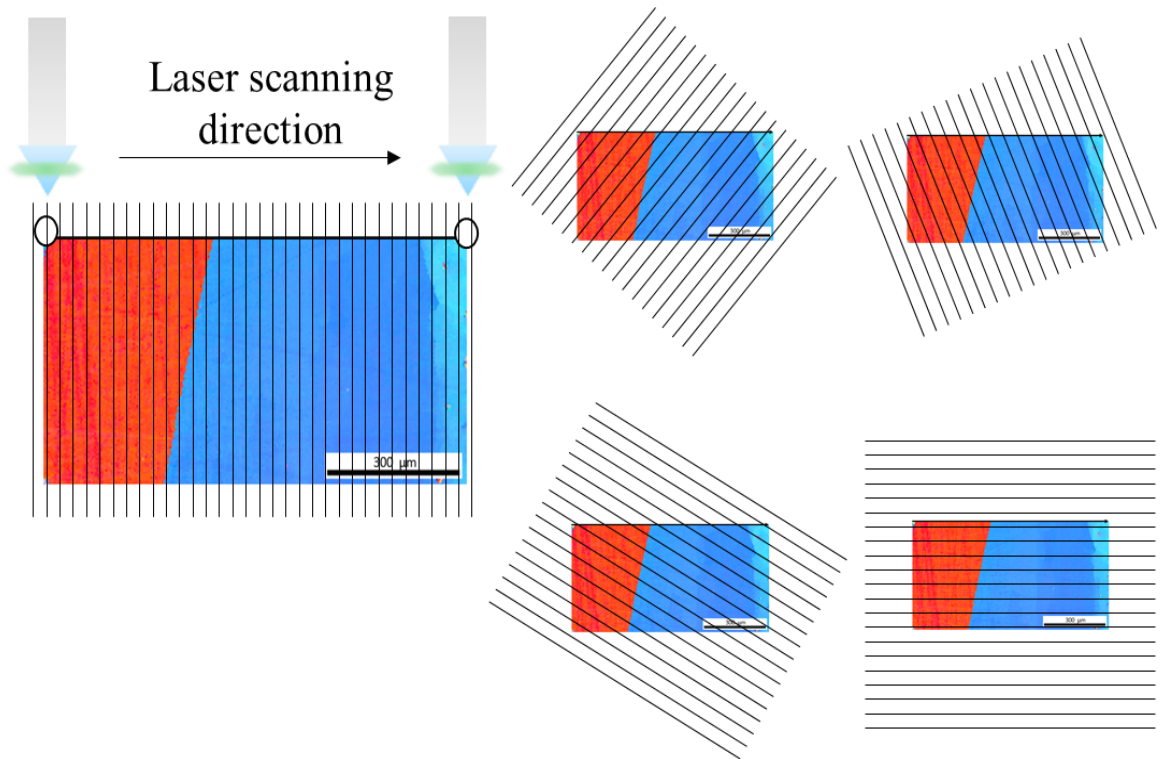
Figure 22. Laser scanning under five different PDMS film orientations along the same line as indicated by the two circles representing the starting and finishing positions
The five SAW velocity profiles as well as the Fe-Ni composition profile along the same line are displayed in Figure 23. More details can be found in Table 11.
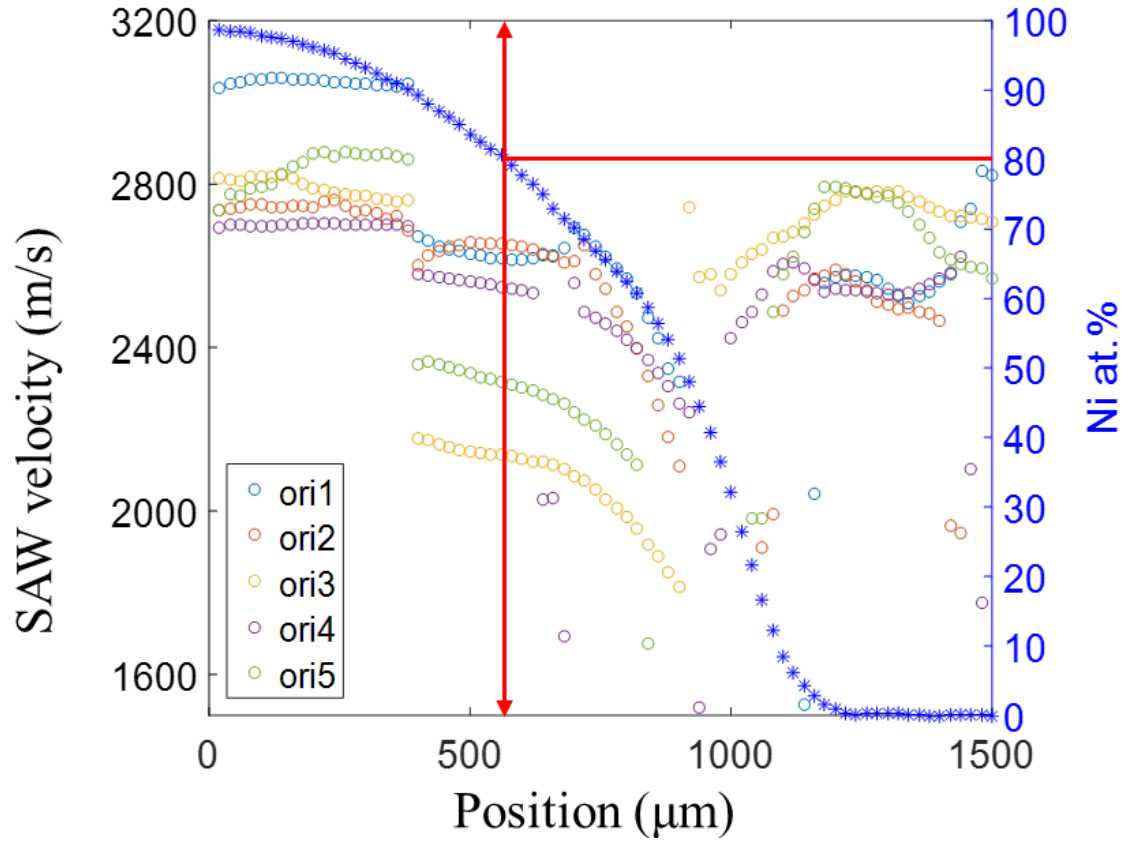
Figure 23. SAW velocities along the same scanning line under the five different PDMS film orientations. The Fe-Ni composition profile from EDS is overlaid and read from the vertical axis on the right.

Table 11. Measured SAW velocities under different crystallographic and PDMS orientations at different Ni at.%. compositions. The five PDMS orientations are 179, 80, 77, 74 and 25 degrees measured from the reference direction (transverse direction).

Position (μm)	Euler angle (radian)	Compo-sition Ni at.%	$V_{expt.}$ (m/s) PDMS Ori-1	$V_{expt.}$ (m/s) PDMS Ori-2	$V_{expt.}$ (m/s) PDMS Ori-3	$V_{expt.}$ (m/s) PDMS Ori-4	$V_{expt.}$ (m/s) PDMS Ori-5
20	0.1445 1.1793 0.8278	98.6	3034.4	2737.0	2814.7	2693.3	2734.6
40	0.1624 1.2680 0.8122	98.4	3049.0	2752.8	2808.7	2705.5	2772.2
60	2.0824 0.8055 1.0850	98.4	3049.0	2729.8	2803.8	2706.7	2814.7
80	0.1983 1.2020 0.8247	98.2	3059.9	2749.2	2797.7	2692.1	2772.2
100	2.0999 0.7992 1.0789	97.9	3057.5	2743.1	2809.9	2695.8	2769.8

120	0.1808 1.2004 0.8184	97.7	3062.3	2780.7	2859.6	2689.7	2814.7
140	0.1749 1.1423 0.8173	97.3	3051.4	2750.4	2823.2	2707.9	2794.1
160	0.1854 1.1480 0.8146	96.9	3067.2	2693.3	2805.0	2703.1	2854.8
180	0.1889 1.1540 0.8117	96.5	3057.5	2746.8	2800.2	2701.8	2883.9
200	3.3325 1.9923 0.7572	96.2	3050.2	2767.4	2782.0	2704.3	2859.6
220	0.1838 1.1322 0.8126	95.7	3047.8	2778.3	2785.6	2701.8	2877.8
240	0.1890 1.1408 0.8168	95.2	3049.0	2726.1	2775.9	2703.1	2897.3
260	3.3316 1.9904 0.7522	94.4	3052.6	2766.2	2782.0	2705.5	2871.8
280	2.1711 0.8423 0.9861	93.9	3044.1	2767.4	2767.4	2699.4	2839.0
300	0.1797 1.1491 0.8182	93.1	3047.8	2699.4	2763.7	2698.2	2899.7
320	0.1775 1.1487 0.8283	92.4	3035.6	2701.8	2773.5	2699.4	2869.3
340	0.1781 1.1544 0.8209	91.6	3038.1	2743.1	2767.4	2704.3	2870.6
360	0.1743 1.1574 0.8277	90.9	3034.4	2740.7	2743.1	2694.6	2869.3
380	0.1775 1.1680 0.8201	90.0	3044.1	2684.5	2760.1	2698.2	2862.1
400	2.1520 0.8262 1.0087	89.2	2670.3	2601.9	2178.7	2579.3	2359.6
420	2.1611 0.8278 1.0016	88.1	2656.9	2636.3	2182.4	2579.3	2364.4
440	0.1815 1.1706 3.9629	87.0	2656.9	2635.1	2160.5	2573.2	2375.3
460	3.3254 1.9713 0.7618	86.1	2632.7	2659.4	2155.7	2567.1	2358.3
480	0.1842 1.1566 0.8139	85.0	2625.4	2653.3	2145.9	2567.1	2337.7
500	2.1471 0.8381 1.0136	83.6	2621.7	2646.0	2138.7	2563.5	2330.4
520	0.1772 1.1667 0.8124	82.6	2649.7	2665.4	2141.1	2558.6	2326.8
540	0.1760 1.1680 0.8125	81.5	2615.7	2656.9	2150.8	2556.2	2334.1
560	0.1718 1.1660 0.8112	80.6	2610.8	2652.1	2138.7	2551.3	2313.4
580	0.1697 1.1663 0.8121	79.1	2598.7	2649.7	2124.1	2540.4	2308.6
600	0.9828 3.0821 0.0130	77.6	2621.7	2649.7	2133.8	2539.2	2300.1
620	4.1106 1.6521 3.1325	76.5	2629.0	2644.8	2119.2	2535.6	2297.7
640	4.1045 1.6290 0.0050	75.0	2609.6	2636.3	2116.8	2535.6	2298.9
660	4.1044 1.6424 3.1355	73.0	2625.4	2610.8	2110.7	2523.4	2277.0
680	4.1008 1.6517 3.1286	71.5	2643.9	2601.1	2115.6	0.0	2252.8
700	4.0977 1.6611 3.1187	70.1	2692.2	2612.0	2098.6	2559.8	2247.9
720	4.0973 1.6436 0.0086	68.4	2660.7	2652.1	2065.8	2487.0	2235.8
740	4.1039 1.6569 6.2803	66.9	2674.7	2557.4	2042.8	2477.3	2203.0
760	4.1003 1.6314 6.2718	65.6	2621.7	2531.9	2041.6	2459.1	2187.2
780	4.0907 1.6317 6.2620	63.9	2580.5	2505.2	2019.7	2439.7	2176.3
800	2.5317 1.5614 6.1788	62.5	2576.0	2463.9	1972.4	2425.1	2142.7
820	4.1064 1.6823 3.1502	60.7	2516.9	2381.4	1966.3	2403.3	2101.0
840	3.7850 0.0888 3.4536	58.7	2548.0	2375.8	1925.0	2374.1	2091.6
860	4.0998 1.6598 3.1406	56.4	2440.9	2266.6	1894.7	2343.8	2049.6
880	4.1017 1.6358 0.0384	54.0	2286.2	2163.7	1838.9	2307.4	1980.0

71

900	4.1051 1.6618 3.1413	51.3	2317.7	2111.2	1813.7	2261.2	0.0
920	0.1642 3.0802 5.4990	48.1	0.0	0.0	2742.6	2240.6	0.0
940	0.5741 3.1069 5.8983	44.5	0.0	0.0	2485.7	0.0	0.0
960	4.1016 1.6180 6.2801	40.6	0.0	2332.9	2485.8	2319.5	0.0
980	4.7449 2.5150 5.7689	36.6	0.0	0.0	2569.7	2502.8	0.0
1000	4.7449 2.5150 5.7689	32.0	0.0	0.0	2609.6	2477.3	2508.9
1020	4.7449 2.5150 5.7689	26.5	0.0	2147.2	2551.3	2408.1	0.0
1040		21.5	0.0	0.0	2675.1	2406.9	2328.2
1060		16.5	2598.4	2427.5	2638.7	2522.2	2580.5
1080		12.2	0.0	2519.8	2667.7	2619.3	2483.4
1100		8.4	0.0	2465.2	2673.9	2689.7	2510.1
1120		6.2	0.0	2551.3	2678.8	2688.5	2530.7
1140		4.3	2516.1	2485.8	2709.0	2510.1	2786.8
1160		2.9	2556.2	2613.8	2678.8	2534.3	2791.7
1180		1.6	2568.3	2592.8	2783.2	2541.6	2795.3
1200		0.9	2576.8	2601.9	2779.5	2546.5	2797.7
1220		0.3	2578.0	2585.8	2780.7	2544.1	2798.9
1240		0.2	2575.6	2564.1	2785.6	2545.3	2777.1
1260		0.3	2573.2	2547.3	2774.7	2516.1	2774.7
1280		0.3	2573.2	2506.0	2774.7	2541.6	2768.6
1300		0.3	2552.6	2493.4	2785.6	2535.6	2763.7
1320		0.3	2558.6	2451.4	2783.2	2527.1	2762.5
1340		0.1	2470.0	2522.8	2782.0	2523.4	2785.6
1360		0.0	2476.1	2504.6	2780.7	2517.4	2687.3
1380		0.0	2477.3	2516.1	2716.4	2555.0	2663.0
1400		0.0	2654.5	2432.4	2715.2	2589.0	2608.4
1420		0.1	2603.5	2433.6	2723.7	2586.5	2602.3
1440		0.1	2602.3	2443.3	2726.1	2597.5	2601.1
1460		0.1	2559.8	0.0	2721.3	2582.9	2602.3
1480		0.1	3115.7	2414.2	2717.6	2748.0	2612.0
1500		0.0	2820.8	0.0	2706.7	0.0	2567.1

The laser scanning distance was 1 mm with a 20 μm step size. In can be seen from Figure 23 that from 0 to 400 μm, velocity profiles were gradually varying and an abrupt drop in velocity profiles regardless of orientations was observed around 400 μm. This

corresponds to the transition from one grain to another (the abrupt change of the orientation from 'red' to 'blue', as seen from the EBSD inverse pole figure in Figure 22). From roughly 400 μm to 800 μm, the velocities gradually decreased within 'blue' orientation grain and the composition changed more rapidly. From 800 μm to 1200 μm, the velocities show high degree of scattering, they were regarded as unreliable data. In addition, there is a narrow strip of composition where no SAW signal could be collected. The reason leading to the scattered data might be the Invar effect of Fe-Ni alloys at the composition around Fe-36Ni, which was also roughly in the void region. Around this specific composition, the thermal expansion coefficient is very small. As the mechanism of the TDTR method was to use laser to deposit heat on a local region, the temperature gradient around the laser spot led to thermal stresses, which launched SAW. As a result, high thermal expansion coefficient could lead to a higher intensity of local displacements, and thus stronger SAWs. The small thermal expansion coefficient implied weaker SAWs, and thus reduced the signal-to-noise ratio in SAW velocity measurements, which could increase the possibility of unreliable data.

5.1.3   Extraction of elastic constants from SAW measurements

With the model to calculate SAW velocities at specified directions, the grain orientation information from EBSD, the PDMS orientation information from optical microscopy, density data from Figure 21, and composition information from EDS, either the forward simulation or neural network method could be applied to extract the elastic constants.

For forward simulations, the process is similar to that for polycrystalline Ni. To extract

the elastic constants of a specific composition, e.g. Fe-80Ni, the experimental SAW

velocities on the five different PDMS orientations, as indicated by the red double-

arrowed line in Figure 23 were used for the optimization. The same simplex-based

optimization method was applied using different initial values to find the best match to

the experimental SAW velocities. Elastic constants of other compositions were similarly

obtained and are summarized in Table 12 and Figure 24.

Table 12. Comparison of the elastic constants of different Fe-Ni compositions obtained from the polycrystalline diffusion multiple sample of this study with those obtained from single crystals reported in the literature.

Compos-ition (Fe at. %)	C_{11} (GPa)			C_{12} (GPa)			C_{44} (GPa)		
	This study	Single-crystal data	Differ-ence (%)	This study	Single-crystal data	Differ-ence (%)	This study	Single-crystal data	Differ-ence (%)
10%	237.0	252	-6.0	123.8	143	-13.4	128.7	139	-7.4
20%	248.1	241	2.9	145.6	143	1.8	138.5	138	0.4
30%	238.7	233	2.4	155.2	146	6.3	129.3	127	1.8
40%	227.3	224	1.5	156.0	151	3.3	108.7	112	-2.9
50%	217.4	212	2.5	154.6	155	-0.3	81.1	90	-9.9
60%	170.6	157	8.7%	106.1	109	-2.7%	117.0	96	21.9%
70%	160.1	147	8.9%	86.6	89	-2.7%	138.2	113	22.3%
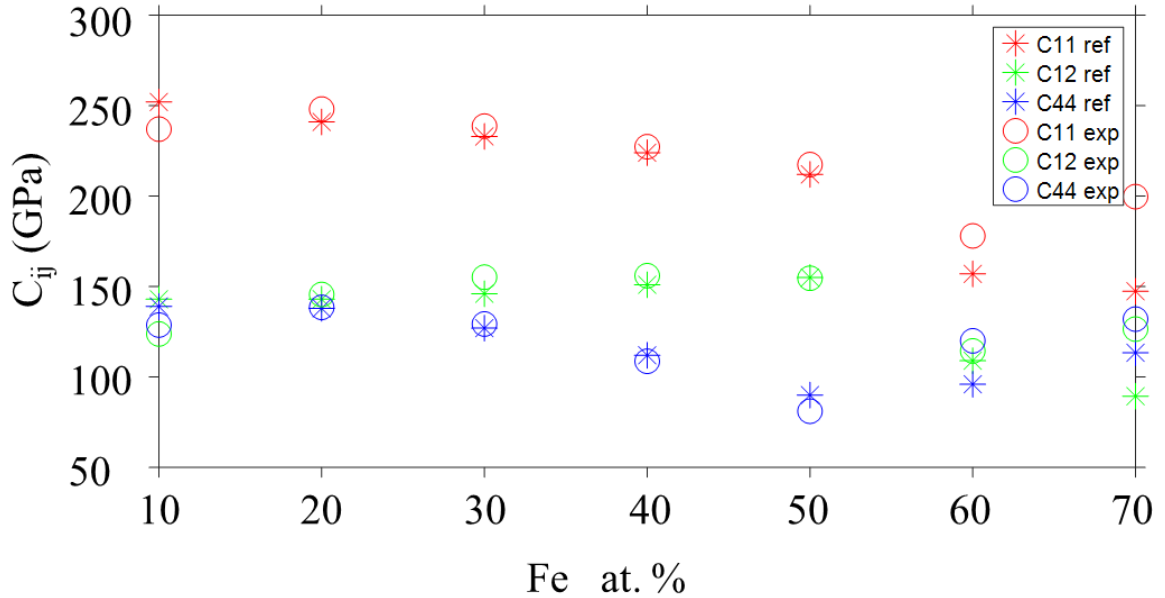
Figure 24. Elastic constants at different Fe-Ni compositions obtained from the current experiment on a diffusion multiple in comparison with the literature data from single crystals of different compositions[102,103].

Figure 24 summarizes data obtained from the current study obtained on a Fe-Ni diffusion in comparison with literature data from single crystals. The elastic constants at composition between Fe-50Ni and Fe-90Ni are in excellent agreement indicating the new high-throughput method works well.

However, for Fe-30Ni and Fe-40Ni, the deviations were much higher. This also made sense as they were extracted from less reliable scattered SAW velocity data as we explained before. Note that for some compositions, if not all five experimental measurements were reliable, only qualified data were used to extract the elastic constants. As the composition profile was measured at higher spatial resolution, elastic constants for

finer composition increment could also be obtained, which is much more efficient than those methods requiring using single crystals.

In addition to forward simulations, neural network method was also applied. SAW velocity is a function of elastic constants, grain orientation, PDMS orientation, material composition and density, as shown in Equation 5.1.1. There are only three independent elastic constants (C_{11}, C_{12}, C_{44}) in cubic materials.

$\mathbf{V_{SAW}}$ = SAW(C_{11}, C_{12}, C_{44}, Grain Orientation, PDMS Orientation, composition, density)   (5.1.1)

To extract the elastic constants of Fe-80Ni for example, we could get the grain orientation information is obtained from EBSD ([0.17   1.17   0.81] radian), composition information from EDS (Fe-80Ni) and 5 PDMS orientations information from microscope ([179, 84, 77, 70, 25] degree), thus the expression was simplified as in Equation 5.1.2:

$\mathbf{V_{SAW}}$ = SAW (C_{11}, C_{12}, C_{44}, [0.17   1.17   0.81], [179, 84, 77, 70, 25])   (5.1.2)

Note each PDMS orientation associates with one individual SAW velocity. Thus, five PDMS orientations lead to five SAW velocities. Bold font was used to emphasize the SAW velocity vector.

The elastic constants are the only variables to be determined, the other variables are parameters that are already known. Based on Equation 5.1.2, 6000 elastic constants-velocities pairs with other variables at fixed values were generated and put into the neural network for training. The training was performed using the MATLAB neural network toolbox. The box had a graphic friendly interface, which saved time and enhances efficiency. The neural network structure was displayed in Figure 25.
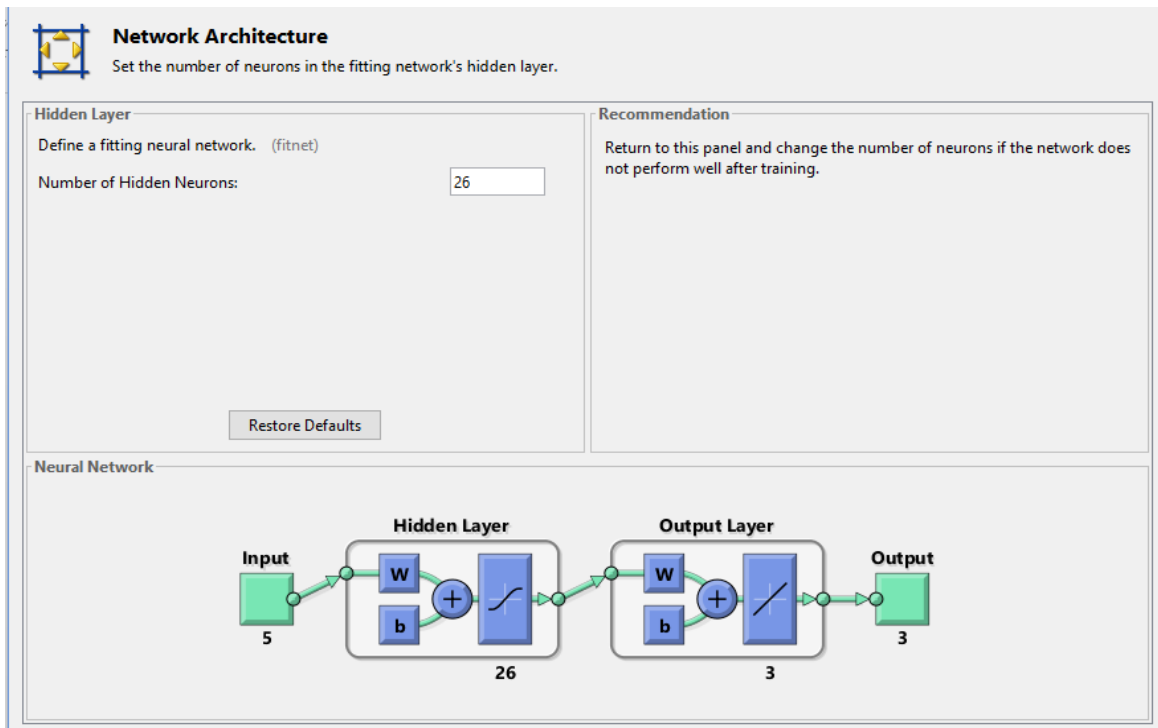
Figure 25. Neural network structure for extracting elastic constants at different Fe-Ni compositions.

The neural network had five inputs corresponding to the five SAW velocities with each representing a PDMS orientation ([179, 84, 77, 70, 25] degree). It had two layers, one

hidden layer and one output layer. The output layer had three outputs corresponding to C_{11}, C_{12} and C_{44}. The hidden layer took charge of exploring the relation between the inputs and outputs. There were 26 neurons in the hidden layer. The number of neurons was determined by the network.

Figure 26 shows how well the network performed in exploring the relation between the inputs (SAW velocities) and outputs (elastic constants C_{11}, C_{12} and C_{44}). To train the network, the original data was divided into 3 sets: training set, validation set and testing set. 70% of original data went to the training set to train the network; 15% of original data went to the validation set to validate the network; 15% of original data went to the testing set to test the network. The performance of the network was reflected in each of the R values. The closer to one those R values were, the better the trained network could capture the characteristics between inputs and outputs.

Results	Samples	MSE	R
Training:	4200	1528.69018e-0	9.81089e-1
Validation:	900	1664.43415e-0	9.80013e-1
Testing:	900	2823.19016e-0	9.65297e-1

Figure 26. The performance of the neural network in extracting the relation between elastic constants and SAW velocities at given density, composition and orientations.

The objective was to adjust the number of neurons in the hidden layer to make all three R values as closer to one as possible. If the R value of training set is very high but that of testing set is low, it indicates too many neurons to fit the relation, i.e. overfitting, thus the number of neurons needs to be decreased in the hidden layer. If the R values are generally low, it indicates some of the characteristics between the inputs and outputs are missing in the network, the number of neurons need to be increased in the hidden layer to increase the degree of freedom and fitting accuracy. By several attempts, 26 neurons were found to perform to the best.

The extracted elastic constants for several compositions were listed in Table 13. The trend in each component of elastic constants is consistent with the forward simulations. The extraction of elastic constants of other compositions are still in process.

Table 13. Extracted elastic constants for the Fe-Ni diffusion couple at compositions of Fe-80Ni (Ni-20Fe) and Fe-90Ni (Ni-10Fe) through the neural network method.

Compos- ition (Fe at. %)	C_{11} (GPa)			C_{12} (GPa)			C_{44} (GPa)		
	This study	Single- crystal data	Differ- ence (%)	This study	Single- crystal data	Differ- ence (%)	This study	Single- crystal data	Differ- ence (%)
10%	244	252	-3.2	144	143	0.7	130	139	-6.5
20%	253	241	5.0	148	143	3.5	137	138	-0.7

In summary, application of a SAW-PDMS-TDTR-MODEL method on a diffusion multiple is capable of measuring composition-dependent full elastic constants without

making any single crystals. The elastic constants at different compositions of Fe-Ni alloys have been extracted using either a forward simulation method or a neural network machine learning method. The C_{ij} values of compositions between Fe-50Ni and Fe-90Ni obtained from current study are in excellent agreement with single-crystal data from the literature, leading credibility to the new method.

5.2 Extraction of the elastic constants from powder samples

Many solid compounds and materials are hard to synthesize into bulk samples, not even polycrystalline bulk solids. But most of them can be synthesized into powders. Thus, it is highly desirable to be able to measure full elastic constants from large grained powders. For a conceptual demonstration, Sn powders are used since they are easily available and very cost-effective. In addition, β-Sn is tetragonal and has six independent C_{ij} values to be measured, which is reasonably challenging.

5.2.1   Sample preparations and characterizations

The Sn powder (99.9% purity) was purchased from AEE (Atlantic Equipment Engineers). It has a mesh size of ~100, roughly 150 μm in powder size, as seen in Figure 27.

Figure 27. Powder Sn of 99.9% purity with mesh size ~ 100 purchased from Atlantic Equipment Engineers.

Some Cu-based conductive bakelite powders were crushed with mortar and pestle to similar size of the Sn powders. Then, they were mixed uniformly with a ratio of bakelite to powder 3:1 and poured into the container of the hot mount machine. Normal uncrushed bakelite was also poured in to fill up the holder space. Regular bakelite hot mounting was performed and the Sn powders inside the mount were subject to grinding on 800 and 1200 grit size of SiC sandpaper and then polished on a vibrotary machine with 0.05 μm silica

suspension as the polishing fluid until a mirror-like surface was obtained, as shown in Figure 28.

The reason to crush a portion of the bakelite powders to mix with Sn powder was to increase the amount of the Sn powders that could stay on the surface. Otherwise, the much bigger bakelite powders would occupy a large portion of surface and the amount of the Sn powders would be very low.
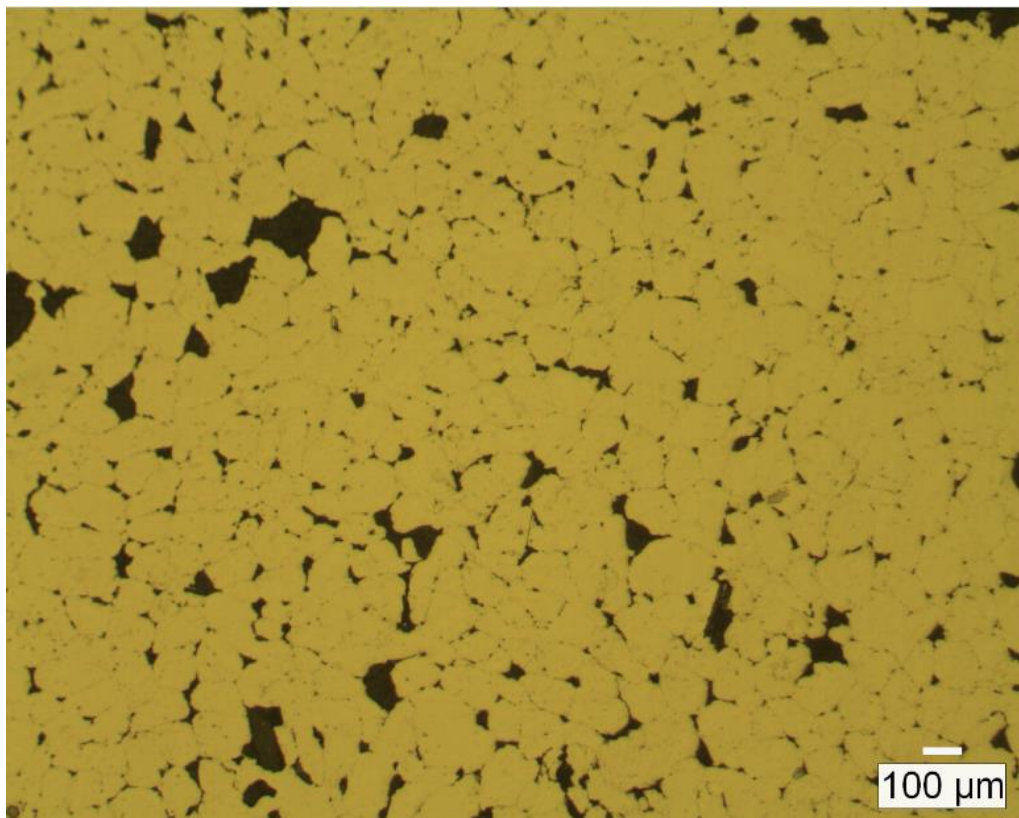
Figure 28. Optical image showing the surface of Sn after mounding, grinding and polishing. Individual powders can still be seen.

A region was selected on the polished surface and micro-indents were placed as markers on the surface, as seen under SEM in Figure 29(a). EBSD was conducted in the region and the inverse pole figure is shown in Figure 29(b). Except a few big grains, the grain size (not particle size) was generally small, which posed a challenge on SAW accuracy. The laser spot size was 3.6 μm in radius, the affected-area of generated SAW is comparative to the single grain size. Thus, the grain boundary could affect the wave propagation and thus affect our measurement of SAW velocities. To solve this issue, multiple spots in a single grain along a single direction were measured for SAW velocities, the average consistent SAW velocity was selected to represent the SAW velocity for a particular orientation.
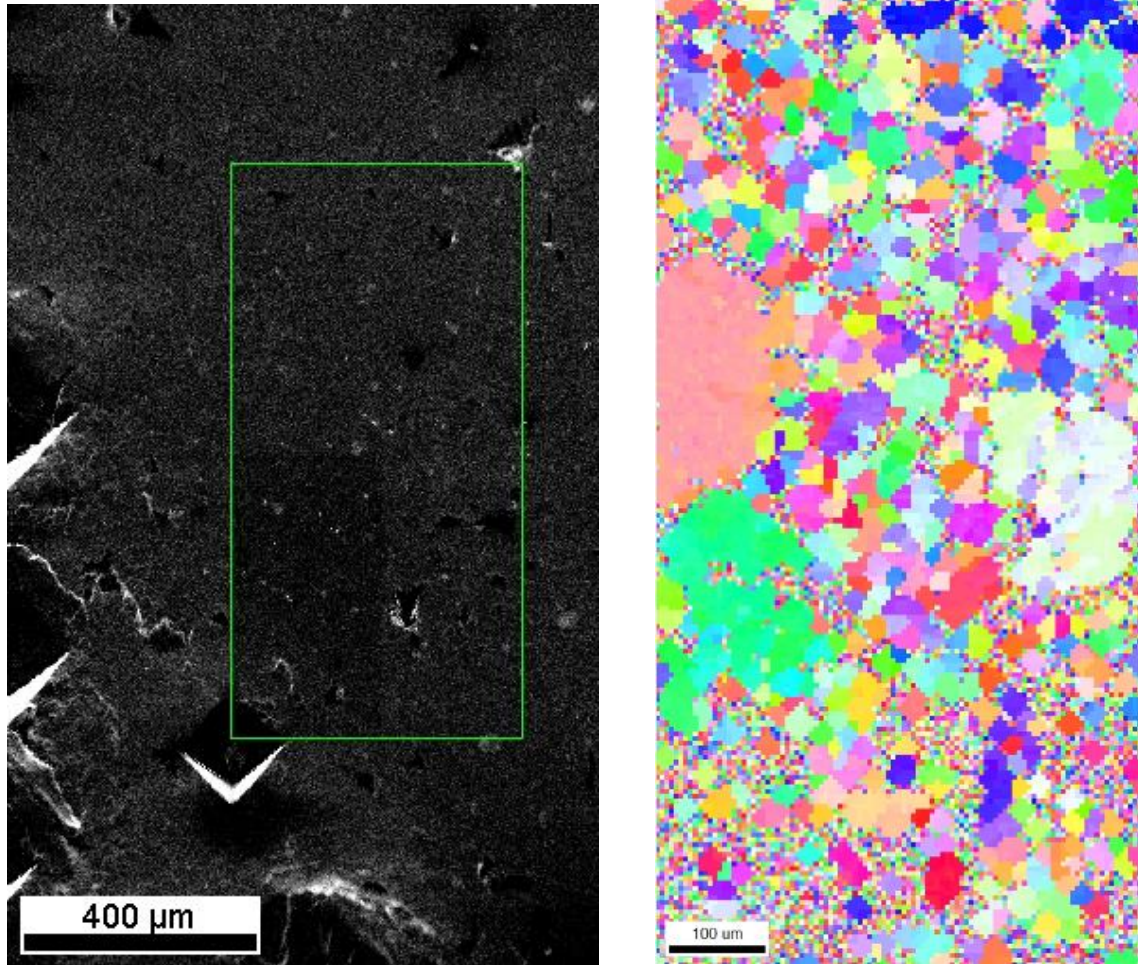
Figure 29. (a) SEM image and (b) the EBSD inverse pole figure of the indented region of the Sn powder sample.

5.2.2   SAW measurements of powder Sn

The SAW velocities of 20 grains along the same PDMS orientation were listed in Table 14. The modeled velocities by using reference elastic constants of Sn were also included

in Table 14 for comparison. The experimental SAW velocities were generally very close

to calculated values except a few orientations.

Table 14. SAW measurements of Sn powders. Theoretical SAW velocities computed using reference elastic constants and experimental SAW velocities are both listed for comparison. PDMS orientation is 48.5 degree referred to the transverse direction.

Grain	Location (x,y) (μm)	Euler angles (radian)			V_{model} (m/s)	V_{expt} (m/s)	Difference (%)
G1	(155,455)	2.5626	1.9213	1.4655	1027.5	1043.8	1.6
G2	(350,650)	0.4073	2.1900	3.8573	1348.0	1349.7	0.1
G3	(100,450)	4.1812	0.7183	4.3835	1009.7	1077.8	6.7
G4	(350,250)	2.3607	1.8207	2.0829	1183.7	1184.6	0.1
G5	(350,350)	2.2670	2.1129	4.0086	1336.9	1262.3	-5.6
G6	(345,750)	4.6602	0.6196	1.8163	1490.2	1466.2	-1.6
G7	(455,395)	2.6012	0.9669	5.0557	1250.7	1281.7	2.5
G8	(350,550)	3.7370	1.1981	6.1205	1607.9	1592.5	-1.0
G9	(145,550)	4.4976	1.0966	5.1125	1390.0	1417.7	2.0
G10	(250,405)	2.5103	1.8784	5.9788	1586.0	1655.6	4.4
G11	(250,495)	0.1089	1.6339	6.0752	1599.3	1543.9	-3.5
G12	(200,455)	2.0756	2.0189	3.9317	1322.4	1344.9	1.7
G13	(305,595)	0.9627	0.6718	2.0028	1395.3	1364.3	-2.2
G14	(400,845)	4.1469	1.6761	4.2949	1147.7	1131.2	-1.4
G15	(400,505)	1.7211	2.1357	1.9328	1384.8	1393.4	0.6
G16	(300,695)	3.4958	1.4140	5.1770	1148.1	1204.1	4.9
G17	(95,545)	1.0948	1.5583	2.9468	1614.0	1631.3	1.1
G18	(195,400)	2.8012	0.9135	5.2354	1478.1	1475.9	-0.1
G19	(450,400)	4.3008	1.6981	5.2117	1167.7	1281.7	9.8
G20	(55,100)	1.5370	1.8686	4.2093	1245.7	1272.0	2.1

5.2.3   Extraction of elastic constants of powder Sn

The reference elastic constants were selected as the initial value to extract the elastic constants through forward simulations. The extracted elastic constants are shown in Table 15 in comparison with single-crystal values.

Table 15. Comparison between reference elastic constants and extracted elastic constants from our method of Sn.

C_{ij} (GPa)	This study	Single-crystal data	Difference (%)
C_{11}	76.3	72.4	5.4
C_{12}	61.4	58.5	5.0
C_{13}	51.1	37.4	36.6
C_{33}	96.1	88.3	8.8
C_{44}	22.9	22.0	4.1
C_{66}	24.2	24.4	-0.8

The extracted elastic constants are with 6% from single-crystal elastic constants except for C_{13} and C_{33}. More experiments and analysis are needed to obtain better measurements of these two elastic constants. The C_{13} and C_{33} extracted from another polycrystalline bulk Sn sample are 39.5 GPa and 84.2 GPa, respectively, which only deviates from the single-crystal data by 5.6% and -4.6%, respectively. The bulk Sn elastic constants were obtained from 33 orientations in contrast to the powder sample measured along 20 orientations. This example shows that for low-symmetry crystals, more orientations need to be measured. In addition, the optimization /forward simulation algorithm has a hard time reaching global minimum. The algorithm needs significant improvement in the future.

5.3 Measurement of elastic constants of intermetallic compound Ni_3Sn_4 of monoclinic

crystalline symmetry

(This study is in collaboration with National Taiwan University. The first-principles

calculations were performed by Ms. Yaxian Wang in Prof. Wolfgang Windl's group at

Ohio State. The MCMC analysis was performed with the help of Prof. Steven

Niezgoda.).

Low symmetrical crystals such as monoclinic and triclinic phases require a large number

of independent elastic constants (C_{ij} values) to completely describe their elasticity. For

instance, a monoclinic crystal (compound) has 13 independent C_{ij} values which are hard

to measure even using single crystals. For this reason, among the approximately 23,000

monoclinic inorganic solid compounds listed in the CRYSTMET database[104], only a

handful of them have experimentally measured full-tensor C_{ij} values[105–108]. All of these

were laboriously measured using single crystals.

The monoclinic Ni_3Sn_4 phase was selected for this demonstration since its C_{ij} values have

never been measured, yet they are critical to understanding the performance of solder

joints in electronic devices where nickel is a commonly used under-bump-metallization

(UBM) material[109].

Nickel reacts with the Sn-based solder to form the Ni_3Sn_4 intermetallic compound (IMC). The presence of this Ni_3Sn_4 IMC between solders and conductor metals is a sign of good metallurgical bonding. However, because of the inherent brittle nature of Ni_3Sn_4, the reliability of solder joints becomes a concern. In traditional packaging technology, such as ball grid array (BGA)[110], this is not a big concern as Ni_3Sn_4 IMC only occupies a small portion of the joint. However, in three-dimensional integrated circuits (3D IC)[111–115], where the joint size can get down to about 5 to 10 microns, the Ni_3Sn_4 IMC can occupy a substantial portion of the joint and carry a significant part of the mechanical load of the joint. Thus, the mechanical properties of the Ni_3Sn_4 IMC become critical to the reliability of the micro joints.

Even though the plastic deformation behaviors of Ni_3Sn_4 have been studied[116,117], no experimental measurements have been reported for its C_{ij} values which are essential for accurate simulation of microstructural evolution and constitutive/micro-mechanical modeling. Ab initio method has been applied to calculate the C_{ij} values of Ni_3Sn_4[118,119] with significant discrepancy in the computed values. Nanoindentation has been applied to measure the Young's modulus of Ni_3Sn_4[120], but the full tensor C_{ij} values are still missing. Experimental measurement is highly desirable to obtain reliable full-tensor C_{ij} values.

The 13 independent full-tensor C_{ij} values would be extremely challenging to measure using the new method. This is mostly due to the challenges associated with the algorithm in reaching global minimum in the 13-variable space. The idea is to employ the elastic

constants computed from first-principles calculations as the initial input C_{ij}'s to the model in order to facilitate the search for the right C_{ij}'s by the algorithm. It is hoped that such a combination will lead to the correct C_{ij}'s from the measured SAW velocities.

5.3.1   Sample preparations and characterizations

The Ni_3Sn_4 phase was formed by reacting a pure Ni (99.99%) slugs with and Sn (99.99%) drops, with an atomic ratio Ni : Sn = 3 : 4, by melting in a sealed and evacuated quartz tube at 1000 °C for one week, followed by water quenching and then annealing at 750 °C for four weeks. The ingot was then sliced into small pieces and polished to reveal the microstructure for observation by optical microscopy with cross polarizers. The sample was grinded through 120, 500, 1200, 2400 grit size SiC sandpaper step by step and then polished with 1 μm diamond paste and then 0.025 μm SiO_2 suspension. A montage image is shown in Figure 30.
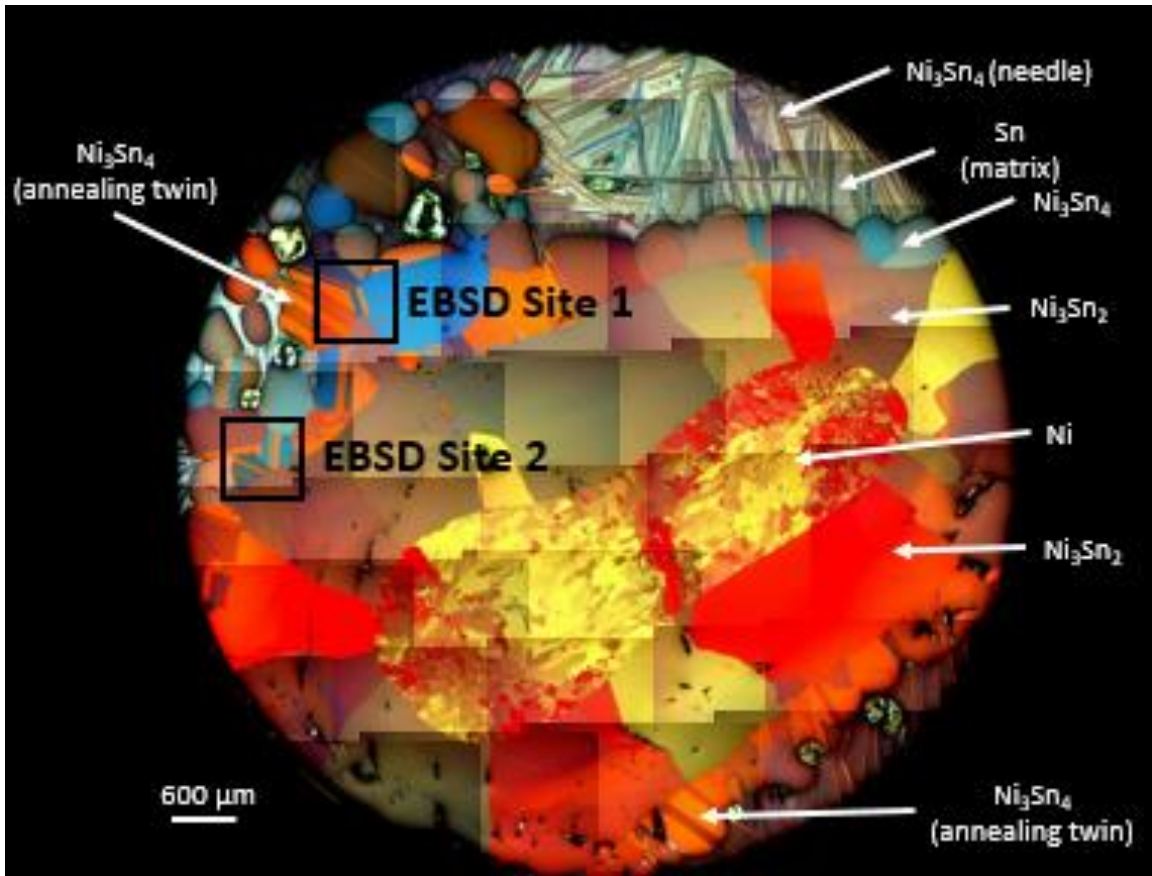
Figure 30. Polarized light microscopic images reflecting the microstructure of the Ni-Sn diffusion couple sample. This composite image is a montage consisting of several regional sections. Two sites were selected for EBSD and SAW experiments.

Given the anisotropic orientations and sizes of grains, two locations were selected for EBSD. The crystallographic orientations of each grain in the two EBSD sites were identified using a scanning electron microscope (JEOL JSM-7800F Prime) equipped with an EBSD detector, as shown in Figure 31(a) and Figure 31(c).

90
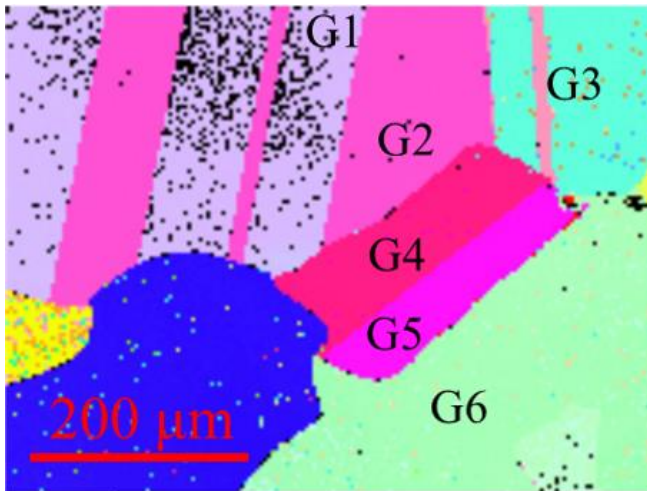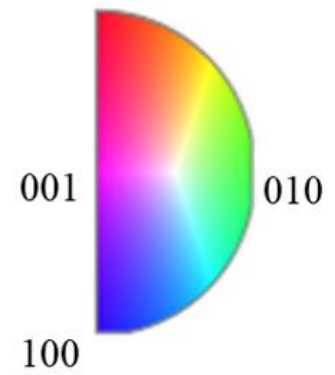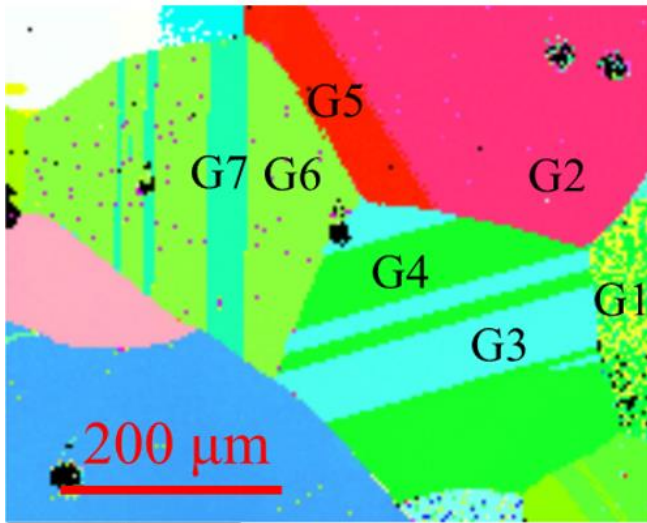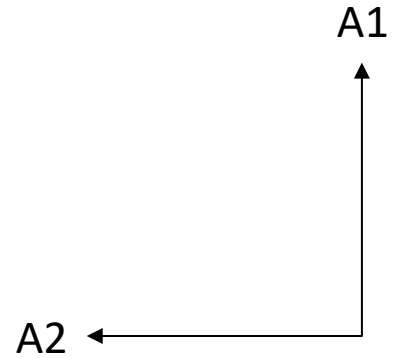
Figure 31. EBSD Inverse pole figures for (a) site 1 and for (c) site 2 of the polycrystalline Ni_3Sn_4 sample. Both the orientation map and sample coordinate frame are displayed in (b) and (d).

From the two EBSD inverse pole figures, several big grains were selected for the SAW experiments. To facilitate the location matching between EBSD and the SAW measurements, micro indents were put around those two sites. A coordinate system was also built to help determine locations in each grain. All grains in the two EBSD figures belonged to the Ni_3Sn_4 phase except for the ones located in the lower left corner of each figure, which was determined to be Ni_3Sn_2 phase. Our focus here was only on the grains of the Ni_3Sn_4 phase.

5.3.2   Elastic constants of Ni_3Sn_4 from first-principles calculations

The elastic constants of Ni_3Sn_4 has 13 independent components, which requires large number of initial values spanned in 13-dimensions. The forward simulation is not practical to run so many initial values in a reasonable amount of time to extract the full elastic constants. As a compromise, the first-principles calculations were employed to obtain a set of calculated elastic constants as the initial C_{ij} input to the SAW model. Then conventional forward simulation was used to update the elastic constants to minimize the difference between the computed SAW velocities and experimental SAW velocities until the optimized elastic constants were obtained.

First-principles calculations were performed using VASP (Vienna ab initio simulation package)[121], which implemented the DFT scheme within the plane wave projector augmented-wave (PAW) method[122] with generalized gradient approximation (GGA)

functional by Perdew et al[123]. After the convergence test, the following parameters are

employed a cutoff energy of 350 eV and a 14-atom cell with a 9*9*7 Monkhorst-Pack k-

point mesh for Brillouin zone integration to relax the cell to ground state[124] where the

deviation of β from experimental value was minimized. The experimental crystal

structure was used as an input for geometry optimization, where the energy of crystal was

minimized with respect to lattice constant and any interior degrees of freedom. Shown in

Table 16 were the results for predicted lattice constants.

Table 16. Lattice constants of Ni_3Sn_4 after relaxation by VASP at different settings.

Settings	a(Å)	b(Å)	c(Å)	β(deg)
Experimental values	12.214	4.060	5.219	105.00
14 atoms, 350 eV, 7*7*5	12.309	4.081	5.100	105.19
14 atoms, 350 eV, 9*9*7	12.308	4.096	5.081	105.09
14 atoms, 380 eV, 7*7*5	12.303	4.090	5.103	105.15
112 atoms, 350 eV, 7*7*5	12.309	4.091	5.085	105.04

The relaxed configuration was used to do the elastic property calculation. It used central

difference, which allowed each ion displaced in each direction by a small positive and

negative displacement. Then the Hessian matrix was determined, which was the matrix of

the second derivatives of energy with respect to the atomic positions. Thus, the elastic

constants 4th-rank tensor was calculated, shown in Table 17. Lee et al. and Gao et al.

reported the calculated elastic constant C_{ij} of Ni_3Sn_4 by using CASTEP software,

respectively [118,119]. Ghosh had compared calculated elastic constant of Fe_3C by VASP

and CASTEP[125], the deviation for C11~C66 was averaged to 144% while our

calculations end up with difference of 6.6% for Gao[110] and 17.4% for Lee[118]. We note

that nearly all values from Gao were smaller while those from Lee are larger.

Comparison between those calculated elastic constants and our forward simulation result

based on each calculated elastic constants as the initial values were all displayed in Table

17.

Table 17. Elastic constants of Ni_3Sn_4 calculated by different first-principles calculations and extracted from our experimental SAW measurements with first-principles calculation results as the initial values to run the forward simulation.

| C_{ij} | C_{ij} from pure calculation | | | C_{ij} from pure calculation plus SAW measurements | | |
	This work	Lee[118]	Gao[110]	This work	Lee	Gao
C11	191.3	192.2	155.0	272.2	198.2	174.3
C22	164.1	176.2	155.7	190.1	180.1	159.5
C33	178.1	204.6	180.1	226.6	211.4	197.0
C44	57.7	76.2	57.6	51.4	53.2	51.0
C55	64.6	77.0	59.9	53.2	61.3	59.2
C66	52.3	68.3	55.8	55.6	65.8	66.9
C12	67.4	77.4	70.2	17.4	74.7	56.8
C13	63.6	82.9	66.4	60.7	88.6	53.0
C23	85.3	80.3	71.8	115.8	105.8	81.4
C15	-24.3	-25.7	-21.1	-22.7	-25.8	-20.5
C25	13.0	12.7	9.9	3.5	3.9	2.5
C35	-3.5	-10.9	-8.6	-1.9	-8.5	-7.4
C46	3.5	8.2	9.9	2.1	8.7	9.7
Velocity difference	4.86% ± 3.99%	7.49% ± 5.24%	6.91% ± 4.71%	3.37% ± 2.84%	3.61% ± 3.11%	3.46% ± 2.90%

5.3.3 SAW measurement results and C_{ij} extraction

As monoclinic Ni_3Sn_4 has 13 independent C_{ij} values to be determined, multiple grains and PDMS film orientations were selected for each site for the SAW experiments, aimed at capturing enough anisotropic variations.

Six grains combined with five PDMS orientations were measured to obtain SAW velocities along 30 distinct directions for site 1, as shown in Figure 31(a). Similarly, seven grains combined with five PDMS orientations were selected for measuring SAW velocities along 35 distinct directions for site 2, as shown in Figure 31(b). As a result, measurements of SAW velocities along 65 crystalline directions were made. For each combination of the grain orientation and PDMS orientation, four velocity measurements around the center of the grain location were made. The spatial sampling range of the measurements were within a circle of 5 μm in radius from the center of the grain. The average velocities after removing significantly dissimilar ones were used as the experimental velocity of each crystallographic direction. With reliable experimental SAW velocities and initial values obtained from different first-principles calculations, the extraction of elastic constants of Ni_3Sn_4 were done through forward simulations. The comparison of elastic constants from pure calculations and from modeling the experimental SAW velocities using first-principles data as initial model input were all listed in Table 17.
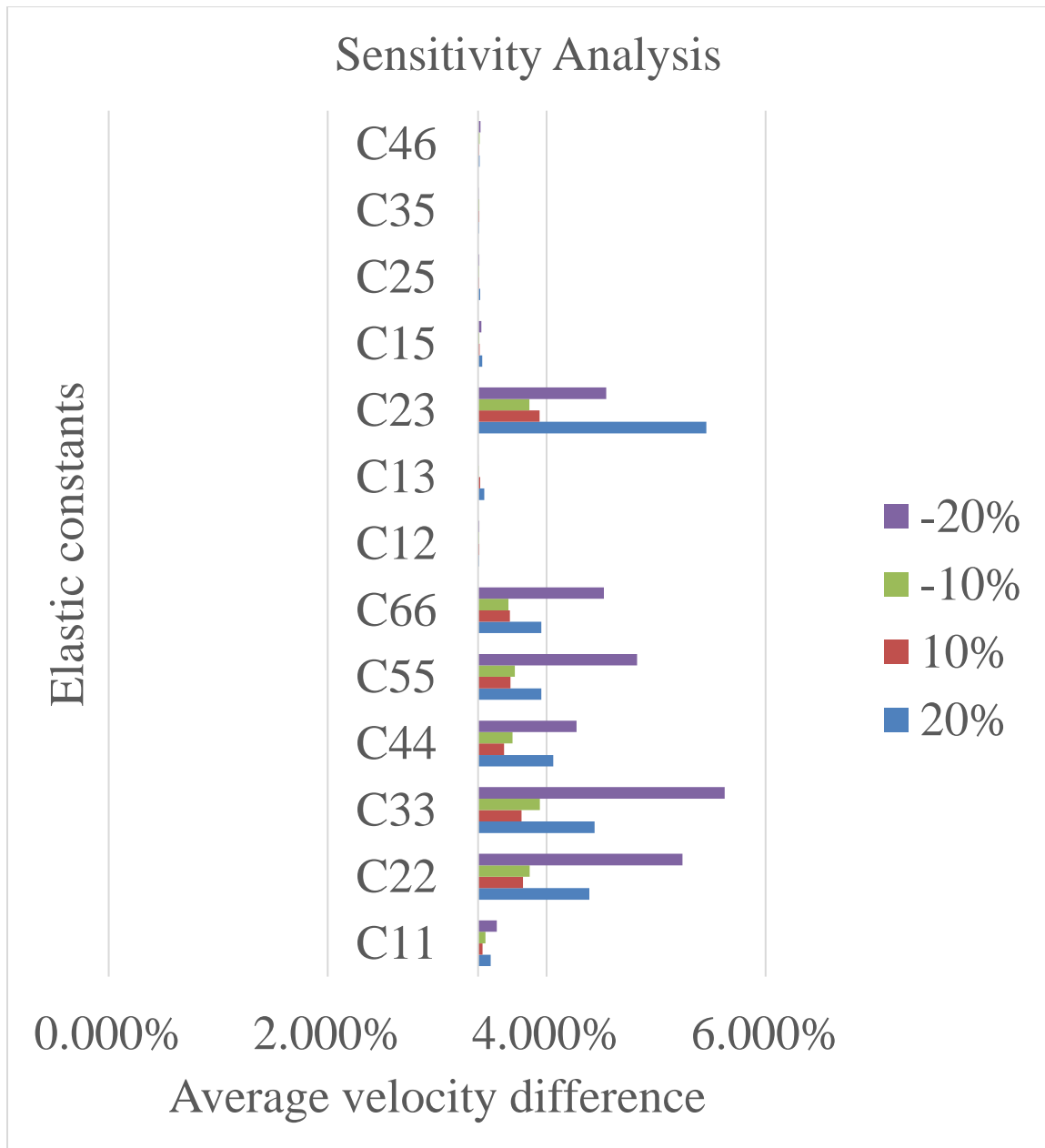
Figure 32. Sensitivity analysis of each elastic constants extracted by combining SAW experiments and first-principles calculations from (a) this study, (b) Lee's work and (c) Gao's work on average SAW velocity difference.
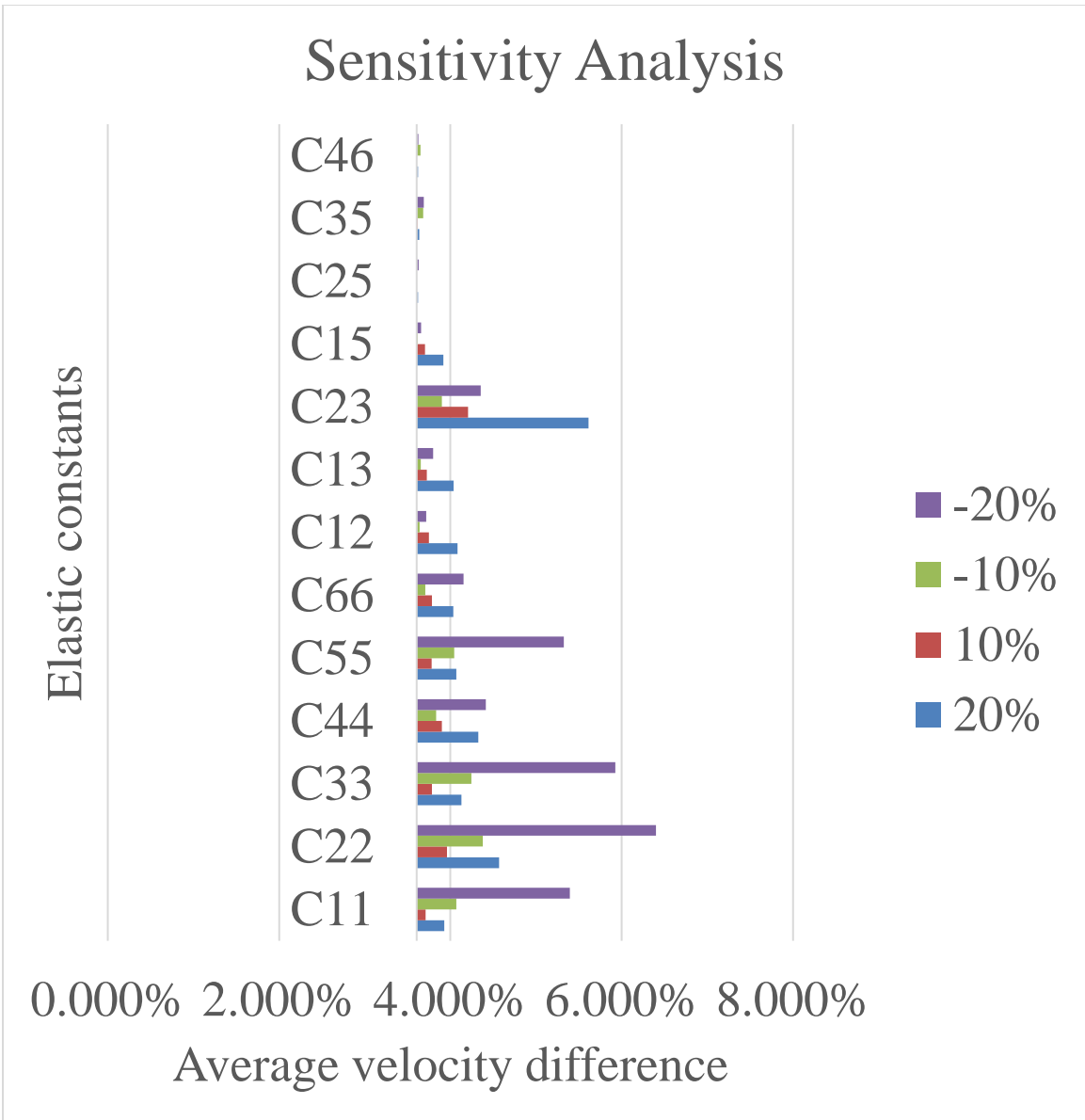
(b)

Sensitivity Analysis
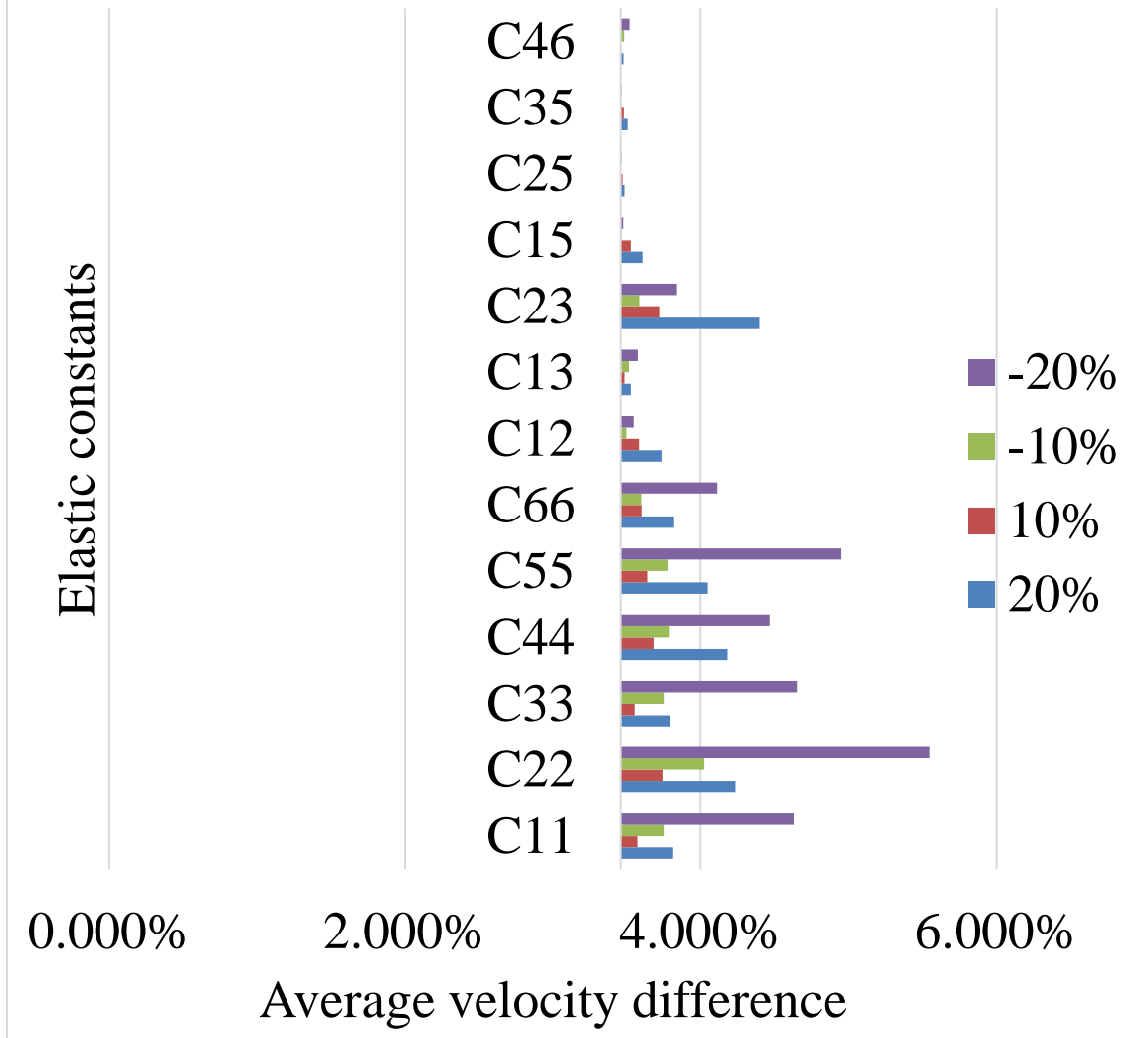
(c)

The general trend in each elastic constant component is consistent to each other but some deviation between each set of extracted elastic constants using different initial values is still quite large. Sensitivity analysis was performed for each set of extracted elastic constants, as shown in Figure 32.

The sensitivity analysis shows that the SAW velocities are more sensitive to elastic constant components of C_{11}, C_{22}, C_{33}, C_{44}, C_{55}, C_{66} and C_{23} regardless of which set of extracted elastic constants. The relative small sensitivity in C_{11} in Figure 32(a) can explain the big deviation in the C_{11} value among all three sets. Moreover, the extracted elastic constants are not convergent to the same values. This is attributed to the local optimum trap in the forward simulations. Some trap-skip methods like MCMC (Monte Carlo Markov Chain) is going to be applied to find the global optimum.

It is very likely that the SAW-PDMS-TDTR-MODEL method, even with first-principles input, cannot measure all the 13 independent C_{ij} values due to the fact that: (1) the SAW velocities are insensitive to some C_{ij} values; and (2) the current forward-simulation algorithm is incapable of finding the global minimum in the 13-variable space even with the first-principles data as the initial input. More work needs to be performed in the future to overcome these challenges.

5.4 Full elastic constants of Ni-based superalloy René 88DT

(This section is mostly based on the paper: Xinpeng Du and Ji-Cheng Zhao. First measurement of the full elastic constants of superalloy René 88DT. *Scripta Materialia* 152, 24 (2018).)

René 88DT is one of the powder metallurgy superalloys[126,127]; and it is one of the most widely used ones for jet engine high pressure turbine discs. Its composition is Ni-16Cr-13Co-4Nb-4W-2.1Al-3.7Ti-0.7Nb-0.03C-0.015B (wt.%, Ni-balance). René 88DT has an excellent combination of tensile and creep strength as well as corrosion and oxidation resistance at elevated temperatures[128]. Various studies have been performed over the years on its phase structures[129] and the effect of constituent elements[130], creep deformation mechanisms at elevated temperatures[131,132], and fatigue crack initiation mechanisms under cyclic loading[133–135].

The elastic behavior of René 88DT is much less studied and the full elastic constants of René 88DT have never been reported yet, most likely due to the fact it is a significant undertaking to grow a single crystal out of such a complex powder metallurgy composition for elastic constant measurement. Nevertheless, extensive studies on the fatigue initiation mechanism of René 88DT show that elastic anisotropy plays a significant role on the crack initiation process[133–135]. Moreover, elastic constants are essential parameters for various micro-mechanics models, such as fatigue sensitivity[136],

failure mechanism at microscale[137], crack nucleation mechanisms[138], fatigue-crack-initiation interaction[139] and so on. Thus, accurate elastic constant values of René 88DT will significantly help improve the accuracy of these models

Traditional tensile stress-strain measurement has been used to evaluate the Young's modulus of René 88DT[140]. The DIC (Digital Image Correlation) technique afforded measurement of local strains of polycrystals in both elastic and plastic regimes to help measure Young's modulus more accurately[141–143]. Hardness test has been used to measure the mechanical strength of Nickel-based superalloys[144]. These methods, however, can only result in an average measurement of Young's modulus rather than the full elastic constants.

By using our TDTR-based SAW technique, however, the full elastic constants can be extracted accurately. As mentioned in Chapter 2, by combining both experiments generating and detecting SAW velocities along various orientations, and models predicting SAW velocities along any specified orientation, the full elastic constants can be eventually extracted through the forward simulations.

5.4.1   Sample preparations and characterizations

A bulk piece of René 88DT was provided by GE Global Research and a small piece of the sample was cut with a diamond saw and then placed in an air furnace for heat

treatment at 1150 °C for 50 h. The oxidation resistance of René 88DT is so good that a

protective oxide scale was formed to protect the sample from internal oxidation. The

center of the sample was unaffected by any of the oxidation effect. As 1150 °C was

higher than the solvus line (roughly 1105 °C) of the gamma prime phase, no gamma

prime precipitate would expect to form at 1150 °C. This heat treatment served the dual

purpose of both growing the grain size and forming the fcc solid solution phase to reduce

the potential interference of the gamma prime phase during the measurements. After the

heat treatment, the sample was directly taken out of the furnace and cooled down to

ambient temperature. It was mounted in regular metallographic bakelite, grinded with

SiC sand papers of 120, 320, 600, 800, 1200 grit sizes in sequence in water, and polished

with a vibratory polishing machine in 0.05 um colloidal silica suspension for 48 h to

obtain a high-quality surface finish.

Microhardness indents were placed on the sample surface to denote a region (1000 µm x

500 µm) of interest. Electron backscattering diffraction (EBSD) characterization was

carried out on a XL-30 ESEM system (FEI, Inc.) with a high-brightness field-emission

electron gun. The acceleration voltage was 20 kV. The working distance was 20 mm. The

step size was 5 µm for each direction. The collected data was then analyzed on a TSL

software platform. The collected inverse pole figure of (001) showing in Figure 33

displays the distribution of the grain size and orientation.
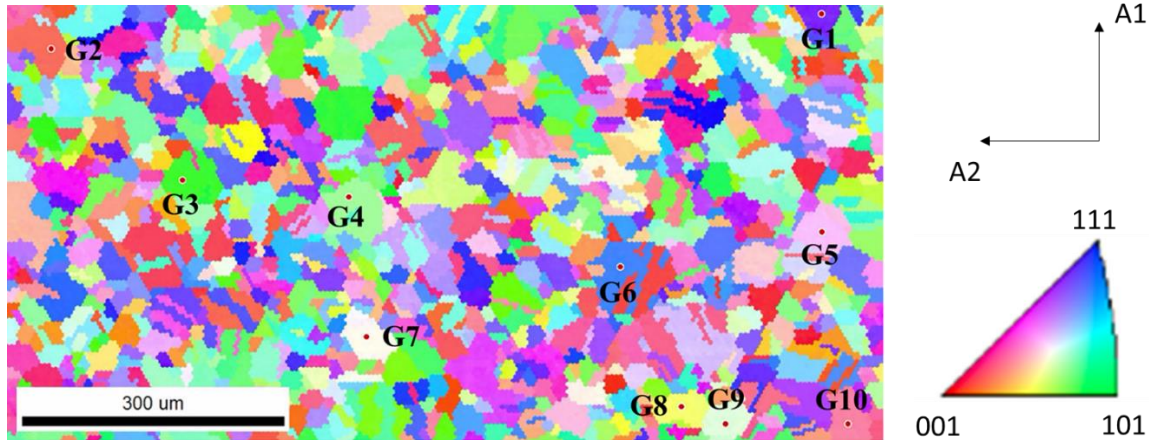
Figure 33. EBSD inverse pole figure of (001) with the reference frame and orientation map shown. The scanning region was 1000 μm x 500 μm with a step size of 5 μm in both directions. Based on the grain size and distribution, 10 grains were selected and labeled for SAW measurements.

5.4.2   Experimental measurements of surface acoustic waves

SAW measurements were conducted on ten grains as labelled in Figure 33 under two different PDMS orientations. In other words, we performed one set of measurements and then rotated the PDMS film orientation and performed a second set of measurements. For each grain, four points around the grain center were measured to get SAW velocities. The results of one SAW measurement on Grain 10 under PDMS orientation 1 are shown in Figure 34 to demonstrate the data in both time domain and frequency domain to explain how the SAW velocity was evaluated. The velocities reported in Table 18 are the average velocity of four measurements on each grain under each orientation. The laser spot size of this experiment was ~5 µm, enabling high spatial resolution of the measurements since the SAW attenuates quickly beyond the laser spot by the PDMS film.

103

(a)

SAW peak
3.94 GHz
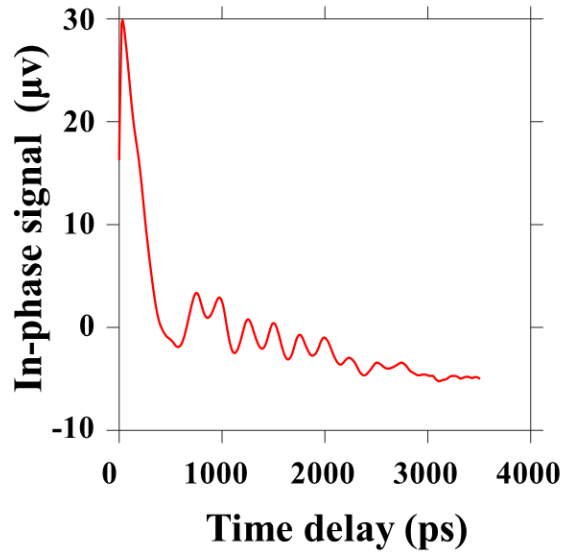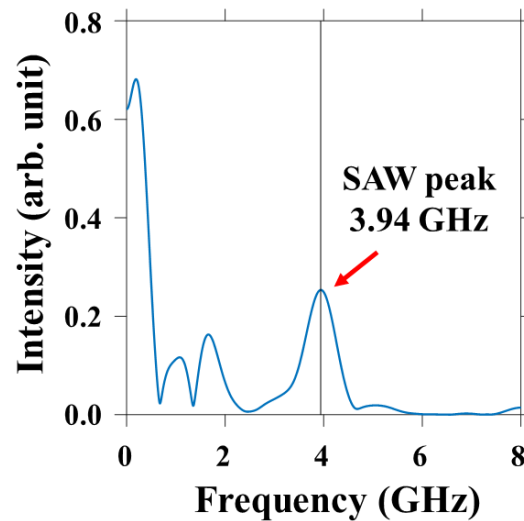
(b)

Figure 34. (a) Time domain signal of a SAW wave obtained by detecting the SAW profile as a function of the delay time between the pump and the probe beam; (b) Frequency domain signal of the SAW wave obtained by applying the Fourier transform to the time domain signal. The SAW peak could be identified in the frequency domain, and the SAW velocity is equal to the frequency times the wavelength which is 700 nm that is dictated by the PDMS film grating.

To obtain the direction associated with the measured velocity, Euler angles measured using EBSD and the PDMS film orientation measured by light microscope were both employed. Some measurements were not included in the analysis due to either small signal-to-noise ratios or wide variability of the velocities within a grain. The results of the reliable measurements were summarized in Table 18 with a total of 15 experimental SAW velocities, which spanned a range of ~ 2500 m/s to ~2870 m/s, indicating high anisotropy of René 88DT. Those experimental velocities were to be matched by the computed SAW velocities from the elastodynamic model with elastic constants and density as input parameters. Our forward optimization method was based on Nelder-Mead simplex method. At any given initial value of elastic constants, the method would begin to update the elastic constants iteratively, aimed at minimizing the difference between calculated SAW velocities and experimental SAW velocities. As it only converges to a local optimum, multiple initial values were provided to achieve the best fit possible.

Table 18. Comparison of the experimental ($V_{expt.}$) and computed (V_{model}) SAW velocities.

Grain	Euler angles (degree)	PDMS orientation (degree)	$V_{expt.}$ (m/s)	V_{model} (m/s)	Difference (%)
G5	[95.1, 76.2, 26.8]	89.6	2495.5	2451.0	-1.78
G6	[348.7, 64.4, 43.0]	89.6	2473.7	2606.1	5.35
G7	[34.8, 79.2, 241.0]	89.6	2496.7	2588.8	3.69
G8	[225.1, 93.0, 154.8]	89.6	2869.3	2867.7	-0.06
G9	[209.0, 32.8, 160.6]	89.6	2507.7	2509.0	0.05
G10	[136.9, 19.9, 297.6]	89.6	2756.5	2690.2	-2.41
G1	[215.4, 118.5, 145.6]	60.1	2648.5	2690.2	1.57
G2	[203.0, 86.3, 169.5]	60.1	2638.8	2501.8	-5.19
G3	[13.6, 88.5, 47.0]	60.1	2575.6	2581.1	0.21
G4	[26.8, 35.6, 102.4]	60.1	2517.4	2649.5	5.25
G5	[95.1, 76.2, 26.8]	60.1	2619.3	2617.8	-0.06
G7	[34.8, 79.2, 241.0]	60.1	2573.2	2569.8	-0.13
G8	[225.1, 93.0, 154.8]	60.1	2756.5	2552.9	-7.39
G9	[209.0, 32.8, 160.6]	60.1	2625.0	2482.3	-5.44
G10	[136.9, 19.9, 297.6]	60.1	2718.8	2571.6	-5.41

5.4.3   Extraction of elastic constants of René 88DT

A total of 45 initial values were equally sampled for C_{11}, C_{12} and C_{44} and put into the

forward optimization algorithm. The best fit yields the elastic constants as $C_{11} = 267.1$

GPa, $C_{12} = 170.5$ GPa, and $C_{44} = 107.6$ GPa. The anisotropic ratio is 2.23, which is quite

high. The computed and measured SAW velocities are in excellent agreement as shown

in Table 18. The density of René 88DT used in the computation is 8.36 g/cm^3 [145]. Since

there are no literature elastic constants for a direct comparison with our results, the elastic

constants are used to compute the aggregate polycrystalline properties such as Young's

modulus and Poisson's ratio for comparison. The computed/aggregated Young's modulus from our elastic constants is between 194 and 221 GPa (the lower and upper bonds) using the widely employed Voigt and Reuss averaging schemes [146], which agrees well with the literature Young's modulus values ranging from 210 to 220 GPa that were obtained from bulk sample measurements[130][147]. The aggregated Poisson's ratio computed from our elastic constants is between 0.32 and 0.34.

The current measurement was made at ambient temperature. The PDMS film may still be workable for temperatures up to 200 °C above which a different grating film or an alternative grating scheme need to be identified or developed. To prevent sample surface oxidation at higher temperatures (e.g., > 400 °C), the sample needs to be put inside a vacuum with an optical window to allow laser beam access. Such measurements at the working temperatures of the alloy are highly desired and will be pursued in the future. In summary, this SAW-PDMS-TDTR-MODEL method was successfully applied to measure the full elastic constants of René 88DT from a polycrystalline sample. SAW velocities along 15 distinct directions were experimentally measured and were fitted with a robust elastodynamic model through a forward optimization algorithm. The full elastic constants of René 88DT were obtained and reported for the first time as $C_{11} = 267.1$ GPa, $C_{12} = 170.5$ GPa, and $C_{44} = 107.6$ GPa. This new method can be employed to measure elastic constants of any polycrystalline sample with a grain size larger than 30 µm as demonstrated in this study, thus it will greatly facilitate future measurements of elastic constants for complex alloys without the need of growing single crystals.

5.5 Extraction of Young's modulus of inorganic glasses

In contrast to crystalline materials, glass materials have no long-range order in atomic arrangement, which makes them unique in many properties for various applications. Though improvement of glass composition, microstructure and fabrication process could help reduce brittleness of glass materials[148], glasses still dominantly deform in the elastic region. The macroscopically plasticity is very limited at room temperature[149]. Thus, the modulus of elasticity is very essential to characterize a glass.

Stress-strain test is conventionally used to measure Young's modulus of glasses based on either compression/tension test[150–152] or nano-indentation[153,154]. However, as the measurement results are not only dependent on the materials' intrinsic properties but also dependent on external parameters like indenter shape[155], strain rate[156], and even sample size[157], test results are not consistent from time to time or from instrument to instrument.

Atomic Force Acoustic Microscopy (AFAM) has been used to measure local elastic properties like Young's modulus of materials[158,159]. But as this technique depends not only on the Young's modulus of the sample and the tip, but also on the tip shape, exerted load and surface geometry, its accuracy depends on the various corrections. Ultrasonic techniques have also been developed to measure modulus[160–162], but as the sample needs to be machined in a certain geometry and size; and some form of contact transducer or coupling agent is also needed. The stringent requirements limit its applicability.

The elastodynamic model described in Chapter 2 can be slightly modified to relate

Young's modulus to materials density, Poisson's ratio and SAW velocities. Thus, the

SAW-PDMS-TDTR-MODEL method can be applied to measure Young's modulus of

glasses when their densities and Poisson's ratios are known. As our model only gives a

numerical solution, the approximated analytic solution of the SAW velocity as a function

of the Young's modulus, Poisson's ratio and the materials density derived by Viktorov[163]

was used here, as shown in Equation 5.5.1.

$$V_{SAW} = \frac{0.87 + 1.12v}{1+v} \sqrt{\frac{E}{2\rho(1+v)}} \qquad (5.5.1)$$

where, V_{SAW} is the SAW velocity, E the Young's modulus, v Poisson's ratio and ρ

material density. From this solution, the Young's modulus can be obtained by measuring

SAW velocity and Poisson's ratio separately.

5.5.1   Sample preparations

Three different isotropic materials, crystalline tungsten (which is intrinsically isotropic in

modulus), a soda lime glass and a Zr-based metallic glass were prepared. The tungsten

metal was purchased from Kamis, Inc. It was grinded with SiC paper from 320, 400, 600,

800, 1200 grit size in sequence and polished in a vibratory polishing machine with 0.05

colloidal silica suspension for 24 hours. This tungsten sample was mainly used as a

reference for measurements of other inorganic glass samples. The soda lime glass slides

($76.2 \times 25.4 \times 1.0$ mm) were purchased from Fisher Scientific (Item number: 12-544-1).

To increase the efficiency of laser power in inducing thermal gradient for launching

surface acoustic waves in the soda lime glass, an aluminum coating of less than 20 nm

was deposited on the sample as a transducer using a vacuum magnetron sputter (Denton

Vacuum LLC). The Zr-based metallic glass was obtained from Materion (Vit 1b:

$Zr_{67}Cu_{10.6}Ni_{9.8}Ti_{8.8}Be_{3.8}$ wt%). The same vibratory polishing process as we did for the

tungsten sample was done on this metallic glass.

5.5.2   Experimental measurements of SAW velocities

The laser setup is the same except that a half-wave plate working at the laser wavelength

(780 nm) was inserted in the experimental setup to help match the laser pump light

polarization with the orientation of the 1D grating PDMS film on the sample, and thus

increased the signal-to-noise ratio in SAW measurement.

Four locations and five orientations of each sample were selected for SAW

measurements. The representative experimental signals are shown in Figure 35. The

acquisition of signal was in the time domain. After applying the Fourier transform to get

signals expressed in the frequency domain, SAW frequency peaks were identified to

calculate SAW velocities, which is equal to the peak frequency times the wavelength of

the SAW wave (700 nm in this case). The velocities were measured to be 2667.6 ± 23.8

m/s, 3131.5 ± 24.1 m/s and 2226.1 ± 17.8 m/s for tungsten metal, soda lime glass and

metallic glass, respectively.
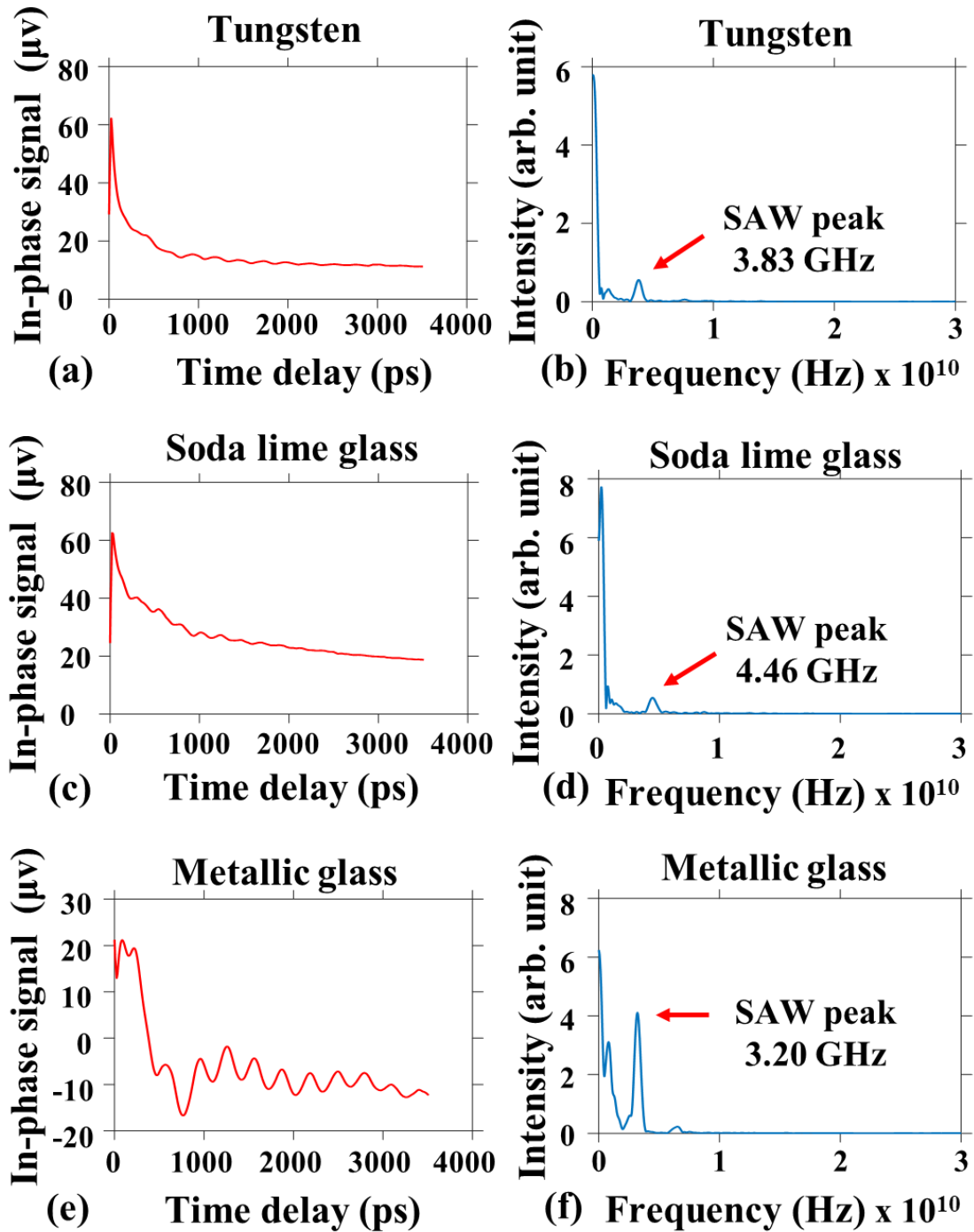
Figure 35. Time domain signal for (a) tungsten, (c) soda lime glass, and (e) metallic glass, and their corresponding Fourier transform in the frequency-domain for (b) tungsten, (d) soda lime glass, and (f) metallic glass. The SAW peaks identified in the frequency domain determine the experimental SAW velocities.

111

The single-crystal elastic constants and density data for tungsten reported by Lowrie et al.[164] were used to predict the Young's modulus of 407.4 GPa; Reference data of the soda lime glass was obtained from Fisher Scientific. The density, Poisson's ratio and Young's modulus for the soda lime glass is 2480 kg/m^3, 0.2 and 72 GPa, respectively; Reference data sheet from Materion showed the density and the Young's modulus of the metallic glass was 6000 kg/m^3 and 95 GPa, respectively. The Poisson's ratio was estimated to be 0.353.

By subjecting the measured SAW velocities, and individual densities and Poisson's ratios to Equation 5.5.1, the measured Young's modulus of each sample as well as the reference Young's modulus are all shown in Table 19. The differences of our extracted Young's modulus from reference values are 1.1%, 3.9% and 2.7%, respectively, indicating the reliability and accuracy of our method in measuring Young's modulus for inorganic glass materials.

Table 19. Comparison of the Young's modulus reported in the literature values and extracted from the current SAW measurements.

Materials	Young's modulus from the literature (GPa)	Young's modulus from current measurements (GPa)
Tungsten	407.4	411.7 ± 7.3
Soda lime glass	72	69.2 ± 1.1
Zr-based metallic glass	95	92.4 ± 1.5

In conclusion, this SAW method can be used to measure Young's modulus of inorganic glasses when the density and Poisson's ratio can be obtained separately. Less than 4% differences of Young's modulus from SAW measurements with other independent measurements have been achieved on tungsten, soda lime glass and Zr-based metallic glass. This method has high spatial resolution (~ 10 µm) and thus is amendable to measurements of individual phases in a polished surface of a sample.

Chapter 6: Conclusions

In this dissertation, an innovative laser-ultrasonic method has been developed to measure single-crystal elastic constants from polycrystalline samples. This technique is based upon measurements of the SAW velocities with the help of a polydimethylsiloxane film grating that is placed on a polished surface of a polycrystalline sample to confine surface acoustic waves that are induced by a femtosecond laser and measured using pump-probe time-domain thermoreflectance (TDTR). Electron backscatter diffraction (EBSD) is employed to measure the crystallographic orientation along which the surface acoustic wave propagates in each grain (perpendicular to the polydimethylsiloxane grating). Such measurements are performed on several grains. A robust mathematical solution was developed to compute SAW velocities along any crystallographic orientation of any crystal structure with given elastic constants and density. By either inputting various starting values of elastic constants to compute the SAW velocities to match experimental measurements in several distinct crystallographic orientations using an optimization algorithm or applying the neural network machine learning method to train a network on generated data to explore the relation among elastic constants, density and orientations and directly extract elastic constants from experimental measurements, accurate elastic

constant values have been obtained from seven polycrystalline metal samples of Ni, Al,

Ta, Nb, Fe (bcc) Co (hcp) and β-Sn (tetragonal) to be within 6.8% of single-crystal

measurements.

In addition to the benchmark work on the polycrystalline pure metals, the new SAW-

PDMS-TDTR-MODEL method has been applied to the measurements of: (1) composition-

dependent elastic constants of Fe-Ni diffusion couple; (2) elastic constants from powder

Sn sample; (3) the elastic constants of intermetallic compound Ni_3Sn_4 of monoclinic

crystalline symmetry; (4) the full elastic constants of Ni-based superalloy René 88DT; and

(5) Young's modulus of inorganic glass materials, showing the advantages of this method

with high accuracy, high spatial resolution and high throughput, saving a significant time

and cost by avoiding the preparation of single crystals.

This new technique is expected to change the current scenario that experimentally

measured elastic constants are available for only about 1% of the estimated 160,000

distinct solid compounds, not to mention the significant need for elastic constants of

various solid solution compositions that are the base of structural materials.

Appendix A: The Model for Surface Acoustic Waves

(This SAW model is mostly following the paper by Zhao et al[59]. but with improved treatment of eigen value degeneracy.)

On the assumption of linear elastic deformation in a homogeneous anisotropic medium and the absence of body force, body torque, dissipative process and external fields, the wave motion equation is expressed as

$$C_{ijkl} \frac{\partial^2 U_l}{\partial x_j\, \partial x_k} = \rho \frac{\partial^2 U_i}{\partial t^2} \qquad x_3 \leq 0 \qquad\qquad (A.1)$$

where U stands for the displacement, ρ the mass density and C the elastic constants. x and t are the space and time, respectively. Here the Einstein summation convention is implied.

The boundary condition is assumed to be a point source hitting on the sample surface at a specific time, which corresponds to the boundary condition (A.2)

$$\sigma_{i3}|_{z=0} = C_{i3kl} \frac{\partial U_l}{\partial x_k}\Big|_{z=0} = \delta_{i3}\delta(x,y)\delta(t) \qquad\qquad (A.2)$$

Wherein, $\delta_{i3} = \{ \begin{smallmatrix} 1 & i = 3 \\ 0 & i \neq 3 \end{smallmatrix}$, $\delta(x,y) = \delta(x)\delta(y)$.

$$i, j, k, l = 1,2,3$$

In addition, at very far away, the displacement should be zero. When the time goes to infinity, the displacement should also be zero. So, we have another set boundary conditions (A.3).

$$U_i(x, y, z, t) = 0, \qquad \text{when } x, y, z, t \to \infty \tag{A.3}$$

The corresponding initial condition is determined by the causality principle, which dictates before any trigger takes place, the displacement should be zero.

$$U_i(x, y, z, t) = 0 \text{ for } t < 0 \tag{A.4}$$

To solve Equation (A.1), Fourier transform is applied to the time t and the space variables x and y that are parallel to the sample surface.

$$\tilde{U}(k_x, k_y, z, \omega) = \int\limits_{-\infty}^{\infty}\!\!\!\int\!\!\!\int U(x, y, z, t) e^{i\omega t - ik_x x - ik_y y} dx dy dt \tag{A.5}$$

Substitute Equation A.5 into Equation A.1, the differential equation is converted into a simple second order differential equation with z and its derivatives as the variables.

$$
\begin{aligned}
-k_x^2 C_{i11l}\tilde{U}_l &- k_x k_y C_{i12l}\tilde{U}_l + ik_x C_{i13l}\frac{\partial \tilde{U}_l}{\partial z} - C_{iuvl}k_u k_v \tilde{U}_l - k_x k_y C_{i21l}\tilde{U}_l \\
&- k_y^2 C_{i22l}\tilde{U}_l + ik_y C_{i23l}\frac{\partial \tilde{U}_l}{\partial z} + ik_x C_{i31l}\frac{\partial \tilde{U}_l}{\partial z} \\
&+ ik_y C_{i32l}\frac{\partial \tilde{U}_l}{\partial z} + C_{i33l}\frac{\partial^2 \tilde{U}_l}{\partial z^2} + ik_u C_{i3ul}\frac{\partial \tilde{U}_l}{\partial z} = -\rho\omega^2 \delta_{il}\tilde{U}_l
\end{aligned}
\tag{A.6}
$$

In a compact form, it is expressed as,

$$-k_x k_y C_{iuvl}\overline{U}_l + ik_v C_{iv3l}\frac{\partial \overline{U}_l}{\partial z} + ik_u C_{i3ul}\frac{\partial \overline{U}_l}{\partial z} + C_{i33l}\frac{\partial^2 \overline{U}_l}{\partial z^2} = -\rho\omega^2 \delta_{il}\overline{U}_l \tag{A.7}$$

Wherein, u,v = 1,2. Here, the Einstein summation is applied.

117

As this is a homogeneous differential equation, the solution format is assumed to be

$$\tilde{U}_l(k_x, k_y, z, \omega) = A_l(k_x, k_y, \omega)e^{-pz} \tag{A.8}$$

Where the A_l stands for the displacement vector.

By substituting this assumption of Equation A.8 into Equation A.7, the differential equation is converted into an algebra one.

$$D_{il}A_l = 0 \tag{A.9}$$

Wherein, $D_{il} = C_{i33l}p^2 - ik_u C_{i3ul}p - ik_v C_{iv3l}p - C_{iuvl}k_u k_v + p\omega^2 \delta_{il}$

This actually becomes an eigen-value problem. To assure the displacement vector has a non-trivial solution, the determinant must be zero.

$$\det(D) = 0 \tag{A.10}$$

This results in a polynomial equation of sixth order with respect to p.

If a small imaginary part is induced, say, into the frequency, it is guaranteed that there are three and only three roots of p that have positive real parts or pure imaginary. However, it's possible for p to have multiple roots, which means p can have degeneracy. (For example, when p has three roots, p1, p2 and p3. If two of them are equal, we say it has multiple roots, or say p has a degeneracy). When this occurs, two distinct eigen-vectors that are perpendicular to each other corresponding to the same eigen value need to be found. The previous modeling[59] doesn't take that into consideration and uses SVD (singular-value decomposition) method, which will return the same eigen-vector once the eigen-value is the same rather than a pair of two eigen-vectors that are perpendicular to each other.

118

Therefore, a better way to solve this issue is to go to the null space of D, which is not a full rank matrix. The built-in *eig* function in MATLAB is employed to solve this issue.

After right eigen values of p and corresponding eigen-vectors are selected, the displacement can be expressed as the superposition of the three modes. But the weight of each mode is still unknown as expressed in Equation A.11.

$$\overline{U}_l(k_x, k_y, z, \omega) = \sum_r a_r A_l^r(k_x, k_y, \omega)e^{-p_r z} \tag{A.11}$$

To evaluate the coefficients of a_r of each mode, the boundary condition (A.2) is applied. After doing Fourier transform on Equation A.2,

$$\overline{\delta}_{i3}|_{z=0} = \delta_{i3} = (ik_u C_{i3ul} - p_r C_{i33l})A_l^r \cdot a_r \tag{A.12}$$

Exhibit the expression in a simple fashion

$$M_{ir} \cdot a_r = \delta_{i3}, \qquad \text{where } M_{ir} = (ik_u C_{i3ul} - p_r C_{i33l})A_l^r \tag{A.13}$$

As the eigen values of p and their corresponding eigen vectors are all known, the M_{ir} is defined, thus the coefficients a_r are deterministic right away through linear algebra principle.

The above solution is only on how to solve the displacement response by Fourier transform. To obtain SAW velocities, the solution is to remain in the Fourier transformed space. Spatial x is transformed to k while time t is transformed to ω. k/ω is defined to be

slowness. It is more effective to remain in the slowness space and evaluate the variation of displacement directly to get the SAW velocity.

The solution mentioned above corresponds to a point source stimulus, so intrinsically this solution is a Green's function. The stimulus source in our measurement, however, is a circular laser spot with Gaussian distribution of intensity. To obtain the complete solution, it is necessary to convolute the real heating source profile with this Green's function. We assume the heating laser spot is expressed in (A.14).

$$S(x, y) = Ae^{-\frac{x^2+y^2}{a^2}} \tag{A.14}$$

Wherein, a is the radius of the spot. Then the convolution of the displacement with (A.14) is the real solution in the time-space domain. The multiplicity of (A.11) and Fourier transformed (A.14) is the real solution in the slowness space.

Appendix B: The Model for Bulk Acoustic Waves

(This bulk acoustic wave model is mostly following the book by Rosenbaum[38].)

The bulk wave differs from the SAWs in that the third space component (the space variable normal to the sample surface) can also be sampled, which however, is a parameter to be determined in the surface wave modeling.

The governing equation for bulk wave modeling is exactly the same as the surface wave modeling regardless of the infinity in the third dimension. In this case, there is no boundary condition confining the wave.

$$C_{ijkl} \frac{\partial^2 U_l}{\partial x_j \, \partial x_k} = \rho \frac{\partial^2 U_i}{\partial t^2} \tag{B.1}$$

Assume the solution of displacement has such a form

$$U_i = A e^{-i\left(k_x x + k_y y + k_z z - \omega t\right)} \tag{B.2}$$

where A stands for amplitude, k the wave vector. The rest of variables are defined exactly as in SAW modeling.

Substitute Equation B.2 into Equation B.1, a homogeneous equation is obtained

$$\left(C_{ijkl}k_j k_k - \rho\omega^2\delta_{il}\right)U_l = 0 \tag{B.3}$$

Introduction of direction cosine of the propagation and the relation between phase velocity and time and space frequencies yields

$$\left(C_{ijkl}l_j l_k - \rho v^2\delta_{il}\right)U_l = 0 \tag{B.4}$$

Wherein, l stands for the propagation direction cosine and v the phase bulk wave velocity. To guarantee this equation has non-trivial solution of displacement, the determinant of the matrix must vanish

$$\det|C_{ijkl}l_j l_k - \rho v^2\delta_{il}| = 0 \tag{B.5}$$

By solving this equation, a bi-cubic equation with respect to v is obtained, and the three positive v solutions are the corresponding velocities of the three bulk waves.

All the eigenvalues of v are substituted into Equation B.4 to solve the displacement. By comparing the polarization (displacement) vector with the propagation direction, corresponding velocity modes can be mapped out accordingly.

In addition, our modeling also takes into account the piezoelectric effect. This effect is considered by modifying the expression of the elastic constants.

$$C' = C^E + \frac{e^2}{\epsilon^2} \tag{B.6}$$

Wherein, C' is the modified elastic constants, also called stiffened elastic constants; C^E is the normal elastic constants; e is the piezoelectric stress matrix; ϵ is the piezoelectric matrix. To express them in terms of index notation

$$C'_{KL} = C^E_{KL} + \frac{(e_{Kj}l_j)(l_i e_{iL})}{l_i \epsilon_{ij} l_j} \ , K, L = 1,2,3,4,5,6; \quad i, j = 1,2,3 \qquad (B.7)$$

More detailed derivation of this relation can be found else where[38].

Appendix C: The Determination of SAW Propagation Direction in Measurements

As mentioned before, experimental measurements are referred to the sample coordinate system through the transverse direction (TD), rolling direction (RD) and normal direction (ND) while modeling calculations are referred to the crystalline principle coordinate system (reference direction for SAW velocity is [010]), the conversion of the coordinates between these two coordinate systems needs to be established.

In addition, the reference direction in the sample coordinate system was chosen to be TD, but the actual direction was determined by the PDMS film. The grating vector (the direction perpendicular to the grating lines) determined the actual direction of SAW propagation. Typically, the PDMS film is not perfectly aligned along the TD direction, there was always some deviation from the reference direction that needs to be corrected. Moreover, in some cases, PDMS was rotated on purpose by different angles to increase the number of film orientations for distinct anisotropic SAW velocities. Thus, the deviation angle between PDMS grating vector and reference TD direction needs to be accurately measured to get SAW measurements right. As a result, the connection between the experimental coordinate

system and the coordinate system associated with PDMS grating vector needs to be established.

For any two Cartesian coordinate systems, any direction indicated by a normalized 3-digit vector in one coordinate system can be expressed in the other coordinate system through the transformation matrix as constructed as follows:
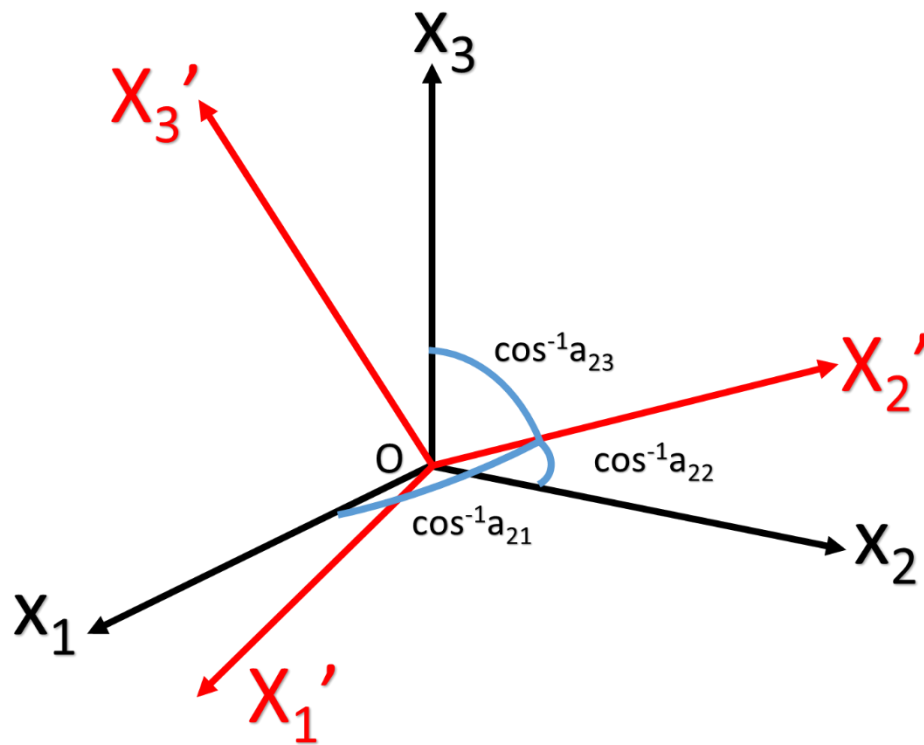
Figure C.1. The old and new Cartesian coordinate systems and how each component of the transformation matrix is constructed.

In Figure C.1, x_1, x_2, x_3 are assumed to represent the three axes of the old Cartesian coordinate system while x_1', x_2', x_3' represent the three axes of the new Cartesian coordinate system. Then the transformation matrix can be constructed as

$$A = \begin{bmatrix} a_{11} & a_{12} & a_{13} \\ a_{21} & a_{22} & a_{23} \\ a_{31} & a_{32} & a_{33} \end{bmatrix} \tag{C.1}$$

Where a_{ij} stands for the cosine of the angle between the new i axis and old j axis.

Euler Angles (α, β, γ, Bunge's convention) stand for three consecutive rotations, starting from the rotation about z axis by α, followed by the rotation about new x axis by β and then followed by the rotation about the newest z axis by γ. Based on Equation C.1, the corresponding transformation matrix of the three consecutive rotations is expressed as follows:

$$T_1 = \begin{bmatrix} \cos\gamma & \sin\gamma & 0 \\ -\sin\gamma & \cos\gamma & 0 \\ 0 & 0 & 1 \end{bmatrix} \begin{bmatrix} 1 & 0 & 0 \\ 0 & \cos\beta & \sin\beta \\ 0 & -\sin\beta & \cos\beta \end{bmatrix} \begin{bmatrix} \cos\alpha & \sin\alpha & 0 \\ -\sin\alpha & \cos\alpha & 0 \\ 0 & 0 & 1 \end{bmatrix} \tag{C.2}$$

In terms of the PDMS film orientation, a new coordinate system was established. Figure C.2 shows the general relation between the sample coordinate system and PDMS-based coordinate system. Here A1 and A2 stand for RD and TD directions in the sample coordinate system. The ND direction points out of paper. They formed the sample coordinate system. OP stands for the PDMS film grating line direction while OS stands for the direction of SAW propagation. OP and OS are perpendicular to each other. With a

126

virtue axis pointing out of paper, the PDMS orientation-based coordinate system was established. (Here a right-hand Cartesian coordinate system was guaranteed). Thus, the transformation matrix M connecting the PDMS coordinate system and sample coordinate system could be established, which rotated OP to A1 and OS to A2. The rotation angle (not the deviation angle) was defined to be the angle between OP and the direction antiparallel to A2. This provides the convenience when measuring the angle under a microscope. With the angle known, the transformation matrix was constructed as in Equation C.3.
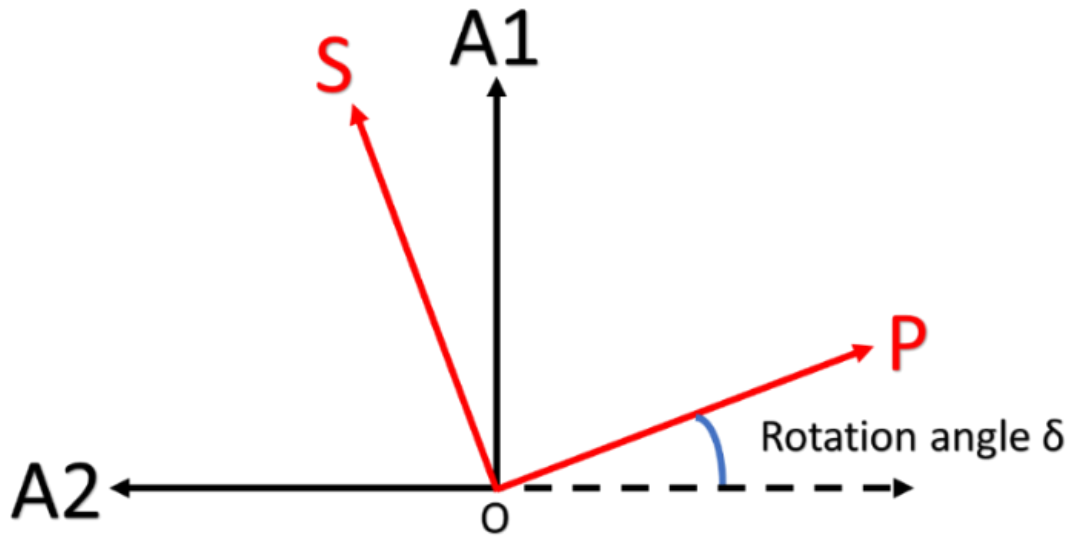
Figure C.2. Two coordinate systems correlating the PDMS film vector orientation with the EBSD orientation.

$$T_2 = \begin{bmatrix} \cos(90 - \delta) & \cos(\delta) & 0 \\ \cos(180 - \delta) & \cos(90 - \delta) & 0 \\ 0 & 0 & 1 \end{bmatrix} \tag{C.3}$$

As a result, the actual SAW propagation direction OS was rotated to align with the TD direction in sample coordinate system, which was then transformed by rotations represented by Euler Angles to align with the [010] direction in the crystalline principle coordinate system. The complete coordinate transformation was in Equation C.4.

$$T = \begin{bmatrix} \cos\gamma & \sin\gamma & 0 \\ -\sin\gamma & \cos\gamma & 0 \\ 0 & 0 & 1 \end{bmatrix} \begin{bmatrix} 1 & 0 & 0 \\ 0 & \cos\beta & \sin\beta \\ 0 & -\sin\beta & \cos\beta \end{bmatrix} \begin{bmatrix} \cos\alpha & \sin\alpha & 0 \\ -\sin\alpha & \cos\alpha & 0 \\ 0 & 0 & 1 \end{bmatrix} \begin{bmatrix} \cos(90-\delta) & \cos(\delta) & 0 \\ \cos(180-\delta) & \cos(90-\delta) & 0 \\ 0 & 0 & 1 \end{bmatrix} \quad (C.4)$$

Also, in order to express [010] in terms of the PDMS coordinate system, we can apply the transpose of the transformation matrix to [010], namely

$$C = T' \begin{bmatrix} 0 \\ 1 \\ 0 \end{bmatrix}$$

Appendix D: MATLAB coding used in this dissertation

1. Forward simulation

```
clear
clc
tic
ub=[800,300,300]'*1e9;%This is the upper bound for C11 C44 C12 for most
metals and ceramics
lb=[4,2,2]'*1e9;         %This is the lower bound for C11 C44 C12 for most
metals and ceramics
Num=[8,3,3];            %Attempt numbers of C11 C44 C12

%Sampling the C11 C44 C12 values for initials values
for i=1:3;
Cset{i}=linspace(lb(i),ub(i),Num(i)+2);
Cset{i}(1)=[];
Cset{i}(end)=[];
end

% Find the terminal output with errors and iterations. Error minimum is
the target
for i=1:Num(1);   % C11
    for j=1:Num(2);   %C44
        for k=1:Num(3);   %C12
            i
            j
            k
    % Temp1 Temp2 and Temp3 are the initial C11 C44 C12
values,respectively
            Temp1=Cset{1}(i);
            Temp2=Cset{2}(j);
            Temp3=Cset{3}(k);
            [Temp1,Temp2,Temp3]
            [x,fval,exitflag,output] =
fminsearchbnd(@Ni_fitting_three_value_3_11_16,[Temp1 Temp2
Temp3],lb,ub); %*****

            % fminsearchbnd returns the information between measured
velocities and theoretically set velocities in the subroutine
            C{i,j,k}=x;
```

```matlab
            err(i,j,k)=fval;
            iter(i,j,k)=output.iterations;
        end
    end
end
save('Ni_forward_simulation_XX_XX_XXXX')

%Sort the differences among each local optimum
[errmin, minind] = min(err(:));
[i, j, k] = ind2sub(size(err),minind);
fprintf('The smallest error is %d\n',err(i,j,k))
fprintf('The corresponding Cij is C11:%.3dGPa C44:%.3dGPa
C12:%.3dGPa\n',C{i,j,k}/1e9)

%Display the differences and associated C values from smallest to
largest
disp('Display the entire Cij values and corresponding differences:')
disp('         C11            C44            C12            err');
errSort=sort(err(:));
for i=1:length(err(:));
     Cindex=find(err==errSort(i));
    [a,b,c]=ind2sub(size(err),Cindex);
    format shortg
    disp([C{a,b,c}/1e9,err(a,b,c),2*C{a,b,c}(2)/(C{a,b,c}(1)-
C{a,b,c}(3))]);
end
toc
```

130

```
function [x,fval,exitflag,output] =
fminsearchbnd(fun,x0,LB,UB,options,varargin)
% FMINSEARCHBND: FMINSEARCH, but with bound constraints by
transformation
% usage: x=FMINSEARCHBND(fun,x0)
% usage: x=FMINSEARCHBND(fun,x0,LB)
% usage: x=FMINSEARCHBND(fun,x0,LB,UB)
% usage: x=FMINSEARCHBND(fun,x0,LB,UB,options)
% usage: x=FMINSEARCHBND(fun,x0,LB,UB,options,p1,p2,...)
% usage: [x,fval,exitflag,output]=FMINSEARCHBND(fun,x0,...)
%
% arguments:
%  fun, x0, options - see the help for FMINSEARCH
%
%  LB - lower bound vector or array, must be the same size as x0
%
%        If no lower bounds exist for one of the variables, then
%        supply -inf for that variable.
%
%        If no lower bounds at all, then LB may be left empty.
%
%        Variables may be fixed in value by setting the corresponding
%        lower and upper bounds to exactly the same value.
%
%  UB - upper bound vector or array, must be the same size as x0
%
%        If no upper bounds exist for one of the variables, then
%        supply +inf for that variable.
%
%        If no upper bounds at all, then UB may be left empty.
%
%        Variables may be fixed in value by setting the corresponding
%        lower and upper bounds to exactly the same value.
%
% Notes:
%
%  If options is supplied, then TolX will apply to the transformed
%  variables. All other FMINSEARCH parameters should be unaffected.
%
%  Variables which are constrained by both a lower and an upper
%  bound will use a sin transformation. Those constrained by
%  only a lower or an upper bound will use a quadratic
%  transformation, and unconstrained variables will be left alone.
%
%  Variables may be fixed by setting their respective bounds equal.
%  In this case, the problem will be reduced in size for FMINSEARCH.
%
%  The bounds are inclusive inequalities, which admit the
%  boundary values themselves, but will not permit ANY function
%  evaluations outside the bounds. These constraints are strictly
%  followed.
%
%  If your problem has an EXCLUSIVE (strict) constraint which will
%  not admit evaluation at the bound itself, then you must provide
```

```matlab
%  a slightly offset bound. An example of this is a function which
%  contains the log of one of its parameters. If you constrain the
%  variable to have a lower bound of zero, then FMINSEARCHBND may
%  try to evaluate the function exactly at zero.
%
%
% Example usage:
% rosen = @(x)  (1-x(1)).^2 + 105*(x(2)-x(1).^2).^2;
%
% fminsearch(rosen,[3 3])     % unconstrained
% ans =
%    1.0000    1.0000
%
% fminsearchbnd(rosen,[3 3],[2 2],[])     % constrained
% ans =
%    2.0000    4.0000
%
% See test_main.m for other examples of use.
%
%
% See also: fminsearch, fminspleas
%
%
% Author: John D'Errico
% E-mail: woodchips@rochester.rr.com
% Release: 4
% Release date: 7/23/06

% size checks
xsize = size(x0);
x0 = x0(:);
n=length(x0);

if (nargin<3) || isempty(LB)
  LB = repmat(-inf,n,1);
else
  LB = LB(:);
end
if (nargin<4) || isempty(UB)
  UB = repmat(inf,n,1);
else
  UB = UB(:);
end

if (n~=length(LB)) || (n~=length(UB))
  error 'x0 is incompatible in size with either LB or UB.'
end

% set default options if necessary
if (nargin<5) || isempty(options)
  options = optimset('fminsearch');
end
```

```matlab
% stuff into a struct to pass around
params.args = varargin;
params.LB = LB;
params.UB = UB;
params.fun = fun;
params.n = n;
% note that the number of parameters may actually vary if
% a user has chosen to fix one or more parameters
params.xsize = xsize;
params.OutputFcn = [];

% 0 --> unconstrained variable
% 1 --> lower bound only
% 2 --> upper bound only
% 3 --> dual finite bounds
% 4 --> fixed variable
params.BoundClass = zeros(n,1);
for i=1:n
  k = isfinite(LB(i)) + 2*isfinite(UB(i));
  params.BoundClass(i) = k;
  if (k==3) && (LB(i)==UB(i))
    params.BoundClass(i) = 4;
  end
end

% transform starting values into their unconstrained
% surrogates. Check for infeasible starting guesses.
x0u = x0;
k=1;
for i = 1:n
  switch params.BoundClass(i)
    case 1
      % lower bound only
      if x0(i)<=LB(i)
        % infeasible starting value. Use bound.
        x0u(k) = 0;
      else
        x0u(k) = sqrt(x0(i) - LB(i));
      end

      % increment k
      k=k+1;
    case 2
      % upper bound only
      if x0(i)>=UB(i)
        % infeasible starting value. use bound.
        x0u(k) = 0;
      else
        x0u(k) = sqrt(UB(i) - x0(i));
      end

      % increment k
      k=k+1;
```

133

```matlab
    case 3
      % lower and upper bounds
      if x0(i)<=LB(i)
        % infeasible starting value
        x0u(k) = -pi/2;
      elseif x0(i)>=UB(i)
        % infeasible starting value
        x0u(k) = pi/2;
      else
        x0u(k) = 2*(x0(i) - LB(i))/(UB(i)-LB(i)) - 1;
        % shift by 2*pi to avoid problems at zero in fminsearch
        % otherwise, the initial simplex is vanishingly small
        x0u(k) = 2*pi+asin(max(-1,min(1,x0u(k))));
      end

      % increment k
      k=k+1;
    case 0
      % unconstrained variable. x0u(i) is set.
      x0u(k) = x0(i);

      % increment k
      k=k+1;
    case 4
      % fixed variable. drop it before fminsearch sees it.
      % k is not incremented for this variable.
  end

end
% if any of the unknowns were fixed, then we need to shorten
% x0u now.
if k<=n
  x0u(k:n) = [];
end

% were all the variables fixed?
if isempty(x0u)
  % All variables were fixed. quit immediately, setting the
  % appropriate parameters, then return.

  % undo the variable transformations into the original space
  x = xtransform(x0u,params);

  % final reshape
  x = reshape(x,xsize);

  % stuff fval with the final value
  fval = feval(params.fun,x,params.args{:});

  % fminsearchbnd was not called
  exitflag = 0;
```

```matlab
  output.iterations = 0;
  output.funcCount = 1;
  output.algorithm = 'fminsearch';
  output.message = 'All variables were held fixed by the applied
bounds';

  % return with no call at all to fminsearch
  return
end

% Check for an outputfcn. If there is any, then substitute my
% own wrapper function.
if ~isempty(options.OutputFcn)
  params.OutputFcn = options.OutputFcn;
  options.OutputFcn = @outfun_wrapper;
end

% now we can call fminsearch, but with our own
% intra-objective function.
[xu,fval,exitflag,output] = fminsearch(@intrafun,x0u,options,params);

% undo the variable transformations into the original space
x = xtransform(xu,params);

% final reshape to make sure the result has the proper shape
x = reshape(x,xsize);

% Use a nested function as the OutputFcn wrapper
  function stop = outfun_wrapper(x,varargin);
    % we need to transform x first
    xtrans = xtransform(x,params);

    % then call the user supplied OutputFcn
    stop = params.OutputFcn(xtrans,varargin{1:(end-1)});

  end

end % mainline end

% =====================================
% ========= begin subfunctions =========
% =====================================
function fval = intrafun(x,params)
% transform variables, then call original function

% transform
xtrans = xtransform(x,params);

% and call fun
fval = feval(params.fun,reshape(xtrans,params.xsize),params.args{:});
```

135

```matlab
end % sub function intrafun end


% =====================================
function xtrans = xtransform(x,params)
% converts unconstrained variables into their original domains

xtrans = zeros(params.xsize);
% k allows some variables to be fixed, thus dropped from the
% optimization.
k=1;
for i = 1:params.n
  switch params.BoundClass(i)
    case 1
      % lower bound only
      xtrans(i) = params.LB(i) + x(k).^2;

      k=k+1;
    case 2
      % upper bound only
      xtrans(i) = params.UB(i) - x(k).^2;

      k=k+1;
    case 3
      % lower and upper bounds
      xtrans(i) = (sin(x(k))+1)/2;
      xtrans(i) = xtrans(i)*(params.UB(i) - params.LB(i)) +
params.LB(i);
      % just in case of any floating point problems
      xtrans(i) = max(params.LB(i),min(params.UB(i),xtrans(i)));

      k=k+1;
    case 4
      % fixed variable, bounds are equal, set it at either bound
      xtrans(i) = params.LB(i);
    case 0
      % unconstrained variable.
      xtrans(i) = x(k);

      k=k+1;
  end
end

end % sub function xtransform end
```

2. SAW wave modeling

```matlab
function val=Ni_fitting_three_value_3_11_16(x)    %*****

 %This function is used to calculate the difference between the
experimental and calculated SAW velocities at given Cij values

 %x: elastic constants [C11 C44 C12]
 %val: the difference between experimental and calculated SAW
velocities

sampling=4000;
rho=8.91*10^3;%kg/m^3 for Ni               %*****
lambda=7*10^-6; %m
k0=2*pi/lambda;
T=20*10^-13;%s
w0=2*pi/T;
offset=0;
w=w0+complex(0,0.000001*w0);


C11=x(1);
C44=x(2);
C12=x(3);

%vset values are velocities from experiment %*****
vset1=2886.7;
vset2=2396.0;
vset3=2914.3;
vset4=2612.7;
vset5=2640.3;
vset6=2812.3;
vset7=2808.1;
vset8=2897.3;
vset9=2899.4;

%Assembly
vset=[vset1,vset2,vset3,vset4,vset5,vset6,vset7,vset8,vset9]; %*****

EulerMatrix=[
    6.1857    2.2641    4.6373
    4.3537    2.4559    5.6268
    1.3703    1.5124    5.9412
    4.9150    2.7210    0.9819
    4.8803    2.7069    5.6597
    1.8460    1.5427    0.1308
    1.8413    1.5579    0.1312
    1.3812    1.5116    5.9108
    1.3606    1.5239    5.9416
    ];

Number=length(vset); % Number of measurements for elastic constants
```

137

```matlab
for flag=1:Number;

% Preallocate
F=zeros(3,3);
B=zeros(3,3);
M=zeros(3,3);
N=zeros(3,3);
POL=cell(3,3);
pp=zeros(1,3);
S=cell(1,3);
x=zeros(1,3);
y=zeros(1,3);
z=zeros(1,3);
A=zeros(3,3);
R=zeros(3,3);
I=zeros(3,3);
a=zeros(1,3);
G33=zeros(1,sampling);

%Evaluate the Cij
%C(3,3,3,3)=0;
C=zeros(3,3,3,3);
[C(1,1,1,1),C(2,2,2,2),C(3,3,3,3)]=deal(C11);
[C(1,1,2,2),C(1,1,3,3),C(2,2,3,3)]=deal(C12);
[C(2,3,2,3),C(1,3,1,3),C(1,2,1,2)]=deal(C44);

for i=1:3;
    for j=1:3;
        for k=1:3;
            for l=1:3;
                if C(i,j,k,l)~=0;

[C(j,i,k,l),C(i,j,l,k),C(j,i,l,k),C(k,l,i,j)]=deal(C(i,j,k,l));
                end
            end
        end
    end
end
deg=8;   %PDMS
orientation
%*****

MM=[cosd(90-deg) cosd(deg) 0;cosd(180-deg) cosd(90-deg) 0; 0 0 1]; %It
brings PDMS orientation into Sample coordinate system
%Euler angle plus MM brings PDMS coordinate system into coincidence
with crystalline coordinate system
C=C_modifi(C,(Euler2matrix(EulerMatrix(flag,1),EulerMatrix(flag,2),Eule
rMatrix(flag,3))*MM)');

%evaluate the initial k
for nx=1;
```

138

```matlab
    for ny=1:sampling;

k(1)=nx*k0;
k(2)=ny*k0;

%evaluate the quadratic coefficient
for i=1:3;
    for j=1:3;
        F(i,j)=C(i,3,3,j);
    end
end

%evaluate the linear coefficient
for i=1:3;
    for l=1:3;
        B(i,l)=0;
    end
end

for i=1:3;
    for l=1:3;
        for u=1:2;
            B(i,l)=B(i,l)-k(u)*C(i,u,3,l);
        end
            for v=1:2;
                B(i,l)=B(i,l)-k(v)*C(i,3,v,l);

            end

        M(i,l)=B(i,l)*complex(0,1);
    end
end

% Evaluate the constant coefficient

for i=1:3;
    for l=1:3;
        N(i,l)=0;
    end
end

for i=1:3;
    for l=1:3;
        N(i,l)=N(i,l)+rho*w^2*deltaij(i,l);
        for u=1:2;
            for v=1:2
                N(i,l)=N(i,l)-C(i,u,v,l)*k(u)*k(v);
            end
        end
    end
end
% Get the final expression
```

```matlab
for i=1:3;
    for j=1:3;
POL{i,j}=[F(i,j) M(i,j) N(i,j)];
    end
end
Poly=conv(conv(POL{1,1},POL{2,2}),POL{3,3})+conv(conv(POL{1,2},POL{2,3}
),POL{3,1})+conv(conv(POL{1,3},POL{2,1}),POL{3,2})-
conv(conv(POL{1,1},POL{2,3}),POL{3,2})-
conv(conv(POL{1,2},POL{2,1}),POL{3,3})-
conv(conv(POL{1,3},POL{2,2}),POL{3,1});
ppC=roots(Poly);
cont=0;
for i=1:length(ppC);
    if real(ppC(i)>0)
        cont=cont+1;
pp(cont)=ppC(i);
    end
end

% keep useful p values
%pp=[pp(1) pp(2) pp(3)];

% Solve to get A;;;;Notice imaginary number
for i=1:3;
    S{i}=F*pp(i)^2+M*pp(i)+N;
    temp=S{i};

     [NA,NB,NC]=svd(temp);
     Sol=NC(:,end);
     x(i)=Sol(1);
     y(i)=Sol(2);
     z(i)=Sol(3);

end

% %Choose the first set as the solution of A; First index: the number
of set;
% %Second: the order of the components

 for i=1:3;
    A(i,1)=x(i);
    A(i,2)=y(i);
    A(i,3)=z(i);
 end

 if(nx==0)&&(ny==0);
    A=eye(3);
 end

%boundary conditions to determine a
```

140

```matlab
for i=1:3;
    for r=1:3;
        R(i,r)=0;
        I(i,r)=0;
    end
end

%determine the coefficients of each a
for i=1:3;
    for r=1:3;
        for l=1:3;
            R(i,r)=R(i,r)+C(i,3,3,l)*pp(r)*A(r,l);
            for u=1:2;
                I(i,r)=I(i,r)+C(i,3,u,l)*k(u)*A(r,l);
            end
        end
    end
end
Comb=-R+I*complex(0,1);
del=[0 0 1]';

% Solve a by using determinant operatios
for r=1:3;
    Aug=Comb;
    Aug(:,r)=del;
    a(r)=det(Aug)/det(Comb);
end

%get G value
    G33(nx+offset,ny+offset)=0;
    for r=1:3;
        G33(nx+offset,ny+offset)=G33(nx+offset,ny+offset)+a(r)*A(r,3);
    end
    end
end

inc=1;
xx=1:sampling;
yy=real(G33(1,:));
xnew=1:inc:sampling;
ynew=spline(xx,yy,xnew);
YYnew=H_L_Peak_Ni(ynew,inc);                      %*****
Numer=1+inc*YYnew;
slownessnew=Numer*k0/real(w);
velocitynew=1./slownessnew;
%vel(flag)=velocitynew;
%velSet(flag)=velocitynew
%err(flag)=(velocity-vset(flag))/vset(flag);
%diff(flag)=abs(velocitynew-vset(flag))/vset(flag);
end
val=sum(diff);
```

```matlab
function y=H_L_Peak_Ni(var,inc)
%This function is to return the RW peak location considering the case
when
%maximum and minimum are so close
%y: RW peak slowness
%var: displacement
%inc: slowness

PeakTotal=find((diff(ynew))<0);
 dif=diff(ynew);
 MaxI=find(diff(sign(dif))==-2)+1; %Get the maximum indices
 MinI=find(diff(sign(dif))==2)+1;  %Get the mininum indices
 if length(MaxI)<2 || length(MinI)<2;  %If there is only one Peak, use
it as SAW
     y=(PeakTotal(end));
 elseif abs(xnew(MaxI(end-1))-xnew(MinI(end-1)))<1e-
5&&abs((ynew(MaxI(end-1))-ynew(MinI(end-1))))>1e-19; %difference
between Max and Min is larger and closer enough, count it as a peak
     y=(MaxI(end-1)+MinI(end-1))/2;
     if y*2.8571e-07<3.4e-4;  %If the slowness peak is too small, count
it as some useless fluctuation
         y=(PeakTotal(end));
     end
 elseif length(PeakTotal)==0;
     y=0;
else
y=(PeakTotal(end));
end
```

```matlab
function M=Euler2matrix(a,b,r)
%This program is to convert the Euler angle set to matrix
multiplication
%M: transformation matrix
%a,b,r: Input the Euler angles(radian) in order with the intrinsic
convention (Bunge's convention) z-x'-z''
%It brings the sample coordinate frame into coincidence with the
crystalline coordinate frame

Rza=[cos(a) sin(a) 0
    -sin(a) cos(a) 0
    0 0 1];

Rxb=[1 0 0
    0 cos(b) sin(b)
    0 -sin(b) cos(b)];

Rzr=[cos(r) sin(r) 0
    -sin(r) cos(r) 0
    0 0 1];

M=Rzr*Rxb*Rza;
```

```matlab
function newC=C_modifi(C,a)
%This function is used to transform C in the new coordinate frame based
on transformation matrix a
% C: input elastic constants;
% a: transformation matrix

newC=zeros(3,3,3,3);
for ip=1:3;
    for jp=1:3;
        for kp=1:3;
            for lp=1:3;
                for i=1:3;
                    for j=1:3;
                        for k=1:3;
                            for l=1:3;

newC(ip,jp,kp,lp)=newC(ip,jp,kp,lp)+a(ip,i)*a(jp,j)*a(kp,k)*a(lp,l)*C(i
,j,k,l);
                            end
                        end
                    end
                end
            end
        end
    end
end
```

3. Bulk wave modeling:

```
clear;
clc;
close all;
%Define the plane you have interest. The two axes must be perpendicular
 Xaxis=[1,0,0];
 Yaxis=[0,1,0];

run material_parameters;
L=1;%Longitudinal mode;
SV=2;%Shear mode vibrating in sagital plane
SH=3;%Shear mode (Lame mode)
%Get basic information of the material
[CIJ,dens,name,DIJ,PIJ]=parameter(Ni);
%Solve the eigen problems
[vphase,slowness,angle]=Christoffel_directEig_piezo(CIJ,Xaxis,Yaxis,den
s,DIJ,PIJ,'non-piezo');
%[vphaseNonPiezo,slownessNonPiezo,angle2]=Christoffel_directEig_piezo(C
IJ,Xaxis,Yaxis,dens,DIJ,PIJ,'non-piezo');


for i=1:length(vphase)
vpx(i,:)=vphase(i,:)*cos(angle(i));
vpy(i,:)=vphase(i,:)*sin(angle(i));
sx(i,:)=slowness(i,:)*cos(angle(i));
sy(i,:)=slowness(i,:)*sin(angle(i));
end

%This is to draw the phase velocity
figure(1)
plot(vpx,vpy)
legend('(Quasi)L','(Quasi)SV','(Quasi)SH')
xlabel('phase velocity in km/s')
title([name ,'  surface ','x: [',num2str(Xaxis),']   y:
[',num2str(Yaxis),']'])
grid on
axis tight
axis equal

%This is to draw the slowness space
figure(2)
plot(sx/1000,sy/1000,'o')
legend('(Quasi)L','(Quasi)SV','(Quasi)SH','Location','NorthEast')
xlabel('slowness in s/m')
% xlim([-4,4]*1e-4);
% ylim=([-4,4]*1e-4);
title(['  slowness surface ','x: [',num2str(Xaxis),']   y:
[',num2str(Yaxis),']'])

grid on
axis tight
```

145

```matlab
axis equal

%This is to draw the power flow angle in degree, which is the angle
between the propagation vector and energy velocity vector
for i=1:length(slowness)
 [Sbrch1(i,1),Sbrch1(i,2)]=P2C(slowness(i,1),angle(i));
 [Sbrch2(i,1),Sbrch2(i,2)]=P2C(slowness(i,2),angle(i));
 [Sbrch3(i,1),Sbrch3(i,2)]=P2C(slowness(i,3),angle(i));
end

for i=1:length(slowness)

    if i==length(slowness)
        [Vgdir1(:,i),phi1(i)]=PowerFlowAngle(Sbrch1(i,:),Sbrch1(1,:));
        [Vgdir2(:,i),phi2(i)]=PowerFlowAngle(Sbrch2(i,:),Sbrch2(1,:));
        [Vgdir3(:,i),phi3(i)]=PowerFlowAngle(Sbrch3(i,:),Sbrch3(1,:));
    else

[Vgdir1(:,i),phi1(i)]=PowerFlowAngle(Sbrch1(i,:),Sbrch1(i+1,:));

[Vgdir2(:,i),phi2(i)]=PowerFlowAngle(Sbrch2(i,:),Sbrch2(i+1,:));

[Vgdir3(:,i),phi3(i)]=PowerFlowAngle(Sbrch3(i,:),Sbrch3(i+1,:));
    end
end

figure(3)
plot(angle*180/pi,phi1,'b',angle*180/pi,phi2,'r',angle*180/pi,phi3,'k',
'Markersize',3)
xlim([0,180])
legend('(Quasi)L','(Quasi)SV','(Quasi)SH')
xlabel('Power Flow Angle in degree')
title([name ,'  surface ','x: [',num2str(Xaxis),']   y:
[',num2str(Yaxis),']'])
grid on

%This is to draw the ray surface
vgroup(:,1)=vphase(:,1)./(cosd(phi1'));
vgroup(:,2)=vphase(:,2)./(cosd(phi2'));
vgroup(:,3)=vphase(:,3)./(cosd(phi3'));

vgx(:,1)=vgroup(:,1).*Vgdir1(1,:)';
vgy(:,1)=vgroup(:,1).*Vgdir1(2,:)';
vgx(:,2)=vgroup(:,2).*Vgdir2(1,:)';
vgy(:,2)=vgroup(:,2).*Vgdir2(2,:)';
vgx(:,3)=vgroup(:,3).*Vgdir3(1,:)';
vgy(:,3)=vgroup(:,3).*Vgdir3(2,:)';

figure(4)
plot(vgx,vgy)
legend('(Quasi)L','(Quasi)SV','(Quasi)SH')
xlabel('Ray surface')
```

146

```matlab
title([name ,'  surface ','x: [',num2str(Xaxis),']   y:
[',num2str(Yaxis),']'])
grid on
axis tight
axis equal

%This is to get and draw electro-mechanical coupling constant
Ksquare=(vphase-vphaseNonPiezo).^2./(vphase.^2);
ktsquare=Ksquare./(Ksquare+1);
kt=sqrt(ktsquare);
figure(5)
plot(angle*180/pi,kt(:,1),'b',angle*180/pi,kt(:,2),'r',angle*180/pi,kt(
:,3),'k')
legend('(Quasi)L','(Quasi)SV','(Quasi)SH')
xlabel('Angle of acoustic propagation vector')
ylabel('coupling constant')
xlim([0,180])
title([name ,'  surface ','x: [',num2str(Xaxis),']   y:
[',num2str(Yaxis),']'])
grid on

figure(6)
for i=1:length(vphase)
sxNon(i,:)=slownessNonPiezo(i,:)*cos(angle(i));
syNon(i,:)=slownessNonPiezo(i,:)*sin(angle(i));
end
plot(sxNon(:,1),syNon(:,1),'b',sx(:,1),sy(:,1),'r')
legend('non-piezo','piezo')
xlabel('Slowness')
title([name ,'  surface ','x: [',num2str(Xaxis),']   y:
[',num2str(Yaxis),']'])
grid on
axis tight
axis equal

figure(7)
plot(angle*180/pi,vphase)
legend('(Quasi)L','(Quasi)SV','(Quasi)SH')
xlabel('angle')
ylabel('velosity')
title([name ,'  surface ','x: [',num2str(Xaxis),']   y:
[',num2str(Yaxis),']'])
grid on
```

```matlab
function [CIJ,dens,name,DIJ,PIJ]=parameter(mat)
%This function is to get material properties from the data base

CIJ=CIJassign(mat.indepC,mat.class)
dens=mat.density
name=mat.fomular


if isfield(mat,'indepD')
    %isfield is used to check whether an item in a structure exists.
For variable existance, use the function exist.

    DIJ=DIJassign(mat.indepD,mat.subclass);
else
    DIJ=[];
end

if isfield(mat,'indepP')
    %isfield is used to check whether an item in a structure exists.
For variable existance, use the function exist.

    PIJ=PIJassign(mat.indepP,mat.class);
else
    PIJ=[];
end
```

```matlab
function
[vphase,slowness,angle]=Christoffel_directEig_piezo(CIJ,Xaxis,Yaxis,den
s,DIJ,PIJ,varargin)

%preallocate
L36=zeros(3,6);
L63=zeros(6,3);
Chris=zeros(3,3);%Christoffel matrix
vphase=zeros(1,3);
slowness=zeros(1,3);


%Construct space
if dot(Xaxis,Yaxis)>1e-3
    error('The axes are not perpendicular')
end
xaxis=Xaxis/norm(Xaxis);
yaxis=Yaxis/norm(Yaxis);
% make sure x and y axis are perpendicular
zaxis=cross(xaxis,yaxis);
R1=[xaxis;yaxis;zaxis];

increment=pi/180;
for theta=0:increment:2*pi-increment;  %*****
    SS=[cos(theta),sin(theta),0];
    L13=SS*R1;%This is used to get the direction cosine


%Construct divergence matrix operator
dirx=L13(1,1);
diry=L13(1,2);
dirz=L13(1,3);

L36(1,1)=dirx;
L36(1,5)=dirz;
L36(1,6)=diry;
L36(2,2)=diry;
L36(2,4)=dirz;
L36(2,6)=dirx;
L36(3,3)=dirz;
L36(3,4)=diry;
L36(3,5)=dirx;

%Construct Christoffel matrix
if (nargin<7)|(strcmp(varargin{1},'non-piezo'));
   Chris=L36*CIJ*L36';

elseif (strcmp(varargin{1},'piezo'))

    if isempty(DIJ);
        vphase=0;
        slowness=0;
```

149

```matlab
        angle=0;
        return;
    else %This if structure is used to avoid the interference of piezo
parameters requirement on non-piezoelectric materials

 e=CIJ*DIJ'*1e9;%This is the definition of e (called piezoelectric
stress matrix), which is 6X3
 assignin('base','e',e)%this is to display the local variable e into
the workspace. It's particulaly useful in debugging
 %(C unit: MPa; e unit: C/m^2; DIJ (called piezoelectric strain matrix
unit: C/N)
 %Multiply by 1e9 is to convert MPa to Pa (N/m^2)
    numerator=(e*L13')*(e*L13')';
    denomenator=L13*PIJ*L13';
    CIJs=CIJ+numerator/denomenator/1e9;
    Chris=L36*CIJs*L36';
    end
else
    disp('Include piezoelectricity: piezo')
    disp('Do not include piezoelectricity: default or non-piezo')
    error('Input the type again')
end


[vector value]=eig(Chris,'vector'); %Get eigenvectors and eigenvalues
%Assign each eigenvalue to its eigenvector
valueSort=ModeMatch(vector,value,zaxis,L13);%The order: L,SV,SH
velocity=sqrt(valueSort/dens);
vphase=[vphase;velocity];
velX=velocity*cos(theta);
velY=velocity*sin(theta);

end
% hold off
% axis tight
% axis equal
% grid on
vphase(1,:)=[];
slowness=1./vphase;
angle=0:increment:2*pi-increment;  %*****
angle=angle';
```

```matlab
function CIJ=CIJassign(indepC,varargin)
% This function is used to construct the CIJ matrix.
% Format: CIJassign(indepC,varargin), where indepC stands for the
independent elastic constants. Numbering is from
% lowest to the highest, like C11,C12,C13...C16, C21,C22
% varargin is used to specify the class type (cubic by default)
if nargin<2|(strcmp(varargin{1},'cubic'))
    if length(indepC)~=3
        error('The number of independent elastic constants don''t match
this class')
    end
C11=indepC(1);
C12=indepC(2);
C44=indepC(3);
CIJ=zeros(6,6);
[CIJ(1,1),CIJ(2,2),CIJ(3,3)]=deal(C11);
[CIJ(1,2),CIJ(1,3),CIJ(2,3)]=deal(C12);
[CIJ(4,4),CIJ(5,5),CIJ(6,6)]=deal(C44);

elseif (strcmp(varargin{1},'isotropic'))
    if length(indepC)==2
        disp('Make sure you input C11 and C12 in GPa')

        C11=indepC(1);
        C12=indepC(2);
        C44=(C11-C12)/2;
    elseif length(indepC)==3
        C11=indepC(1);
        C12=indepC(2);
        C44=indepC(3);
    else
        error('The number of independent elastic constants don''t match
this class')
    end

CIJ=zeros(6,6);
[CIJ(1,1),CIJ(2,2),CIJ(3,3)]=deal(C11);
[CIJ(1,2),CIJ(1,3),CIJ(2,3)]=deal(C12);
[CIJ(4,4),CIJ(5,5),CIJ(6,6)]=deal(C44);

elseif (strcmp(varargin{1},'tetragonal'))
    if length(indepC)~=7
        error('The number of independent elastic constants don''t match
this class')
    end
C11=indepC(1);
C12=indepC(2);
C13=indepC(3);
C16=indepC(4);
C33=indepC(5);
C44=indepC(6);
C66=indepC(7);
```

151

```matlab
CIJ=zeros(6,6);
[CIJ(1,1),CIJ(2,2)]=deal(C11);
[CIJ(1,2)]=deal(C12);
[CIJ(1,3),CIJ(2,3)]=deal(C13);
[CIJ(1,6)]=deal(C16);
[CIJ(2,6)]=-deal(C16);
[CIJ(3,3)]=deal(C33);
[CIJ(4,4),CIJ(5,5)]=deal(C44);
[CIJ(6,6)]=deal(C66);

elseif (strcmp(varargin{1},'orthorhombic'))
    if length(indepC)~=9
        error('The number of independent elastic constants don''t match
this class')
    end
C11=indepC(1);
C12=indepC(2);
C13=indepC(3);
C22=indepC(4);
C23=indepC(5);
C33=indepC(6);
C44=indepC(7);
C55=indepC(8);
C66=indepC(9);

CIJ=zeros(6,6);
[CIJ(1,1)]=deal(C11);
[CIJ(1,2)]=deal(C12);
[CIJ(1,3)]=deal(C13);
[CIJ(2,2)]=deal(C22);
[CIJ(2,3)]=deal(C23);
[CIJ(3,3)]=deal(C33);
[CIJ(4,4)]=deal(C44);
[CIJ(5,5)]=deal(C55);
[CIJ(6,6)]=deal(C66);

elseif (strcmp(varargin{1},'trigonal'))
    if length(indepC)~=6
        error('The number of independent elastic constants don''t match
this class')
    end
C11=indepC(1);
C12=indepC(2);
C13=indepC(3);
C14=indepC(4);
C33=indepC(5);
C44=indepC(6);


CIJ=zeros(6,6);
[CIJ(1,1), CIJ(2,2)]=deal(C11);
[CIJ(1,2)]=deal(C12);
[CIJ(1,3),CIJ(2,3)]=deal(C13);
```

```
[CIJ(1,4),CIJ(5,6)]=deal(C14);
[CIJ(2,4)]=-deal(C14);
[CIJ(3,3)]=deal(C33);
[CIJ(4,4),CIJ(5,5)]=deal(C44);
[CIJ(6,6)]=(C11-C12)/2;

elseif (strcmp(varargin{1},'monoclinic'))
    if length(indepC)~=13
        error('The number of independent elastic constants don''t match
this class')
    end

 C11=indepC(1);
 C22=indepC(2);
 C33=indepC(3);
 C44=indepC(4);
 C55=indepC(5);
 C66=indepC(6);
 C12=indepC(7);
 C13=indepC(8);
 C23=indepC(9);
 C15=indepC(10);
 C25=indepC(11);
 C35=indepC(12);
 C46=indepC(13);

 CIJ=zeros(6,6);
[CIJ(1,1)]=deal(C11);
[CIJ(2,2)]=deal(C22);
[CIJ(3,3)]=deal(C33);
[CIJ(4,4)]=deal(C44);
[CIJ(5,5)]=deal(C55);
[CIJ(6,6)]=deal(C66);
[CIJ(1,2)]=deal(C12);
[CIJ(1,3)]=deal(C13);
[CIJ(2,3)]=deal(C23);
[CIJ(1,5)]=deal(C15);
[CIJ(2,5)]=deal(C25);
[CIJ(3,5)]=deal(C35);
[CIJ(4,6)]=deal(C46);

else
    error('Check spelling of class type or class is missing here')
end

for I=1:6;
    for J=I:6;
        CIJ(J,I)=deal(CIJ(I,J));

    end
end
```

```matlab
function DIJ=DIJassign(indepD,varargin)
% This function is used to construct the CIJ matrix.
% Format: CIJassign(indepC,varargin), where indepC stands for the
independent elastic constants. Numbering is from
% lowest to the highest, like C11,C12,C13...C16, C21,C22
% varargin is used to specify the class type (cubic by default)
if nargin<2|(strcmp(varargin{1},'cubic'))
    disp('Only valid for 4bar3m and 23')
    if length(indepD)~=1
        error('The number of independent piezoelectric constants don''t
match this situation')
    end
D14=indepD(1);
DIJ=zeros(3,6);
[DIJ(1,4),DIJ(2,5),DIJ(3,6)]=deal(D14);


elseif (strcmp(varargin{1},'tetragonal'))
    if length(indepD)~=7
        error('The number of independent elastic constants don''t match
this class')
    end
D11=indepD(1);
C12=indepD(2);
C13=indepD(3);
C16=indepD(4);
C33=indepD(5);
C44=indepD(6);
C66=indepD(7);

DIJ=zeros(6,6);
[DIJ(1,1),DIJ(2,2)]=deal(D11);
[DIJ(1,2)]=deal(C12);
[DIJ(1,3),DIJ(2,3)]=deal(C13);
[DIJ(1,6)]=deal(C16);
[DIJ(2,6)]=-deal(C16);
[DIJ(3,3)]=deal(C33);
[DIJ(4,4),DIJ(5,5)]=deal(C44);
[DIJ(6,6)]=deal(C66);

elseif (strcmp(varargin{1},'orthorhombic'))
    if length(indepD)~=9
        error('The number of independent elastic constants don''t match
this class')
    end
D11=indepD(1);
C12=indepD(2);
C13=indepD(3);
C22=indepD(4);
C23=indepD(5);
C33=indepD(6);
C44=indepD(7);
C55=indepD(8);
```

```matlab
C66=indepD(9);

DIJ=zeros(6,6);
[DIJ(1,1)]=deal(D11);
[DIJ(1,2)]=deal(C12);
[DIJ(1,3)]=deal(C13);
[DIJ(2,2)]=deal(C22);
[DIJ(2,3)]=deal(C23);
[DIJ(3,3)]=deal(C33);
[DIJ(4,4)]=deal(C44);
[DIJ(5,5)]=deal(C55);
[DIJ(6,6)]=deal(C66);

elseif (strcmp(varargin{1},'3m m x1'))
    if length(indepD)~=4
        error('The number of independent piezoelectric constants don''t
match this situation')
    end
D15=indepD(1);
D16=indepD(2);
D31=indepD(3);
D33=indepD(4);

DIJ=zeros(3,6);
[DIJ(1,5), DIJ(2,4)]=deal(D15);
[DIJ(1,6)]=deal(D16);
[DIJ(2,1)]=deal(D16)/2;
[DIJ(2,2)]=-deal(D16)/2;
[DIJ(3,1),DIJ(3,2)]=deal(D31);
[DIJ(3,3)]=deal(D33);


else
    %error('Check spelling of class type or class is missing here')
    DIJ=[];
end
```

Reference

1. Mura, T. *Micromechanics of Defects in Solids*. (Kluwer Academic/Springer, 1987).

2. Schuren, J. C. *et al.* New opportunities for quantitative tracking of polycrystal responses in three dimensions. *Curr. Opin. Solid State Mater. Sci.* **19,** 235–244 (2015).

3. Chen, L.-Q. Phase-field models for microstructure evolution. *Annu. Rev. Mater. Res.* **32,** 113–140 (2002).

4. Wang, Y. & Li, J. Phase field modeling of defects and deformation. *Acta Mater.* **58,** 1212–1235 (2010).

5. De Jong, M. *et al.* Charting the complete elastic properties of inorganic crystalline compounds. *Sci. Data* **2,** 1–13 (2015).

6. Łopuszyński, M. & Majewski, J. Composition dependence of elastic constants in wurtzite AlGaInN alloys. *J. Appl. Phys.* **111,** 33502 (2012).

7. Wang, X. *et al.* Computational modeling of elastic constants as a function of temperature and composition in Zr–Nb alloys. *CALPHAD Comput. Coupling Phase Diagrams Thermochem.* **48,** 89–94 (2015).

8. Chelli, S. *et al.* Ab-initio study of structural, elastic, electronic and thermodynamic

properties of $Ba_xSr_{1-x}S$ ternary alloys. *Mater. Sci. Pol.* **33,** 879–886 (2015).

9.   Sun, X.-W. *et al.* The structural, elastic, and electronic properties of $Zr_xNb_{1-x}C$ alloys from first principle calculations. *Chinese Phys. B* **22,** 107105 (2013).

10.   Sandstrom, R. & Korzhavyi, P. Use of elastic constants based on ab initio computation in materials optimisation of austenitic stainless steels. *Can. Metall. Q.* **53,** 282–291 (2014).

11.   Vashishta, P. *et al.* Interaction potential for silicon carbide : A molecular dynamics study of elastic constants and vibrational density of states for crystalline and amorphous silicon carbide. *J. Appl. Phys.* **101,** 103515 (2007).

12.   Shokrieh, M. M., Esmkhani, M., Shokrieh, Z. & Zhao, Z. Stiffness prediction of graphene nanoplatelet/epoxy nanocomposites by a combined molecular dynamics-micromechanics method. *Comput. Mater. Sci.* **92,** 444–450 (2014).

13.   Lee, S., Park, J., Sastry, A. M. & Lu, W. Molecular dynamics simulations of SOC-dependent elasticity of $Li_xMn_2O_4$ spinels in Li-ion batteries. *J. Electrochem. Soc.* **160,** A968–A972 (2013).

14.   Enemark, S., Deriu, M., Soncini, M. & Redaelli, A. Mechanical model of the tubulin dimer based on molecular dynamics simulations. *J. Biomech. Eng.* **130,** 41008 (2008).

15.   Barker Jr, R. E. An approximate relation between elastic moduli and thermal expansivities. *J. Appl. Phys.* **34,** 107–116 (1963).

16.   Ledbetter, H. Thermal expansion and elastic constants. *Int. J. Thermophys.* **12,** 637–642 (1991).

157

17.   Anderson, O. L. A simplified method for calculating the Debye temperature from elastic constants. *J. Phys. Chem. Solids* **24,** 909–917 (1963).

18.   Alers, G. A. & Neighbours, J. R. Comparison of the Debye temperature determined from elastic constants and calorimetry. *Rev. Mod. Phys.* **31,** 675–680 (1959).

19.   Siethoff, H. & Ahlborn, K. The dependence of the Debye temperature on the elastic constants. *Phys. Status Solidi* **190,** 179–191 (1995).

20.   Jia, T., Chen, G. & Zhang, Y. Lattice thermal conductivity evaluated using elastic properties. *Phys. Rev. B* **95,** 155206 (2017).

21.   Phillips, C. Experimental determination of the low-temperature Grüneisen parameter of silicon from pressure derivatives of elastic constants. *Phys. Rev. B* **1,** 1548–1551 (1970).

22.   Bruls, G., Weber, D., Wolf, B., Thalmeier, P. & Luthi, B. Strain-order-parameter coupling and phase diagrams in superconducting UPt$_3$. *Phys. Rev. Lett.* **65,** 2294–2297 (1990).

23.   Nye, J. F. *Physical Properties of Crystals*. (Oxford University Press, 1985).

24.   Ferrar, W. L. *Algebra; a text-book of determinants , matrices, and algebraic forms*. (Oxford at the Clarendon press, 1941).

25.   Standard test methods for shear modulus at room temperature. *ASTM Stand. E143* (2013).

26.   Standard test methods of compression testing of metallic materials at room temperature. *ASTM Stand. E 9* (2009).

27. Standard test methods for tension testing of metallic materials. *ASTM Stand. E 8 E 8M* (2013).

28. Pestka, K. a. *et al.* Experimental measurement of the elastic constants of $GdScO_3$ via resonant ultrasound spectroscopy utilizing ab initio calculations. *Appl. Phys. Lett.* **92,** 111915 (2008).

29. Migliori, A. & Sarrao, J. *Resonant Ultrasound Spectroscopy: Applications to Physics, Materials Measurements, and Nondestructive Evaluation*. (Wiley-VCH, 1997).

30. Sun, M. Optimal recovery of elastic properties for anisotropic materials through ultrasonic measurements. (The University of Maine, 2002).

31. Xu, Y., Aizawa, T. & Kihara, J. Structure of surface wave on coarse-grained nickel observed by acoustic spectro-microscopy. *Mater. Trans. JIM* **37,** 1690–1698 (1996).

32. Benedek, G. B. & Fritsch, K. Brillouin scattering in cubic crystals. *Phys. Rev.* **107,** 647–662 (1966).

33. Search, H., Journals, C., Contact, A., Iopscience, M. & Address, I. P. Brillouin scattering study of gallium nitride : elastic stiffness constants. *J. Phys. Condens. Matter* **9,** 241–248 (1997).

34. Hayes, W. & Loudon, R. *Scattering of Light by Crystals*. (New York : Wiley, 1978).

35. Every, A. G. General closed-form expressions for acoustic waves in elastically anisotropic solids. *Phys. Rev. B* **22,** 1746–1760 (1980).

36. Kim, K. Y., Sachse, W. & Every, A. G. On the determination of sound speeds in cubic crystals and isotropic media using a broadband ultrasonic point-source/point-receiver method. *J. Acoust. Soc. Am.* **93,** 1393–1406 (1993).

37. Every, A. & Sachse, W. Determination of the elastic constants of anisotropic solids from acoustic-wave group-velocity measurements. *Phys. Rev. B* **42,** 8196–8205 (1990).

38. Rosenbaum, J. F. *Bulk Acoustic Wave Theory and Devices*. (Artech Print on Demand, 1988).

39. Antonelli, G. A., Zannitto, P. & Maris, H. J. New method for the generation of surface acoustic waves of high frequency. *Phys. B Condens. Matter* **316–317,** 377–379 (2002).

40. Farnell, G. W. Properties of elastic surface waves. *Phys. Acoust.* **6,** 77–102 (1970).

41. Milsom, R. F., Reilly, N. H. C. & Redwood, M. Analysis of generation and detection of surface and bulk acoustic waves by interdigital transducers. *IEEE Trans. Sonics Ultrason.* **SU-24,** 147–166 (1977).

42. Bu, G. *et al.* Surface acoustic wave velocity in single-crystal AlN substrates. *IEEE Trans. Ultrason. Ferroelectr. Freq. Control* **53,** 251–254 (2006).

43. Taylor, B., Maris, H. J. & Elbaum, C. Phonon focusing in solids. *Phys. Rev. Lett.* **23,** 416–419 (1969).

44. Camley, R. E. & Maradudin, A. A. Phonon focusing at surfaces. *Phys. Rev. B* **27,** 1959–1964 (1983).

45. Kolomenskii, A. A. & Maznev, A. A. Phonon-focusing effect with laser-generated

ultrasonic surface waves. *Phys. Rev. B* **48,** 14502 (1993).

46. Maznev, A. A., Kolomenskii, A. A. & Hess, P. Time-resolved cuspidal structure in the wave front of surface acoustic pulses on (111) gallium arsenide. *Phys. Rev. Lett.* **75,** 3332–3335 (1995).

47. Hong, Y., Sharples, S. D., Clark, M. & Somekh, M. G. Rapid and accurate analysis of surface and pseudo-surface waves using adaptive laser ultrasound techniques. *Ultrasonics* **42,** 515–518 (2004).

48. Sharples, S. D., Clark, M., Li, W. & Somekh, M. G. Rapid imaging of microstructure using spatially resolved acoustic spectroscopy. in *International Symposium on Laser Ultrasonics: Science, Technology and Applications* (2008).

49. Smith, R., Sharples, S., Li, W., Clark, M. & Somekh, M. Orientation imaging using spatially resolved acoustic spectroscopy. in *Anglo-French Physical Acoustics Conference (AFPAC 2011)* **353,** 1–7 (2012).

50. Sharples, S. D., Clark, M. & Somekh, M. G. Spatially resolved acoustic spectroscopy for fast noncontact imaging of material microstructure. **14,** 10435–10440 (2006).

51. Li, Q. *et al.* Generation and control of ultrashort-wavelength two-dimensional surface acoustic waves at nanoscale interfaces. *Phys. Rev. B* **85,** 195431 (2012).

52. Siemens, M. E. *et al.* High-frequency surface acoustic wave propagation in nanostructures characterized by coherent extreme ultraviolet beams. *Appl. Phys. Lett.* **94,** 93103 (2009).

53. Hurley, D. H. & Telschow, K. L. Picosecond surface acoustic waves using a

suboptical wavelength absorption grating. *Phys. Rev. B* **66,** 153301 (2002).

54. Sadhu, J., Lee, J. H. & Sinha, S. Frequency shift and attenuation of hypersonic surface acoustic phonons under metallic gratings. *Appl. Phys. Lett.* **97,** 133106 (2010).

55. Rogers, J. A., Maznev, A. A., Banet, M. J. & Nelson, K. A. Optical generation and characterization of acoustic waves in thin films: fundamentals and applications. *Annu. Rev. Mater. Sci.* **30,** 117–157 (2000).

56. Nelson, K. A. Characterization of 6FDA-APLBP polyimide films through impulsive stimulated thermal scattering. *J. Mater. Sci.* **30,** 5960–5966 (1995).

57. Banet, M. J. *et al.* High-precision film thickness determination using a laser-based ultrasonic technique. *Appl. Phys. Lett.* **73,** 169 (1998).

58. Rogers, J. A. *et al.* Optical system for rapid materials characterization with the transient grating technique : application to nondestructive evaluation of thin films used in microelectronics. *Appl. Phys. Lett.* **71,** 225–227 (2001).

59. Zhao, P., Zhao, J.-C. & Weaver, R. Dynamic surface acoustic response to a thermal expansion source on an anisotropic half space. *J. Acoust. Soc. Am.* **133,** 2634–2640 (2013).

60. Every, A. G., Kim, K. Y. & Maznev, A. A. The elastodynamic response of a semi-infinite anisotropic solid to sudden surface loading. *J. Acoust. Soc. Am.* **102,** 1346–1355 (1997).

61. Favretto-Cristini, N., Komatitsch, D., Carcione, J. M. & Cavallini, F. Elastic surface waves in crystals. Part 1: review of the physics. *Ultrasonics* **51,** 653–60

(2011).

62.   Hoop, A. T. D. E. A modification of Cagniard's method for solving seismic pulse
      problems. *Appl. Sci. Res.* **8,** 349–356 (1960).

63.   Achenbach, C.-Y. W. & J. D. A new method to obtain 3-D Green's functions for
      anisotropic solids. *Wave Motion* **18,** 273 (2993).

64.   Wei, C., Zheng, X., Cahill, D. G. & Zhao, J.-C. Invited article: micron resolution
      spatially resolved measurement of heat capacity using dual-frequency time-domain
      thermoreflectance. *Rev. Sci. Instrum.* **84,** 71301 (2013).

65.   Li, D., Zhao, P., Zhao, J.-C. & Cahill, D. G. Generation and detection of gigahertz
      surface acoustic waves using an elastomeric phase-shift mask. *J. Appl. Phys.* **114,**
      143102 (2013).

66.   Nowinski, J. L. *Theory of Thermoelasticity with Applications*. (Springer
      Netherlands, 1978).

67.   Antonelli, G. A., Perrin, B., Daly, B. C. & Cahill, D. G. Characterization of
      Mechanical and Thermal Properties Using Ultrafast Optical Metrology. **31,** 607–
      613 (2006).

68.   Nelson, K. A., Fayer, M. D., Nelson, K. A. & Fayersl, M. D. Laser induced
      phonons : A probe of intermolecular interactions in molecular solids. *J. Chem.
      Phys.* **72,** 5202–5218 (1980).

69.   Frigo, M. & Johnson, S. G. FFTW: An adaptive software architecture for the FFT.
      in *International Conference on Acoustics, Speech, and Signal Processing* 1381–
      1384 (1998).

70. Oppenheim, A. V., Schafer., R. W. & Buck, J. R. *Discrete-Time Signal Processing*. (Prentice Hall INC, 1999).

71. Lagarias, J. C., Reeds, J. A., Wright, M. H. & Wright, P. E. Convergence properties of the Nelder–Mead simplex method in low dimensions. *Soc. Ind. Appl. Math.* **9,** 112–147 (1998).

72. Epstein, S. G. & Carlson, O. N. The elastic constants of nickel-copper alloy single crystals. *Acta Metall.* **13,** 487–491 (1965).

73. Thomas, J. F. Third-order elastic constants of aluminum. *Phys. Rev.* **175,** 955–962 (1968).

74. Soga, N. Comparison of measured and predicted bulk moduli of tantalum and tungsten at high temperatures. *J. Appl. Phys.* **37,** 3416–3420 (1966).

75. Bolef, D. I. Elastic constants of single crystals of the bcc transition elements V, Nb, and Ta. *J. Appl. Phys.* **32,** 100–105 (1961).

76. Leese, J. & Lord, a. E. Elastic stiffness coefficients of single-crystal iron from room temperature to 500°C. *J. Appl. Phys.* **39,** 3986–3988 (1968).

77. Mcskimin, H. J. Measurement of the elastic constants of single crystal cobalt. *J. Appl. Phys.* **26,** 406–409 (1955).

78. Kammer, E. W., Cardinal, L. C., Vold, C. L. & Glicksman, M. E. The elastic constants for single-crystal bismuth and tin from room temperature to the melting point. *J. Phys. Chem. Solids* **33,** 1891–1898 (1972).

79. McCulloch, W. S. & Pitts, W. A logical calculus of the ideas immanent in nervous activity. *Bull. Math. Biophys.* **5,** 115–133 (1943).

80. Koch, N., Welzel, U., Wern, H. & Mittemeijer, E. J. Mechanical elastic constants and diffraction stress factors of macroscopically elastically anisotropic polycrystals: The effect of grain-shape (morphological) texture. *Philos. Mag.* **84,** 3547–3570 (2004).

81. Odegard, G. M., Clancy, T. C. & Gates, T. S. Modeling of the mechanical properties of nanoparticle/polymer composites. *Polymer.* **46,** 553–562 (2005).

82. Burg, V., Toonder, .J., Dijken, A., Hoefnagels, J. & Geers, M. Characterization method for mechanical properties of thin freestanding metal films for RF-MEMS. in *Thermal, Mechanical and Multiphysics Simulation and Experiments in Micro-Electronics and Micro-Systems* 1–7 (2006).

83. Leo, P. H., Lowengrub, J. S. & Nie, Q. Microstructural evolution in orthotropic elastic media. *J. Comput. Phys.* **157,** 44–88 (2000).

84. Li, X., Lowengrub, J., Nie, Q., Cristini, V. & Leo, P. Microstructure evolution in three-dimensional inhomogeneous elastic media. *Metall. Mater. Trans. A* **34A,** 1421–1431 (2003).

85. Shin, J. H., Jeong, J. & Lee, J. W. Microstructural evolution and the variation of tensile behavior after aging heat treatment of precipitation hardened martensitic steel. *Mater. Charact.* **99,** 230–237 (2015).

86. Morales, F. M. *et al.* Determination of the composition of $In_xGa_{1-x}N$ from strain measurements. *Acta Mater.* **57,** 5681–5692 (2009).

87. Mánuel, J. M. *et al.* Structural and compositional homogeneity of InAlN epitaxial layers nearly lattice-matched to GaN. *Acta Mater.* **58,** 4120–4125 (2010).

88. Łepkowski, S. P. & Gorczyca, I. Ab initio study of elastic constants in $In_xGa_{1-x}N$ and $In_xAl_{1-x}N$ wurtzite alloys. *Phys. Rev. B* **83,** 203201 (2011).

89. Łopuszyński, M. & Majewski, J. A. Computational study of structural and elastic properties of random $Al_xGa_yIn_{1-x-y}N$ alloys. *J. Phys. Condens. Matter* **22,** 205801 (2010).

90. Keating, P. N. Effect of invariance requirements on the elastic strain energy of crystals with application to the diamond structure. *Phys. Rev.* **145,** 637–645 (1966).

91. Golding, B., Moss, S. C. & Averbach, B. . Composition and pressure dependence of the elastic constants of gold-nickel alloys. *Phys. Rev. Rev.* **158,** 637–646 (1967).

92. Ashkenazi, J., Dacorogna, M., Peter, M., Talmor, Y. & Walker, E. Elastic constants in Nb-Zr alloys from zero temperature to the melting point: Experiment and theory. *Phys. Rev. B* **18,** 4120–4131 (1978).

93. Sakurai, J., Fujii, M., Nakamura, Y. & Takaki, H. Elastic constants of Ni-Fe and Ni-Cu alloys. *J. Phys. Soc. Japan* **19,** 308–310 (1964).

94. Hayes, D. J. & Brotzen, F. R. Elastic constants of niobium-rich zirconium alloys between 4.2K and room temperature. *J. Appl. Phys.* **45,** 1721–1725 (1974).

95. Xia, Y. Z., Bei, H., Gao, Y. F., Catoor, D. & George, E. P. Synthesis, characterization, and nanoindentation response of single crystal Fe-Cr-Ni alloys with FCC and BCC structures. *Mater. Sci. Eng. A* **611,** 177–187 (2014).

96. Zhao, J.-C. A combinatorial approach for structural materials. *Adv. Eng. Mater.* **3,** 143–147 (2001).

97.   Zhao, J.-C. Reliability of the diffusion-multiple approach for phase diagram mapping. *J. Mater. Sci.* **39,** 3913–3925 (2004).

98.   Zhao, J.-C. in *Methods for Phase Diagram Determination* 246–272 (Elsevier Ltd, 2007).

99.   Zhao, J.-C. Combinatorial approaches as effective tools in the study of phase diagrams and composition-structure-property relationships. *Prog. Mater. Sci.* **51,** 557–631 (2006).

100. Cao, S. & Zhao, J.-C. Application of dual-anneal diffusion multiples to the effective study of phase diagrams and phase transformations in the Fe-Cr-Ni system. *Acta Mater.* **88,** 196–206 (2015).

101. Tomlinson, W. J. & Andrews, A. J. Densities of fcc nickel-iron alloys. *Met. Sci.* **12,** 263–264 (1978).

102. Shirakawa, Y., Tanji, Y., Moriya, H. & Oguma, I. The elastic constants of Ni and Ni-Fe (fcc) alloys. *Sci. Reports Res. Institutes, Tohoku Univ. Ser. A, Physics, Chem. Metall.* **21,** 187–200 (1969).

103. Alers, G. A., Neighbours, J. R. & Sato, H. Temperature dependent magnetic contributions to the high field elastic constants of nickel and an Fe-Ni alloy. *J. phys. chem. solids* **13,** 40–55 (1960).

104. White, P. S., Rodgers, J. R. & Le Page, Y. CRYSTMET: a database of the structures and powder patterns of metals and intermetallics. *Acta Crystallogr.* **58,** 343–348 (2002).

105. Chiroiu, C., Munteanu, L., Chiroiu, V., Delsanto, P. P. & Scalerandi, M. A genetic

algorithm for determination of the elastic constants of a monoclinic crystal. *Inverse Probl.* **16,** 121–132 (2000).

106. Guenin, G., Jara, D. R., Murakami, Y., Delaey, L. & Gobin, P. F. Some elastic properties of a single crystal of Cu-Zn-Al martensite. *Scr. Metall.* **13,** 289–292 (1979).

107. Küppers, H. The elastic constants of monoclinic potassium hydrogen oxalate. *Acta Crystallogr.* **29,** 415–419 (1973).

108. Isaak, D. G. & Ohno, I. Elastic constants of chrome-diopside: application of resonant ultrasound spectroscopy to monoclinic single-crystals. *Phys. Chem. Miner.* **30,** 430–439 (2003).

109. Lee, C.-F. Under Bump Metallization. U.S. Patent 20160268221 A1 (2016).

110. Bloom, T. R. Ball Grid Array Package. U.S. Patent 20070164433 A1 (2007).

111. Banerjee, K., Souri, S. J., Kapur, P. & Saraswat, K. C. 3-D ICs: A novel chip design for improving deep-submieroraeter interconnect performance and systems-on-chip integration and systems-on-chlp integration. *Proc. IEEE* **89,** 602–632 (2001).

112. Lea, R. M. *et al.* A 3-D stacked chip packaging solution for miniaturized massively parallel processing. *IEEE Trans. Adv. Packag.* **22,** 424–432 (1999).

113. Davis, W. R. *et al.* Demystifying 3D ICs : The pros and cons of going vertical. *IEEE Des. Test Comput.* **22,** 498–510 (2005).

114. Lau, J. H. TSV manufacturing yield and hidden costs for 3D IC integration. in *IEEE Electronic Components and Technology Conference* 1031–1042 (2010).

115. Banijamali, B., Ramalingam, S., Liu, H. & Kim, M. Outstanding and innovative reliability study of 3D TSV interposer and fine pitch solder micro-bumps. in *Electronic Components and Technology Conference* 309–314 (2012).

116. Yu, J. J., Wu, J. Y., Yu, L. J. & Kao, C. R. Choice of intermetallic compounds for structural applications in near submicron joints. in *IEEE 66th Electronic Components and Technology Conference* 1135–1140 (2016).

117. Yu, L. J., Yen, H. W., Wu, J. Y., Yu, J. J. & Kao, C. R. Micromechanical behavior of single crystalline Ni_3Sn_4 in micro joints for chip-stacking applications. *Mater. Sci. Eng. A* **685,** 123–130 (2017).

118. Lee, N. T. S. *et al.* Structural and mechanical properties of Sn-based intermetallics from ab initio calculations. *Appl. Phys. Lett.* **89,** 141908 (2006).

119. Gao, F. & Qu, J. Elastic moduli of $(Ni,Cu)_3Sn_4$ ternary alloys from first-principles calculations. *Electron. Mater.* **39,** 2429–2434 (2010).

120. Tong, B. M., Sriram, V., Minor, A. & Yang, J. In situ and ex situ nanomechanical analysis of reactive nanolayer solder joints. *Adv. Eng. Mater.* **11,** 645–649 (2009).

121. Kresse, G. & Furthmüller, J. Efficient iterative schemes for ab initio total-energy calculations using a plane-wave basis set. *Phys. Rev. B* **54,** 169–186 (1996).

122. Blöchl, P. E. Projector augmented-wave method. *Phys. Rev. B* **50,** 953–979 (1994).

123. Perdew, J. P., Burke, K. & Ernzerhof, M. Generalized gradient approximation made simple. *Phys. Rev. Lett.* **77,** 3865–3868 (1996).

124. Monkhorst, H. J. & Pack, J. D. Special points for Brillouin-zone integrations. *Phys. Rev.* **13,** 5188–5192 (1976).

125. Ghosh, G. A first-principles study of cementite (Fe_3C) and its alloyed counterparts: Elastic constants, elastic anisotropies, and isotropic elastic moduli. *AIP Adv.* **5,** 87102 (2015).

126. Huron, E. S. & Roth, P. G. The influence of inclusions on low cycle fatigue life in a P/M nickel-base disk superalloy. in *Superalloys 1996* 359–368 (1996).

127. Raisson, G. Evolution of PM nickel base superalloy processes and products. *Powder Metall.* **51,** 10–13 (2008).

128. Schafrik, R. & Sprague, R. Saga of gas turbine materials part III. *Adv. Mater. Process.* **162,** 29–33 (2004).

129. Wlodek, S. T., Kelly, M. & Alden, D. A. The structure of René 88DT. in *Superalloys* 129–136 (1996).

130. Pollock, T. M. & Tin, S. Nickel-based superalloys for advanced turbine engines: chemistry, microstructure and properties. *J. Propuls. Power* **22,** 361–374 (2006).

131. Unocic, R. R. *et al.* Mechanisms of creep deformation in polycrystalline Ni-base disk superalloys. *Mater. Sci. Eng. A* **483–484,** 25–32 (2008).

132. Viswanathan, G. B., Karthikeyan, S., Sarosi, P. M., Unocic, R. R. & Mills, M. J. Microtwinning during intermediate temperature creep of polycrystalline Ni-based superalloys: Mechanisms and modelling. *Philos. Mag.* **86,** 4823–4840 (2006).

133. Miao, J., Pollock, T. M. & Jones, J. W. Fatigue crack initiation in nickel-based superalloy René 88 DT at 593°C. in *Superalloys* 589–597 (2008).

134. Stinville, J. C., Lenthe, W. C., Miao, J. & Pollock, T. M. A combined grain scale elastic-plastic criterion for identification of fatigue crack initiation sites in a twin

containing polycrystalline nickel-base superalloy. *Acta Mater.* **103,** 461–473 (2016).

135. Miao, J., Pollock, T. M. & Wayne Jones, J. Crystallographic fatigue crack initiation in nickel-based superalloy René 88DT at elevated temperature. *Acta Mater.* **57,** 5964–5974 (2009).

136. Shenoy, M., Zhang, J. & McDowell, D. L. Estimating fatigue sensitivity to polycrystalline Ni-base superalloy microstructures using a computational approach. *Fatigue Fract. Eng. Mater. Struct.* **30,** 889–904 (2007).

137. Cerrone, A., Tucker, J., Stein, C., Rollett, A. & Ingraffea, A. Micromechanical modeling of René 88DT: from characterization to Simulation. in *Joint Conference of the Engineering Mechanics Institute and the 11th ASCE Joint Specialty Conference on Probabilistic Mechanics and Structural Reliability* 1–10 (2012).

138. Findley, K. O. & Saxena, A. Low cycle fatigue in rene 88DT at 650 °C: Crack nucleation mechanisms and modeling. *Metall. Mater. Trans. A* **37,** 1469–1475 (2006).

139. Chan, K. S. A microstructure-based fatigue-crack-initiation model. *Metall. Mater. Trans. A* **34A,** 43–58 (2003).

140. Caton, M. J., Jha, S. K., Rosenberger, A. H. & Larsen, J. M. Divergence of mechanisms and the effect on the fatigue life variability of René 88 DT. in *Superalloys* 305–312 (2004).

141. Stinville, J. C. *et al.* Sub-grain scale digital image correlation by electron microscopy for polycrystalline materials during elastic and plastic deformation.

Exp. Mech. **56,** 197–216 (2016).

142. Tschopp, M. A., Bartha, B. B., Porter, W. J., Murray, P. T. & Fairchild, S. B. Microstructure-dependent local strain behavior in polycrystals through In-Situ scanning electron microscope tensile experiments. *Metall. Mater. Trans. A* **40A,** 2363–2368 (2009).

143. Stinville, J. C., Vanderesse, N., Bridier, F., Bocher, P. & Pollock, T. M. High resolution mapping of strain localization near twin boundaries in a nickel-based superalloy. *Acta Mater.* **98,** 29–42 (2015).

144. Wu, H. *et al.* A high-throughput methodology search for the optimum cooling rate in an advanced polycrystalline nickel base superalloy. *Mater. Des.* **128,** 176–181 (2017).

145. Krueger, D. D., Kissinger, R. D. & Menzies, R. G. Development and introduction of a damage tolerant high temperature nickel-base disk alloy, René 88DT. in *Superalloys* 277–286 (1992).

146. Hill, R. The elastic behaviour of a crystalline aggregate. *Proc. Phys. Soc. Sect. A* **65,** 349–354 (1952).

147. Tufft, M. Shot peen impact on life, part 2: single particle impact tests using production shot. in *International Conference on Shot Peening* 254–263 (1999).

148. Lewandowski, J. J., Wang, W. H. & Greer, A. L. Intrinsic plasticity or brittleness of metallic glasses. *Philos. Mag. Lett.* **85,** 77–87 (2005).

149. Schuh, C. A., Hufnagel, T. C. & Ramamurty, U. Mechanical behavior of amorphous alloys. *Acta Mater.* **55,** 4067–4109 (2007).

150. Eckert, J., Das, J., Pauly, S. & Duhamel, C. Mechanical properties of bulk metallic glasses and composites. *J. Mater. Res.* **22,** 285–301 (2007).

151. Szuecs, F., Kim, C. P. & Johnson, W. L. Mechanical properties of $Zr_{56.2}$ $Ti_{13.8}Nb_{5.0}Cu_{6.9}Ni_{5.6}Be_{12.5}$ ductile phase reinforced bulk metallic glass composite. *Acta Mater.* **49,** 1507–1513 (2001).

152. Jiang, Q. K. *et al.* Super elastic strain limit in metallic glass films. *Sci. Rep.* **2,** 3–8 (2012).

153. Kese, K. O., Li, Z. C. & Bergman, B. Influence of residual stress on elastic modulus and hardness of soda-lime glass measured by nanoindentation. *J. Mater. Res.* **19,** 3109–3119 (2004).

154. Pharr, G. M. Measurement of mechanical properties by ultra-low load indentation. *Mater. Sci. Eng. A* **253,** 151–159 (1998).

155. Cao, Q. P. *et al.* Bending behavior of electrodeposited glassy Pd-P and Pd-Ni-P thin films. *Scr. Mater.* **68,** 455–458 (2013).

156. Yao, D. *et al.* A size-dependent constitutive model of bulk metallic glasses in the supercooled liquid region. *Sci. Rep.* **5,** 1–8 (2015).

157. Huang, Y. J., Shen, J. & Sun, J. F. Bulk metallic glasses: Smaller is softer. *Appl. Phys. Lett.* **90,** 88–91 (2007).

158. Wagner, H. *et al.* Local elastic properties of a metallic glass. *Nat. Mater.* **10,** 439–442 (2011).

159. Rabe, U. *et al.* Imaging and measurement of local mechanical material properties by atomic force acoustic microscopy. *Surf. Interface Anal.* **33,** 65–70 (2002).

160. Franco, E. E. *et al.* Measurement of elastic properties of materials by the ultrasonic through-transmission technique. *Dyna* **168,** 59–64 (2011).

161. Khanisanij, M. & Sidek, H. A. A. Elastic behavior of borate glasses containing lead and bismuth oxides. *Adv. Mater. Sci. Eng.* **2014,** 1–8 (2014).

162. Sidek, H. A. A., Chow, S. P., Talib, Z. A. & Halim, S. A. Formation and elastic behavior of lead-magnesium chlorophosphate glasses. *Turkish J. Phys.* **28,** 65–71 (2004).

163. Viktorov, I. A. *Rayleigh and Lamb Waves*. (Plenum Press, 1967).

164. Lowrie, R. & Gonas, A. M. Single-crystal elastic properties of tungsten from 24° to 1800°C. *J. Appl. Phys.* **38,** 4505–4509 (1967).